MODELS OF THE ACTIN-LIKE MREB HELIX IN PROKARYOTES

by
Jun Allard

SUBMITTED IN PARTIAL FULFILLMENT OF THE
REQUIREMENTS FOR THE DEGREE OF
MASTER OF SCIENCE

AT

DALHOUSIE UNIVERSITY
HALIFAX, NOVA SCOTIA
JULY 10, 2007

DALHOUSIE UNIVERSITY

DEPARTMENT OF PHYSICS AND ATMOSPHERIC SCIENCE

The undersigned hereby certify that they have read and recommend to the Faculty of Graduate Studies for acceptance a thesis entitled "**Models of the actin-like MreB helix in prokaryotes**" by **Jun Allard** in partial fulfillment of the requirements for the degree of **Master of Science**.

Dated: July 10, 2007

Supervisor: Andrew Rutenberg

Readers: Manfred Jericho

Jürgen Kreuzer

Rich Dunlap

DALHOUSIE UNIVERSITY

Date: **July 10, 2007**

Author: **Jun Allard**

Title: **Models of the actin-like MreB helix in prokaryotes**

Department: **Physics and Atmospheric Science**

Degree: **M.Sc.** Convocation: **October** Year: **2007**

Signature of Author

Table of Contents

List of Figures

Abstract

MreB is an actin-like protein that forms a helix running the length of cylindrical bacterial cells. A quantiative model of the helix is presented. Individual polymers that make up the helical cables are represented by simple force-dependent polymer models bundled into a supramolecular array. Boundary conditions and external forces are provided by a global elasticity model that represents the cables as flexible rods buckled into a helix inside the confinement of the cell wall. Variational techniques and stochastic simulation are used to obtain a quantitative relationship between the pitch of the helix, the total abundance of MreB and the thickness of the cables. Finite element analysis is performed to simulate the elastic dynamics of the MreB cables and a hypothesis for the external forces acting upon the cables is proposed. The model has implications for the *de novo* establishment of the cables, cell growth, and for MreB's role in macromolecular trafficking, the polarization of *Caulobacter crescentus* and cell wall synthesis.

List of Symbols

a_0	size of one MreB monomer (nm)
α_{on}	pointed/barbed asymmetry in on-rates
α_{off}	pointed/barbed asymmetry in off-rates
B	bending modulus of one MreB protofilament ($\text{pN}\,\text{nm}^2$)
C	twisting modulus of one MreB protofilament ($\text{pN}\,\text{nm}^2$)
c_c	critical concentration (μM or nM)
δ	polymer extension after addition of one monomer (nm)
∂_s	differentiation with respect to unstretched arclength (nm^{-1})
EA	stretching modulus of one MreB protofilament (pN)
η	cytoplasmic viscosity ($\text{pN}\,\text{s}/\,\text{nm}^2$)
F_B	effective force opposing polymerization at tips of MreB bundle (pN)
F_E	Euler buckling force (pN)
f_0	polymerization force scale (pN)
f_B	elastic force scale (pN)
$\mathcal{H}$	elastic Hamiltonian of MreB bundle
k^b_{on}	polymerization on rate constant at barbed end ($\mu\text{M}^{-1}\,\text{s}^{-1}$)
k^b_{off}	polymerization off rate constant at barbed end (s^{-1})
k^p_{on}	polymerization on rate constant at pointed end ($\mu\text{M}^{-1}\,\text{s}^{-1}$)
k^p_{off}	polymerization off rate constant at pointed end (s^{-1})
κ	curvature of MreB filament (nm^{-1})
l^e	length of an element in finite element analysis (nm)
L_c	length of cylindrical portion of cell (nm)
L_{fil}	length of MreB filament bundle (nm)
L_{proto}	length of one MreB protofilament (nm)
λ_{tread}	free treadmilling rate (s^{-1})
μ	angular viscosity (pN s/rad)
n	thickness of MreB bundle, in protofilaments

n_{el}	number of elements in finite element analysis
n_{tip}	number of protofilaments that reach the bundle tip
N	number of free MreB subunits in the cytoplasm
N_0	total number of MreB subunits in a cell
N_C	number of MreB subunits per μM in a standard cell geometry
ν	force density (pN/ nm)
p	pitch of MreB helix (nm)
$\hat{\phi}$	azimuthal direction on a cylinder
R_c	radius of cell (nm)
τ	total local twist in MreB filament (nm^{-1})
τ_c	centerline torsion in MreB filament (nm^{-1})
τ_L	internal twist in MreB filament (nm^{-1})
θ	pitch angle of MreB helix, measured from cell's axis
ξ_p	persistence length of filament (μm)

Acknowledgements

I thank my advisor, Dr. Andrew Rutenberg, for four years of patience and wisdom in matters not limited to our research. I thank Dr. Manfred Jericho (Dalhousie), Dr. Rut Carballido-Lopez (INRA, Paris) and Dr. Julie Theriot (Stanford) for valuable discussion; the Rutenberg Group, Christina Sheppard and the Dunn ecosystem. This work was supported by an NSERC Canada Graduate Scholarship.

Halifax, July 2007

Jun Allard

Chapter 1

Introduction

> "It is truly breathtaking that within a period of 5 years a longstanding 'truth' about one of the major life forms of the planet has been overturned." [77]

Life on Earth is divided into two empires: the eukaryote empire, which includes all plants, animals, yeast and algae, and the prokaryote empire, which includes bacteria and archaea. The 'truth' the authors were referring to is the belief that prokaryotes lack a key ingredient that endows other cells with shape, motility and function, called the cytoskeleton. This was considered one of the fundamental differences between eukaryotes and prokaryotes, and one of the factors that allowed eukaryotes to evolve in size and complexity unseen in the prokaryotes. The discovery of a protein called MreB in 2001 led to the collapse of this dogma.

MreB forms a helix running the length of cylindrical cells. It is present in nearly all cylindrical-shaped bacteria, and is implicated in several vital functions. Little is known about the arrangement of molecules that make up the helix, although it is a cousin of actin, the protein that forms the cytoskeleton in eukaryotes.

The helix has raised many open questions. What causes the helical configuration of MreB? What controls the pitch of this helix? How does MreB mechanistically perform its many functions? The tools of physics are appropriate both for testing possible explanations regarding MreB and its functions, and for raising new questions. These tools range from stochastic simulation at the molecular level to continuum elastic models at the supramolecular level. This thesis is an attempt to build a quantitative model and address these questions.

1.1 Organization of this thesis

Chapter 2 presents biological background about the actin cytoskeleton in eukaryotes, including the Brownian ratchet model of force generation. We review the recent experimental information about MreB, and other relevant cytoskeletal elements.

Chapter 3 develops a model of MreB. In Sec. 3.1 we state the polymerization dynamics equation and how they are used to represent the MreB bundle. In Sec. 3.2 we introduce a standard elastic Hamiltonian and use the Cosserat formalism to represent the MreB bundle as an elastic body.

Chapters 4 and 5 describe the results of this model. In Chapter 4, a helical configuration is assumed and the polymerization dynamics are explored analytically and by stochastic simulation. Force generation by a stochastic polymer bundle is discussed in Sec. 4.3. The implications of the model for macromolecular transport are discussed in Sec. 4.6. Chapter 5 presents finite element analysis of the MreB filament inside a cell under various boundary conditions. Three simple models are explored, and Sec. 5.6 discusses their implications for cell wall synthesis.

Chapter 6 contains overall conclusions, summarizes the main results and suggests directions for future work.

Chapter 2

Biological Background

2.1 The actin cytoskeleton in eukaryotes

Many biological functions require something to move. For example, the learning and memory-forming that takes place as this sentence is read requires the neurons in the brain of the reader to have grown in a particular arrangement during development. The physical mechanism leading to this motility, and many other biological functions, is driven by a protein called actin [79].

Actin is ubiquitous, highly-conserved, and forms two-stranded polymers, which in turn form diverse supramolecular structures inside all eukaryotic cells. These structures are collectively known as the actin cytoskeleton. The actin cytoskeleton extends throughout the cytoplasm like a spider's web (Fig. 2.1). It organizes cell shape and cell polarity, drives cell division, organizes subcellular transport and muscle contraction in mammals, and gives rise to many kinds of cell motility.

The actin cytoskeleton organizes subcellular transport of vesicles and other organelles by serving as a track for myosins, which are motor proteins that step along the actin cables by hydrolyzing ATP. By attaching a load to the myosin, the cell can transport the load along the actin cable with speeds of $\approx 200 - 400\,\mathrm{nm/\,s}$ [71]. By attaching a myosin to two opposing actin cables, the cell can pull the two cables together with forces of $1 - 10\,\mathrm{pN}$ [39], giving rise to muscle contractions.

Actin itself can polymerize against a load, such as a cell membrane. The cell membrane can thus develop protrusions, called fillopodia and lamellopodia. By pulling up the cell behind this protrusion, cells such as nematode sperm, keratocytes and neutrophiles can crawl with speeds up to several microns per second [57]. An explanation of the mechanism of this force generation, by Mogilner and Oster in 1996 [61], was a major contribution of computational cell biology [67]. It was preceded and followed by a decade of quantitative modeling of actin ranging from molecular scales [65] to

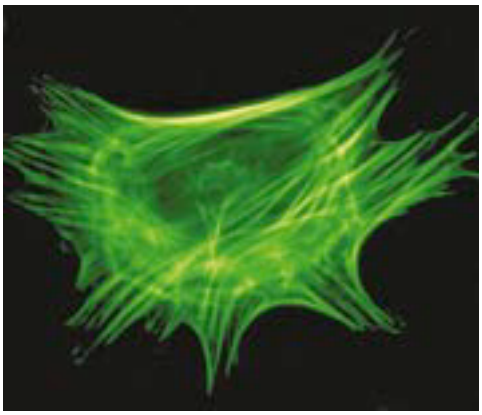

Figure 2.1: The actin cytoskeleton, seen through GFP fluorescence in a eukaryotic cell. Taken from [67].

bulk, continuum elastic regimes [87]. We describe Mogilner and Oster's model here.

2.1.1 Polymerization models and the elastic Brownian ratchet

Actin is a protein that assembles with many copies of itself to form polymers. Addition and dissociation of monomers occur at the ends of the asymmetric actin filament, both at the "barbed" ("+" or fast-growing) tip and the "pointed" ("−" or slow-growing) tip. The kinetics of actin polymerization are well-characterized by concentration-dependent polymerization rates $k^b_{\text{on}}c$ and $k^p_{\text{on}}c$ at the barbed and pointed ends, respectively, where c is the cytoplasmic monomer concentration, and concentration-independent depolymerization rates k^b_{off} and k^p_{off}. This is summarized in Fig. 2.2A.

The average growth rate of the tips are

$$v^b = \delta(k^b_{\text{on}}c - k^b_{\text{off}}) \tag{2.1}$$

$$v^p = \delta(k^p_{\text{on}}c - k^p_{\text{off}}) \tag{2.2}$$

where δ is the length increase due to the addition of one monomer. The total length of the filament will grow above, and shrink below, a critical concentration,

$$c_c = \frac{k^b_{\text{off}} + k^p_{\text{off}}}{k^b_{\text{on}} + k^p_{\text{on}}}. \tag{2.3}$$

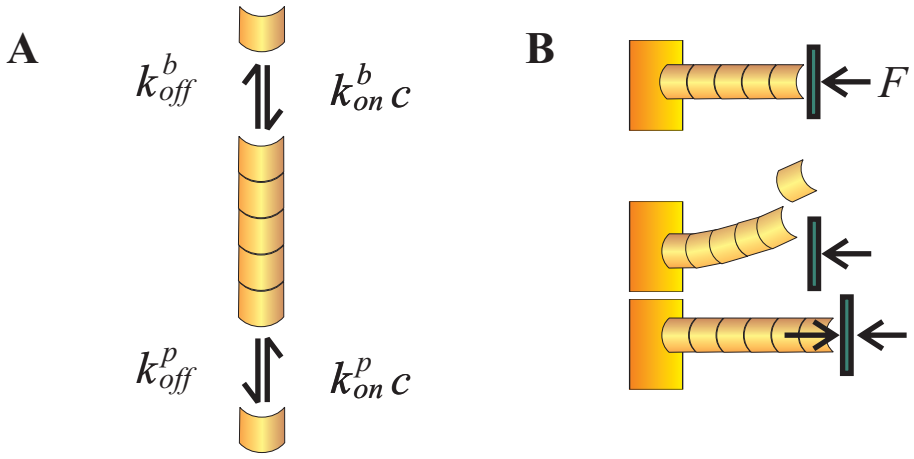

Figure 2.2: (A) Polymerization model, including concentration-dependent "on" rates and independent "off" rates at the barbed and pointed ends. (B) elastic Brownian ratchet mechanism for polymerization against a load force F.

The asymmetry between the polymerization and depolymerization rates at barbed and pointed ends leads to treadmilling, in which the filament length remains constant while depolymerization from the pointed end is balanced by polymerization at the barbed end [1]. The treadmilling rate is [20]

$$\lambda_{tread} = \frac{k^p_{\rm off}k^b_{\rm on} - k^b_{\rm off}k^p_{\rm on}}{k^p_{\rm on} + k^b_{\rm on}}. \tag{2.4}$$

If the filament position is fixed, treadmilling results in a net advection of all polymerized monomers towards the pointed end.

When an actin filament encounters a load, F, it does not simply stall. Instead, thermal undulations of the filament will occasionally allow another monomer addition to take place. In this situation, the polymerization rate reduces to $k^b_{\rm on} \to k^b_{\rm on}p(F)$ where $p(F)$ is the steady-state probability of a gap of width δ between the filament tip and the load. In the regime where thermal undulations are fast compared to polymerization, the load is always pushing against the tip and this probability is simply given by a Boltzmann factor, $p(F) = \exp\left(-F\delta/k_BT\right)$ where $F\delta$ is the work done against the load by the assembly of one additional monomer, and $k_BT = 4.1\,\mathrm{pN\,nm}$ is the thermal energy unit [60].

Upon first consideration, this is in violation of the second law of thermodynamics famously described by Richard Feynman in a thought-experiment of the "thermal

ratchet" [27]. Feynman imagined vanes attached to a shaft with a one-way ratchet, shown in Fig. 2.3. As molecules bombarded the vanes, the ratchet would turn one way, harnessing thermal energy to do useful work. However, Feynman argued that the pawl snapping against the teeth of the wheel (giving rise to the irreversibility of the ratchet) is necessarily dissipating energy, and soon the thermal fluctuations of the pawl would allow the teeth to pass in either direction. Thermal ratchets cannot perform useful work. How, then, can actin generate a force? The resolution lies in the fact that living cells are open systems far from equilibrium. To make this distinction, Mogilner and Oster [61] called their actin model the "elastic Brownian ratchet". The "pawl" that gives rise to the asymmetry of actin polymerization is the chemical energy difference between free monomers and polymerized monomers, and the ATP hydrolysis of the actin subunits after addition. The continually renewed ATP binding to the actin monomers that are diffuse in the cytoplasm allows the polymer to perform work, even in steady-state.[1]

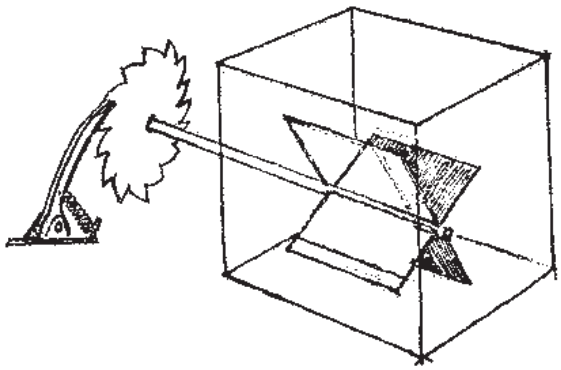

Figure 2.3: Feynman's thermal ratchet. Taken from [27].

Subsequent experiments validated the force-velocity-concentration relationships described above [68]. The ratchet mechanism's efficiency can be estimated by the chemical binding free energy for one monomer, $\Delta G = k_B T \ln(k_{\text{on}} c / k_{\text{off}})$. For typical parameters in eukaryotes, this is roughly 20 pN nm, while the work performed against

[1]Note that ATP is only required for the polymer to perform work in steady-state. The work itself requires only polymerization, as is strikingly evident in individuals with sickle cell anemia. In such cells, hemoglobin (which has no ATP activity) polymerizes much like actin, forcing the cell membrane out and forming spiky projections [83].

the load is $F\delta \approx 11.4\,\mathrm{pN\,nm}$, giving an efficiency of ≈ 0.68 [63].

In vivo, actin dynamics are regulated through over 126 "actin-binding proteins" [8,70] that variously control cross-linking, bundling, filament nucleation, end-capping, filament cutting, monomer sequestration and desequestration. Four such actin-binding proteins are listed here:

- ADF/cofilin is a depolymerizing factor that speeds up depolymerization of actin by binding to two adjacent subunits and modifying their twist slightly, increasing their propensity to separate and thus their k_{off} by up to 20 times [70].

- Profilin binds to free monomers of actin, sequestering them and allowing eukaryotic cells to maintain a cytoplasmic concentration of monomers much higher than the critical concentration. By regulating the amount of actin sequestered by profilin, cells using actin-driven motility can regulate their speed [34, 68].

- Formin binds to the barbed end of actin. It can nucleate new polymers, and also control their growth while remaining processively attached at the barbed end. In the presence of profilin, formin augments the barbed growth rate by 10 to 15 times, and can mediate a force of several piconewtons [46].

- Fimbrin, villin, fascin and epsin all bundle actin filaments, leading to bulk cables of actin that are several polymers thick [34]. Fimbrin, in particular, only bundles polymers that face the same direction, leading to a polarized bundle [43].

2.2 The MreB helix in prokaryotes

Until recently, it was believed that prokaryotic cells lack actin-like cytoskeletons. However, in 2001, MreB was identified as a protein with a cytoskeleton-like role in many bacteria. The subsequent years were a period of rapid advance for microbiology. (For excellent reviews see [8, 59, 77].)

The rapid advance was preceded by a pioneering computational search of possible protein structures in 1992, in which the protein MreB was predicted to be an actin homologue [6]. Even though the actual sequence similarity was only $\approx 15\%$ (less than the 20% typically used to identify homologues [8]), Bork *et al.* predicted MreB

would fold in a similar way to actin, and thus might be functionally homologous. It was not until after the advancement of fluorescence microscopy techniques [59] that, in 2001, Bork *et al.*'s predictions were confirmed and MreB was shown to play a cytoskeleton-like role in *Bacillus subtilis* [41].

MreB assembles into a helical structure extending the length of rod-shaped cells, as shown in Fig. 2.4. It was identified in *Escherichia coli*, *Caulobacter crescentus*, *Rhodobacter sphaeroides* and subsequently in all rod-shaped prokaryotes for which the genomes were known [12] (except Corynebacteria which grows exceptionally slowly), and in several non-rod-shaped species. It is vital, and is highly conserved between species, meaning it probably originated before the common ancestor of all prokaryotes. It is believed to have originated even before the divergence of prokaryotes and eukaryotes, making it the universal ancestor of actins [86].

In Gram-positive species, which have thicker cell walls, several MreB paralogues are often present. In *B. subtilis*, which is Gram-positive, three distinct paralogues exist: MreB, Mbl (named MreB-like) and MreBH. In Gram-negative species, such as *E. coli* and *C. crescentus*, only MreB is present.

In vivo, MreB has been observed by tagging the *mreB* gene with GFP (green fluorescent protein), and then observing its spatial structure using fluorescence microscopy. There is much disagreement between quantitative measurements. The helical pitches for MreB or Mbl, without other paralogues, are $0.73 \pm 0.12\,\mu$m and $1.7 \pm 0.28\,\mu$m, respectively [41]. Measurements on co-localized MreB, Mbl and MreBH report pitches of $0.6 \pm 0.17\,\mu$m [15]. In *E. coli*, pitches of $0.46 \pm 0.08\,\mu$m have been reported [50]. In all cases, the helices are dynamic, with elements moving along the main helix at reported speeds ranging from $6.0\,\mathrm{nm/s}$ [44] to $0.07\,\mu\mathrm{m/s}$ [80]. Fluorescence photobleaching (FRAP) experiments have been performed, where a part of the cell is exposed to an intense, focused beam of light that permanently deactivates the GFP tags for affected molecules. These experiments show that the helix is continually being remodelled, with a half-life of about 8 minutes and no obvious polarity [9]. The helical structure has also been observed to condense into a ring at midcell near the time of division in *E. coli* [76], *C. crescentus* [29] and *B. subtilis* (where only MreBH coils) [10].

The MreB helix appears not to be a single polymer extending the length of the cell but rather a bundle of individual polymers [9, 28]. More will be said regarding the microscopic composition of the helix in Sec. 3.1.2. Quantitative immunoblotting has been used to measure the molecular abundance of various MreBs. In *B. subtilis*, there are roughly 8000 MreB monomers and $12000 - 14000$ of Mbl [41] while *E. coli* has roughly $17000 - 40000$ monomers of MreB [50]. Neglecting the cytoplasmic fraction of monomeric MreB, these abundances suggest a bundle thickness of about 10 protofilaments [21].

As mentioned above, MreB is vital in *E. coli*, *B. subtilis* and *C. crescentus*. It appears to play a central role in several vital cell functions including cell wall synthesis, macromolecular transport, chromosome segregation and the polarization of *C. crescentus*. Little is known about the mechanism through which MreB performs these roles, each of which is discussed below.

2.2.1 Cell wall synthesis

The *mre* genes had been known to play an important role in cell shape and controlling synthesis of the the cell wall. The cell wall is a giant sacculus made of peptidoglycan, also known as murein (*mre* was named after "murein related cluster e"). The hard peptidoglycan cell wall is a primary determinant of cell shape, since an isolated sacculus retains its shape (although deflated) [77]. The cell wall has an elastic modulus of 2.7×10^7 N/m^2 in *E. coli* [93]. As mentioned above, Gram-positive species have even thicker cell walls, and the elastic modulus is probably larger still.

In *B. subtilis* Mbl is necessary for proper insertion of new peptidoglycan, which occurs in a helical fashion [12], while MreBH is necessary for the localization and function of the cell wall hydrolase LytE that is believed to recycle the outer layers of the cell wall, also in a helical fashion [10]. In addition, *mreB* mutants are wide, rounded and usually not viable [30]. Mutants without MreB grow spherical and round, and some eventually lyse under their own stress. It is likely that MreB regulates cell shape by organizing the machinery used for cell wall growth.

It has been suggested that MreB (and Mbl in *B. subtilis*) forms a complex with transmembrane proteins MreC and MreD, and with penicillin-binding proteins, which

are the machinery necessary for insertion of new peptidoglycan into the cell wall [9,77]. Evidence for this suggestion is mixed: MreB does not always colocalize with MreC in *C. crescentus* [17]. It appears likely that helical bundles of MreB affect the spatial pattern of these associated proteins.

2.2.2 Macromolecular transport

Many proteins need to be localized to the poles of the cell in order to function properly. These include proteins involved in some anatomical functions, such as synthesis of flagella or pili, or other motility-associated apparatus such as the actin comet-tail nucleating proteins in *Shigella flexneri*. The proper localization of many of these proteins depends on MreB. Disrupting MreB leads to an immediate loss of polar localization to a host of proteins including the chemotaxis protein Tar and the virulence factor IcsA in *E. coli* [75], and three integral membrane proteins (PleC, DivJ, CckA) in *C. crescentus* [35]. Polar localization in *C. crescentus* was disrupted by either underexpression or overexpression of MreB. When normal MreB expression was returned polar localization was re-established within 4 hours [35]. The time of loss of localization is too short for the long-term effects of MreB loss on cell wall shape to be the mediating factor. This suggests that MreB has a continual role in either direct polar trafficking of these proteins or in the maintenance of landmarks necessary for their proper positioning [8].

Several possibilities exist for the mechanism of polar localization. The first is that MreB plays the same role as actin in eukaryotic macromolecule transport. Actin is a passive track along which myosin motor proteins carry macromolecules. Alternatively, segments of the MreB helix may themselves move toward the poles, carrying their loads with them. Another possibility is that MreB affects polar localization indirectly, for example by initiating polar markers where its free ends are located [77]. We explore these possibilities in Sec. 4.6.

2.2.3 Polarization of *C. crescentus*

Cells of the species *C. crescentus* have a unique morphology and a unique cell cycle. Although they are rod-shaped, the two poles are distinct: during most of the cell

cycle, one pole is adorned with a stalk while the other has a flagellum. Upon division, the two daughter cells are also distinct, since one cell retains its stalk (the "stalked" cell) while the other uses its flagellum to swim (the "swarmer" cell). Eventually, the stalked cell grows another flagellum at its "swarmer" pole, while the swarmer sheds its flagellum and grows a stalk, and both cells are ready for another round of division.

Orchestrating this complex cell cycle requires that the polar proteins in *C. crescentus* be directed towards distinct poles in different stages of its life cycle. For example, PleC is localized to swarmer poles in swarmer and predivisional cells, DivJ is localized to stalked poles, while CckA is localized to both poles of predivisional cells [48]. This polarization is MreB-dependent. After MreB expression is disrupted and restored, PleC and DivJ are restored randomly to either pole [48]. This suggests that MreB may be polarized within *C. crescentus* and that the polarity of the MreB helix is randomly restored after its disruption.

2.2.4 Chromosome segregation

MreB's role in chromosome segregation in *E. coli*, *B. subtilis* and *C. crescentus* is reflected by interactions with both RNA polymerase [48] and SetB, a chromosome defect suppressor [23]. MreB drives a fast initial polar translocation of the origin-proximal region, *oriC*, of newly-replicated DNA [36]. Time-lapse microscopy has shown that the MreB-dependent polar transport of *oriC* in *B. subtilis* traveled $1.4\mu m$ in 11 minutes, with an average speed of $2.8\,\mathrm{nm}/s$ and a peak speed of $4.5\,\mathrm{nm}/s$ [89]. After this initial translocation, disruption of MreB does not affect the segregation of the rest of the chromosome.

2.3 Analogies

Insight into unknown aspects of the MreB helix can be gained through analogies with other biochemical elements in other species [28]. We summarize aspects of two other systems that are often discussed when considering MreB.

2.3.1 Actin cables in Yeast

Actin in yeast assembles into cables [43], that appear very similar to initial observations of MreB. These actin cables appear to have variable numbers of filaments along their lengths and show no obvious polarity. Thick and thin regions alternate along cables, as opposed to constant thickness or progressive tapering. These structures require the actin-binding protein fimbrin, which bundles and polarizes actin filaments.

When a depolymerization agent is added, they appear to depolymerize by losing subunits at $5 - 10\,\mathrm{s}^{-1}$, which agrees with $k_{\mathrm{off}}^{b} + k_{\mathrm{off}}^{p}$ measurements in vitro. Cables appear to depolymerize from their ends and also from points along their middle. Thus, the consistent model of the supramolecular structure is one in which a cable contains a number of actin filaments that overlap and are shorter than the cable but not very short (since depolymerization patchiness is observed during disassembly).

2.3.2 The FtsZ ring in bacteria

The first cytoskeleton-like element discovered in prokaryotes was the protein FtsZ [13], which is essential for cell division and present in nearly all prokaryotes. FtsZ is the earliest player in cell division, when it forms a ring at midcell that initiates the assembly of the "divisome" that eventually divides the mother cell into two daughters.

Only 30% of FtsZ subunits are incorporated into the ring, which means the ring is only 6 to 7 protofilaments thick. The in vivo concentration of FtsZ has been reported as $11\,\mu$M, which is higher than its critical concentration and thus implies that most subunits are polymerized. A favored model is an isodesmic assembly model in which protofilaments disassociate and re-associate within the ring, as well as to and from the cytoplasm. At 180 protofilaments of ~ 80 subunits in length, around 56 protofilaments would comprise the FtsZ ring. In an alternate (but not mutually exclusive) model, cytoplasmic FtsZ exists as monomers which polymerize onto the multi-stranded bundles in the ring [81].

2.4 Other helices in prokaryotes

Since the first visualization of the MreB helix in 2001, a large number of helices have been reported in a wide range of cellular components in prokaryotes.

The Min proteins that oscillate to establish the midcell division site [75] form a helix with a density of $\approx 2.2 \pm 0.4$ turns per micron, distinct from MreB. Genetic manipulation has shown no direct dependence between the two.

The Sec machinery is a general system for secreting proteins from the cytoplasm to the environment [32]. It appears in a helical pattern on the cell envelope with a pitch roughly double that of MreB in *E. coli* [78].

FtsZ has also been observed in a helix [82] when not condensed into the Z-ring, and as previously mentioned, nascent peptidoglycan is helical. Among other elements that have been reported to form helices are the cytoplasmic protein ParA [18], the lipopolysaccharides that make up the outer leaflet of the outer membrane [32], and outer membrane proteins including LamB [33]. SetB, the DNA-associated protein mentioned in Sec. 2.2.4, also forms a helix and may have an interaction with MreB [23].

Helices are becoming ubiquitous in prokaryotes. The understanding of MreB we seek in this thesis may provide a theoretical framework for understanding the independent helices and perhaps a literal framework for the helices that depend on MreB.

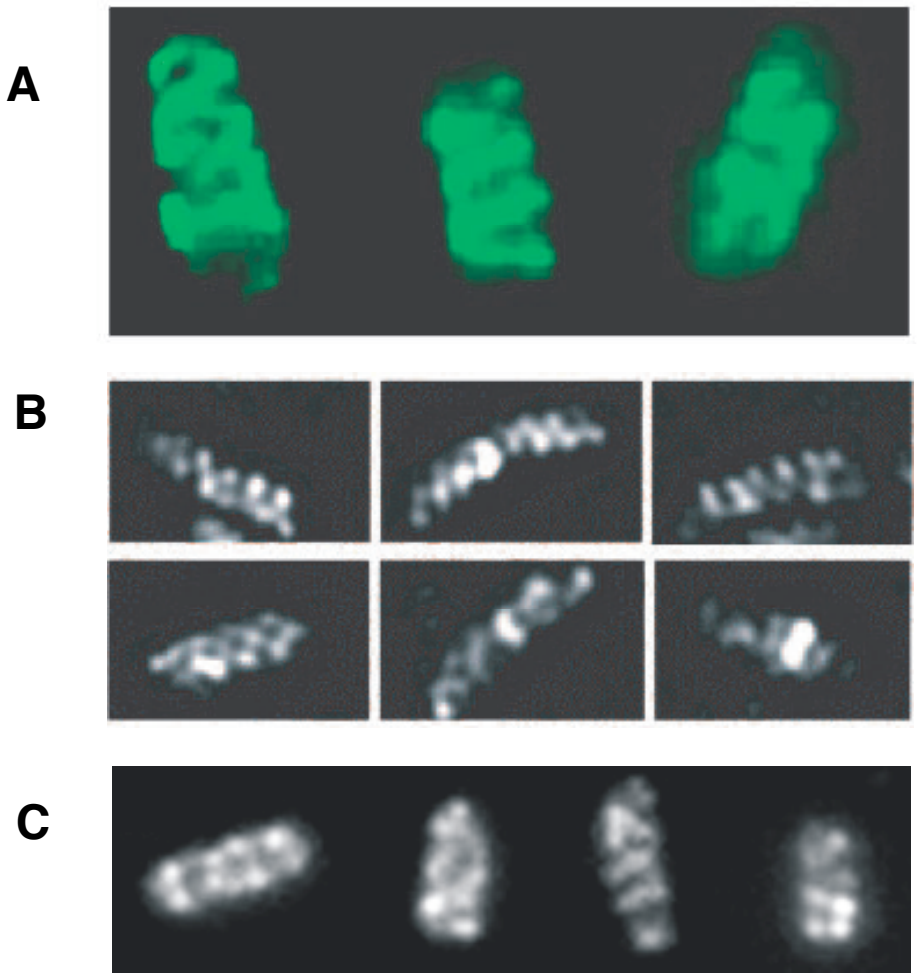

Figure 2.4: The MreB helix in vivo, tagged with fluorescent GFP and visualized through fluorescence microscopy. A) in *B. subtilis*, taken from [22]. B) in *C. crescentus*, from [29]. C) in *E. coli*, from [75].

Chapter 3

Model

In this chapter, we develop a framework to model the MreB helix in rod-shaped cells. The basic model has only one ingredient, MreB (or its homologues), which is considered at three scales. First, the simple polymerization models described in Sec. 2.1.1 are modified for the prokaryotic regime and for what is experimentally known about the differences between MreB and actin. Then, these polymers are combined into a putative ultrastructure in order to represent the in vivo cables, which we assume are composed of several polymers in a bundle. Finally, the cables are considered as a semi-flexible elastic body confined within the rod-shaped cell.

3.1 Polymerization Dynamics

In our model, each polymer, or *protofilament*, has a barbed tip at location x_i^b and pointed tip at location x_i^p. If $x_i^b > x_i^p$, then the protofilament is facing right, otherwise it is facing left. The locations are only allowed to be integer multiples of the subunit spacing, $a_0 = 5.1\,\text{nm}$ [86]. One difference between MreB and actin is the lack of helical twist inherent in the polymer [86]. In actin, the polymer is always two-stranded, with two rows of subunits twisted around each other with an angle of 65° the length gained through the addition of one subunit is $\delta = a_0 \cos 65° = 2.2\,\text{nm}$ [61]. Since MreB forms straight protofilaments without the double helix pattern, the length change by addition or subtraction of one monomer is exactly a_0.

The evolution of a protofilament occurs through four stochastic processes. For the moment assuming the filament faces right, these are

- barbed polymerization, $x_i^b \to x_i^b + a_0$ with rate $k_{\text{on}}^b c$,
- pointed polymerization, $x_i^p \to x_i^p - a_0$ with rate $k_{\text{on}}^p c$,
- barbed depolymerization, $x_i^b \to x_i^b - a_0$ with rate k_{off}^b, and

- pointed depolymerization, $x_i^p \to x_i^p + a_0$ with rate k_{off}^p.

where c is the concentration of monomers in the cytoplasm. An equivalent set of reactions results for left-facing protofilaments, with a change of sign. If a force is acting on the ith barbed tip, its polymerization rate becomes $k_{\text{on}} c \exp(-F_i/f_0)$ where we define $f_0 \equiv k_B T/a_0 = 0.010\,\text{pN}$ to be the polymerization force scale. This is the Brownian ratchet mechanism described in Sec. 2.1.1. Note that the appearance of a_0 instead of δ in this definition is another consequence of the lack of helical twist in the polymer. If n protofilaments share a particular load F, then we assume each protofilament bears an equal share, $F_i = F/n$. This load-sharing will be elaborated upon in Sec. 4.3.

The average growth rates of polymer ends are given by

$$v_i^b = a_0(k_{\text{on}}^b c e^{-F_i/f_0} - k_{\text{off}}^b) \tag{3.1}$$

$$v_i^p = a_0(k_{\text{on}}^p c e^{-F_i/f_0} - k_{\text{off}}^p) \tag{3.2}$$

The concentration of cytoplasmic monomers also varies as each protofilament grows or shrinks. The number of cytoplasmic monomers is denoted N. To determine its relation with the concentration of monomers, we must define the cell geometry. We assume rod-shaped bacterial cells are spherocylinders (ie cylinders with hemispherical end caps) of width $w = 2R_c$ and total length $l = L_c + 2R_c$. Such a cell has volume

$$V = \pi \left(\frac{w}{2}\right)^2 l + \frac{4}{3}\pi \left(\frac{w}{2}\right)^3 = \pi R_c^2 (L_c + \frac{4}{3} R_c). \tag{3.3}$$

Thus, to convert between molecular abundance N and concentration c in μM, we use $N = N_B V c$ where

$$N_B = \left(10^{-6}\text{micro}^{-1}\right) 10^{-24} \left[\frac{\text{litres}}{\text{nm}^3}\right] \cdot 6.02 \times 10^{23} \left[\frac{\text{molecules}}{\text{mole}}\right] \tag{3.4}$$

$$= 6.02 \times 10^{-7} \left[\frac{\text{molecules}}{\text{nm}^3\,\mu\text{M}}\right]. \tag{3.5}$$

For most of our results, we use a standard geometry of a *B. subtilis* cell, with $L_c = 3\,\mu$m and $R_c = 400\,$nm. These numbers were taken from a particular strain that has been used in several of the MreB studies (see [10] supplemental material), although

there is considerable variation in cell size even within the same strain. This standard geometry gives $V = 1.9\,\mu\mathrm{m}^3$, and for convenience we define

$$N_C = N_B V = 1069\,\mu\mathrm{M}^{-1} \tag{3.6}$$

so that $N = N_C c$.

3.1.1 Kinetic parameters

As described above, the polymerization dynamics of one protofilament are modeled by four stochastic processes, each with an independent rate constant,

$$\{k^b_{\mathrm{on}}, k^b_{\mathrm{off}}, k^p_{\mathrm{on}}, k^p_{\mathrm{off}}\}. \tag{3.7}$$

These rate constants are known as the kinetic parameters. The same dynamics can be represented by other combinations of four independent parameters, for example, the set

$$\{\lambda, c_c, \alpha_{\mathrm{on}}, \alpha_{\mathrm{off}}\} \tag{3.8}$$

where λ is the treadmilling rate, Eq. 2.4 (which sets the time scale), c_c is the critical concentration, Eq. 2.3 (which sets the concentration scale) and

$$\alpha_{\mathrm{on}} \equiv \frac{k^p_{\mathrm{on}}}{k^b_{\mathrm{on}}}, \quad \alpha_{\mathrm{off}} \equiv \frac{k^p_{\mathrm{off}}}{k^b_{\mathrm{off}}} \tag{3.9}$$

are the on-asymmetry and off-asymmetry, respectively (of the slow-growing pointed end relative to the fast-growing barbed end). Specifying these four parameters is equivalent to specifying the kinetic rates, since

$$k^b_{\mathrm{on}} = \frac{\lambda}{c_c}\left(\frac{1+\alpha_{\mathrm{off}}}{\alpha_{\mathrm{off}}-\alpha_{\mathrm{on}}}\right) \tag{3.10}$$

$$k^p_{\mathrm{on}} = \alpha_{\mathrm{on}}\frac{\lambda}{c_c}\left(\frac{1+\alpha_{\mathrm{off}}}{\alpha_{\mathrm{off}}-\alpha_{\mathrm{on}}}\right) \tag{3.11}$$

$$k^b_{\mathrm{off}} = \lambda\left(\frac{1+\alpha_{\mathrm{off}}}{\alpha_{\mathrm{off}}-\alpha_{\mathrm{on}}}\right) \tag{3.12}$$

$$k^p_{\mathrm{off}} = \alpha_{\mathrm{off}}\lambda\left(\frac{1+\alpha_{\mathrm{off}}}{\alpha_{\mathrm{off}}-\alpha_{\mathrm{on}}}\right) \tag{3.13}$$

The parametrization Eq. 3.8 has many desirable properties, for instance an easier interpretation in terms of physiological observations. The change-of-parametrization

formulae Eqs 3.10-3.13 are singular when $\alpha_{\text{on}} = \alpha_{\text{off}} \Longleftrightarrow \lambda = 0$. For example, ParM is another prokaryotic actin that is involved in segregating low-copy plasmids. ParM polymerizes with symmetric ends, thus $\alpha_{\text{on}} = \alpha_{\text{off}} = 1$. Also, $k_{\text{on}} = 5.3 \pm 1.3\,\mu\text{M}^{-1}\,\text{s}^{-1}$ and $k_{\text{off}} = 64 \pm 20\,\text{s}^{-1}$ [31], so $c_c \approx 12\,\mu\text{M}$ and $\lambda = 0$.

A key difference between MreB and actin is in their polymerization kinetics. The four kinetic rates for actin were measured in 1986 [66] directly by electron micrograph, and are given in Table 3.1.1. Measurement of actin's critical concentration and free treadmilling rate have confirmed the self-consistency of Eqs. 2.4 and 2.3.

MreB, however, exhibits different polymerization properties. It has an extremely high affinity for itself and a tendency to form gels, and all attempts to purify it from *B. subtilis*, *E. coli* or *C. crescentus* (a crucial first step for an in vitro study such as the one used to measure actin's kinetics) have been unsuccessful [15]. Thus it appears to have a much a lower critical concentration and much higher tendency to bundle. The only successful purification, and subsequent biochemical study, of MreB has been from the thermophilic bacteria *Thermotoga maritima* [24, 25]. Here, the measured critical concentration was $c_c = 3$ nM, which is $c_{c,\text{actin}}/c_{c,\text{MreB}} = 55$ times smaller than actin.

A recent experiment involving fluorescent-labelled single molecules of MreB in *C. crescentus* has lead to a direct measurement of in vivo movement of elements of the helical structure [44]. The single molecules were reported to move at $6.0\,\text{nm/s}$. If this is interpreted as treadmilling along a stationary cable (as the authors do), then $\lambda = 1.2\,\text{s}^{-1}$, which is nearly twice the value for actin.

The above has led us to two options for estimating the in vivo kinetic parameters of MreB. The first is to simply use the actin kinetics, while the second is to use Eqs. 3.10 - 3.13, along with the critical concentration from *Thermotoga* and treadmilling rate estimated in [44], to generate alternative kinetics. We refer to these kinetic parameters as *Thermotoga*-scaled kinetics, and they represent the least-intrusive modification of actin polymerization dynamics to make it consistent with all observed MreB dynamics.

The true kinetic rates of MreB in vivo will certainly differ from either eukaryotic

Symbol	Value	Meaning	Reference
Eukaryotic actin kinetics			
k_{on}^{b}	$12\,\mu\text{M}^{-1}\,\text{s}^{-1}$	Barbed-end addition rate constant	[66]
k_{on}^{p}	$1.3\,\mu\text{M}^{-1}\,\text{s}^{-1}$	Pointed-end addition rate constant	[66]
k_{off}^{b}	$1.4\,\text{s}^{-1}$	Barbed-end dissociation rate	[66]
k_{off}^{p}	$0.8\,\text{s}^{-1}$	Pointed-end dissociation rate	[66]
c_c	$0.167\,\mu\text{M}$	critical concentration	[68] and Eq. 2.4
λ_{tread}	$0.58\,\text{s}^{-1}$	free treadmilling rate	[68] and Eq. 2.3
α_{on}	0.11	pointed-barbed on-assymmetry	Eq. 3.9
α_{off}	0.57	pointed-barbed off-assymmetry	Eq. 3.9
Symbol	Value	Meaning	Reference
Thermotoga-scaled kinetics			
k_{on}^{b}	$1360\,\mu\text{M}^{-1}\,\text{s}^{-1}$	Barbed-end addition rate constant	Eq. 3.10
k_{on}^{p}	$150\,\mu\text{M}^{-1}\,\text{s}^{-1}$	Pointed-end addition rate constant	Eq. 3.11
k_{off}^{b}	$2.9\,\text{s}^{-1}$	Barbed-end dissociation rate	Eq. 3.12
k_{off}^{p}	$1.7\,\text{s}^{-1}$	Pointed-end dissociation rate	Eq. 3.13
c_c	$0.003\,\mu\text{M}$	critical concentration	[25]
λ_{tread}	$1.2\,\text{s}^{-1}$	free treadmilling rate	[44]
α_{on}	0.11	pointed-barbed on-assymmetry	(from actin)
α_{off}	0.57	pointed-barbed off-assymmetry	(from actin)

Table 3.1: List of parameters from eukaryotic actin (top), and parameters scaled to fit the in vitro critical concentration of *Thermotoga* from [25], as well as an estimate of the in vivo treadmilling rate in *C. crescentus* from [44] (bottom).

actin or our *Thermotoga*-scaled rates. However, they describe two regimes (the high-c_c actin regime and the low-c_c *Thermotoga* regime) to which MreB likely belongs to one of. It is uncertain which is more favoured, and we explore both.

The barbed-end polymerization rate generated by our *Thermotoga* scaling is very high, $k_{\text{on}}^{b} = 1360\,\mu\text{M}^{-1}\,\text{s}^{-1}$. Diffusion sets an upper limit on such association rate constants, defining the diffusion-limited regime. For a spherical protein associating with a fixed point (like the barbed end of a polymer), the diffusion-limited rate constant is $2 \times 10^3\,\mu\text{M}^{-1}\,\text{s}^{-1}$ [39]. Our *Thermotoga*-scaled parameter is slightly below this limit.

3.1.2 Bundle ultrastructure

As discussed in Chapter 2, the MreB helix is not an individual polymer, but rather appears to be a bundle of polymers arranged in a supramolecular array. The ultrastructure of the MreB helix – the precise arrangement, orientation and length distribution of the individual protofilaments that make up the helical bundle – remains a mystery. Several hypotheses have been put forward [25, 28] and Fig. 3.1 illustrates five basic possibilities.

Several of these are less plausible. The slippery arrays in Fig. 3.1E are in disagreement with recent biochemical experiments have demonstrated large lateral interactions between filaments [25, 59]. In fact, it appears that MreB forms bundles spontaneously. Unlike actin, it does not need additional proteins (such as fimbrin in yeast, Sec. 2.3.1) for these strong lateral interactions, further supporting strong bundling.

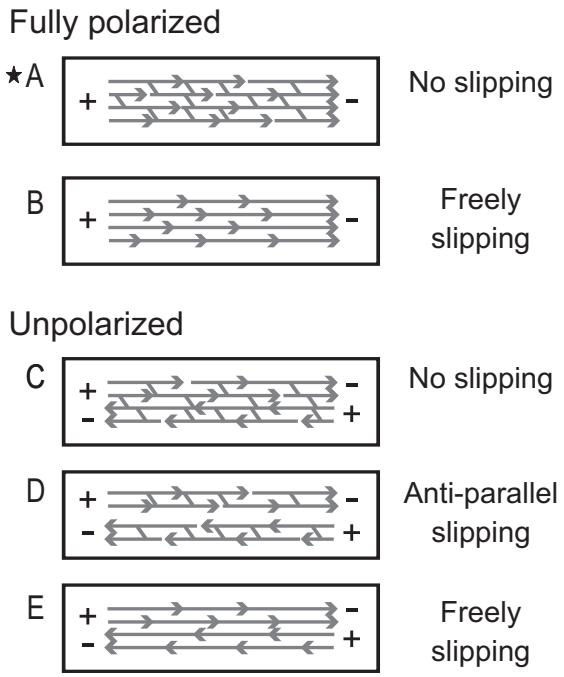

Figure 3.1: Several possible models for the ultrastructure of an MreB cable.

Furthermore, our preliminary simulations of the ultrastructure in Fig. 3.1C led to tapered bundles, as shown in Fig. 3.2. This is a natural consequence of the structure: all antiparallel protofilaments, which cannot slide past each other, treadmill in opposite directions, causing a thinning out at the edges and ultimately a break near the middle once all left-facing protofilaments are occupy the left side, and all right-facing protofilament are on the right. Such tapering is not seen experimentally.

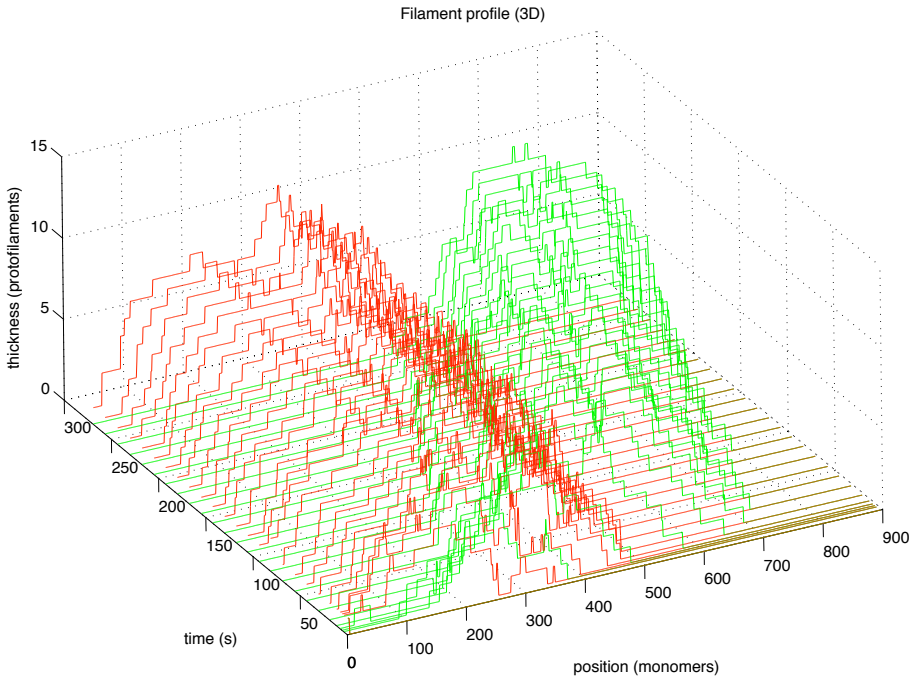

Figure 3.2: Preliminary results of simulations of the ultrastructure in Fig. 3.1C. Protofilaments extend from left to right: left-facing protofilaments are shown in red, while right-facing protofilaments are shown in green. Time progresses towards the back of the page. Initially, the protofilaments faced random directions, and new protofilament were nucleated proportionally to the cytoplasmic concentration (although removing nucleation did not affect the result). As can be seen, the protofilaments separate into two packets, and eventually split near the middle, as anti-parallel protofilaments treadmill away from each other. For this reason, this ultrastructure is rejected.

We therefore consider ultrastructures composed of polarized bundle(s) of protofilaments: either one bundle (Fig. 3.1A) or two antiparallel bundles that freely slide

with respect to each other (Fig. 3.1D). The polymerization properties of these two arrays are identical (their elastic properties will be defined in Sec. 3.2), therefore our results apply to either array.

Here we make the assumption that the bundle is described by a bundle thickness, n, in number of protofilaments. Systematic heterogeneities in the MreB helix thickness have not been observed, and our model does not depend on how the cell regulates the average number of protofilaments in a cross-section of the filament bundle. We will make further assumptions about the arrangement of these n protofilaments.

Although we ascribe a thickness n to the bundle, it contains many more than n protofilaments. As mentioned previously, the protofilaments do not continuously extend from one end of the bacterial cell to the other. Indeed, in *C. crescentus* individual protofilaments appear to be much shorter than the cell length, only 392 ± 23 nm on average [44]. The effect of these lateral free ends is to increase timescales, and to modify transient dynamics. However, in steady-state, exchange of monomers from these free ends is balanced (*i.e.* the net exchange is zero), and the distribution of the individual polymers is irrelevant. For the purposes of finding the steady-state configuration, the mechanical and end-polymerization properties of discontinuous bundles of protofilaments are equivalent to continuous protofilaments. Protofilament association, dissociation and nucleation are thus implicitly included in our model.

3.2 Elasticity

In vitro, MreB typically polymerizes into straight filaments [59]. MreB adopts ring-like coiled configurations in spherical mutants of normally rod-shaped organisms [49], and forms helices in rod-shaped cells [9]. These observations suggest that we model the MreB cable as a long, semi-flexible elastic rod. In this section, we define a model of the elastic properties of the MreB helix.

3.2.1 Cosserat model of an elastic filament

In the elastic Cosserat model [3], a filament is parametrized by its unstretched arclength $s \in [0, L_{fil}]$ where L_{fil} is its total unstretched length. The Hamiltonian of

such a filament is

$$\mathcal{H} = \frac{1}{2}\int_0^{L_{fil}} \left[\left(B\kappa(s)^2 + C\tau(s)^2\right)\, n(s)^2 + EA(1-|\partial_s\vec{r}|)^2\, n(s)\right] ds \tag{3.14}$$

where $\vec{r}(s)$ is the position of the centerline, $\kappa(s)$ is the local curvature, $\tau(s)$ is the local twist and $n(s)$ is the local filament thickness (measured in number of protofilaments). B, C and EA are the bending, twisting and stretching modulii of an individual protofilament, respectively. The symbol ∂_s denotes differentiation with respect to s. This is a variant of the worm-like chain, or Kratky-Porod model [47].

For an actin bundle, the thickness dependence of bending and twisting ranges from linear (n) for slippery protofilaments to quadratic (n^2) for strongly interacting protofilaments and can exhibit more complex state-dependent bending stiffnesses [38], depending on the crosslinkers. For MreB, no crosslinkers are necessary for bundling and lateral interactions appear strong, suggesting a quadratic dependence. Implicit in this n-scaling is also the assumption that cross-sections of the bundle are close-packed and compact rather than being (for example) restricted to a plane like a pan-flute.

Following Antman [3], an elastic filament is described by the position of its centerline $\vec{r}(s)$ and an orthonormal basis of directors $\{\vec{d}_1(s), \vec{d}_2(s), \vec{d}_3(s)\}$ specifying the orientation of its cross-section. This approach has been used extensively for DNA [11] and the bacterial flagellum [42], but is seldom used for eukaryotic actin (though see [53]) since actin does not systematically form structures in vivo that are much smaller than its persistence length. In contrast, MreB forms a helix with a radius of $\approx 400\,\mathrm{nm}$, which is smaller than the persistence length of a single protofilament ($\xi_p = B/k_BT \approx 15\,\mu\mathrm{m}$) and much smaller than ξ_p for a bundle of several protofilaments.

We parametrize the filament by its arclength $s \in [0, L_{fil}]$. The angular strains in the filament are then simply

$$\partial_s \vec{d}_i = \vec{u} \times \vec{d}_i, \tag{3.15}$$

$$\vec{u} = \kappa_1 \vec{d}_1 + \kappa_2 \vec{d}_2 + \tau \vec{d}_3, \tag{3.16}$$

where $\kappa^2 \equiv \kappa_1^2 + \kappa_2^2$ is the curvature and τ is the local twist. We set $\vec{d}_3 \equiv \partial_s \vec{r}$, following the standard shear-free assumption of biopolymers.

3.2.2 Helical equilibria (and the lack thereof)

Although helical equilibria of elastic filaments have been investigated since the 1800's, they remain a challenging, contemporary topic [3,11]. The pioneering work was done by Kirchhoff [45] and Love [56]. In this section we will demonstrate two results; first, that torque is a necessary condition for the helical equilibrium of a filament, and second, that the helix is not the lowest-energy configuration of a filament constrained to lie inside a cylinder.

The helix is assumed to extend throughout the cylindrical part of the cell, but not into the hemispherical poles, in agreement with experiment [41].

The centerline of a helix with pitch angle θ (measured from the cell's axis, $\hat{z}$) and radius R_c is

$$\vec{r}(s) = R_c\cos\left(\frac{\sin\theta}{R_c}s\right)\hat{x} + R_c\sin\left(\frac{\sin\theta}{R_c}s\right)\hat{y} + \cos\theta s\ \hat{z}. \tag{3.17}$$

A helix is shown in Fig. 3.3.

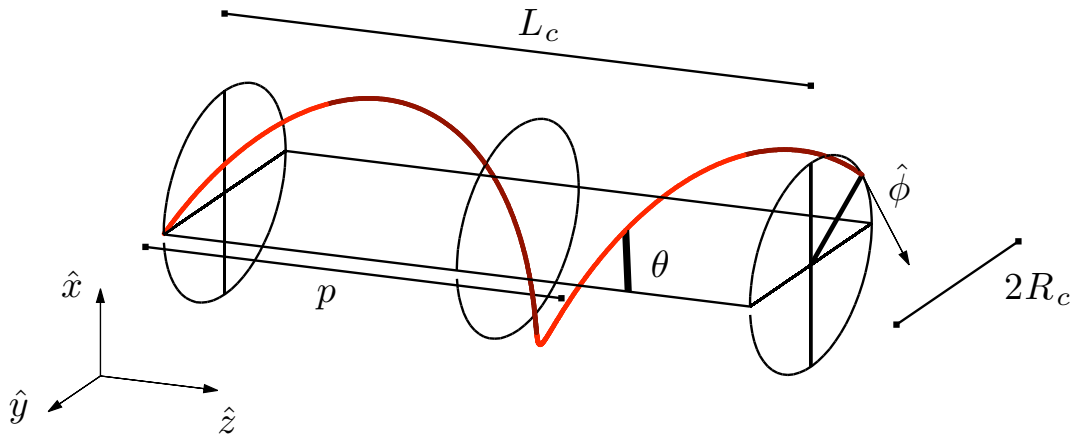

Figure 3.3: A helix. The axis of symmetry lies on the z-axis. The pitch angle θ (measured from the z-axis) is related to the pitch p through Eq. 3.46: longer pitches have smaller θ. The azimuthal direction is denoted $\hat{\phi}$ (Eq. 5.2). The cylinder containing the helix has length L_c and radius R_c. The origin shown has been shifted away from the center of the cylinder for clarity.

We use the tangent, normal and binormal unit vectors, which are defined as

$$\vec{t}(s) \equiv \partial_s \vec{r}(s), \tag{3.18}$$

$$\vec{n}(s) \equiv \partial_s \vec{t}(s)/|\partial_s \vec{t}(s)|, \tag{3.19}$$

$$\vec{b}(s) \equiv \vec{t}(s) \times \vec{n}(s), \tag{3.20}$$

and the Frenet-Serret Theorem [3], which states that

$$\partial_s \vec{t}(s) = \kappa \vec{n}(s), \tag{3.21}$$

$$\partial_s \vec{n}(s) = -\kappa \vec{t}(s) + \tau_c \vec{b}(s), \tag{3.22}$$

$$\partial_s \vec{b}(s) = -\tau_c \vec{n}(s), \tag{3.23}$$

where τ_c is the torsion of the filament's centerline. Inserting Eq. 3.17 into Eqs. 3.18–3.23, we obtain

$$\kappa = \frac{\sin^2\theta}{R_c} \tag{3.24}$$

and

$$\tau_c = \frac{1}{R_c}\cos\theta\sin\theta. \tag{3.25}$$

The meaning of τ_c is as follows. The directors $\{\vec{d}_1(s), \vec{d}_2(s)\}$ are, in general, a rotation of $\{\vec{n}(s), \vec{b}(s)\}$ through an angle $\beta(s)$. The difference between the physically relevant total twist τ and the centerline torsion τ_c is $\tau_L \equiv \tau - \tau_c = \partial_s \beta$. This is sometimes called the internal twist, or the twist of Love [88], which Love described as the twist which the rod would have "if simply unbent". In situations where the ends are free to rotate in the $\vec{d}_3$ direction (although they may be constrained from translation and/or clamped so as not to rotate in the azimuthal direction), the internal twist τ_L will rotate to eliminate $\tau(s)$, resulting in no net twist. In this sense, in mechanical equilibrium, twisting de-couples from bending and stretching [56].

Now suppose that an end force and end torque (also known as a moment) F and M act on the ends of the helix, in line with its z-axis. The total length change of the helix is $L_{fil} - L_c = L_{fil}(1-\cos\theta)$. The total twist, from Eq. 3.25, is $\tau = \tau_L + \sin\theta\cos\theta/R_c$. Thus, we can define potential energies corresponding to the external force and torque,

$$V_F = FL_{fil}(1-\cos\theta), \tag{3.26}$$

$$V_M = ML_{fil}\left(\tau_L + \frac{1}{R_c}\sin\theta\cos\theta\right). \tag{3.27}$$

The total potential energy of the helix, with end loading, is $\mathcal{H} + V_F + V_M \equiv vL_{fil}$, where v is the energy density. The conditions for equilibrium are

$$\frac{\partial v}{\partial \theta} = \frac{\partial v}{\partial R_c} = \frac{\partial v}{\partial \tau_L} = 0. \tag{3.28}$$

Combining the Hamiltonian, Eq. 3.14 with Eq. 3.26, 3.27 and 3.28 gives

$$F = \frac{B}{R_c}\sin^2\theta \tag{3.29}$$

$$M = \sqrt{BT}(1+\cos\theta) \tag{3.30}$$

These equations were derived by Love [56], and represent necessary and sufficient conditions for a helical configuration to be an equilibrium configuration. As can be seen directly from Eq. 3.30, a nonzero torque is required for any helical equilibrium to exist other than the trivial one, with $\theta = -\pi$.

For a filament not subject to end tension or torque but simply constrained to lie inside a cylinder, it is straightforward to show that the helix is not the natural configuration. There are a multitude of configurations with lower total elastic energies, meaning the helix is not the ground state. We solve three cases exactly, illustrated in Fig. 3.4.

Energy of a helix

A helix (Fig. 3.4A) with pitch angle given by $\cos\theta = L_c/L_{fil}$ has constant curvature, and the total bending energy is

$$E_h = \frac{BL_{fil}}{2R_c^2}\left(1 - \left(\frac{L_c}{L_{fil}}\right)^2\right)^2. \tag{3.31}$$

Since $E = \int (B/2)\kappa^2 ds$, it is convenient to define the total square curvature,

$$\mathcal{C} \equiv \int_0^{L_{fil}} \kappa^2 dl. \tag{3.32}$$

For $L_c = 3\,\mu$m, $R_c = 400\,$nm, and $L_{fil} = 10\,\mu$m, this equation gives $\kappa = 1.82\,\mu\text{m}^{-1}$ and $\mathcal{C}_h = 33.1\,\mu\text{m}^{-1}$. For $Bn^2 = 10^4\,\text{pN nm}^2 \cdot 5^2$, the energy is $E_h = 7100\,\text{pN nm}$.

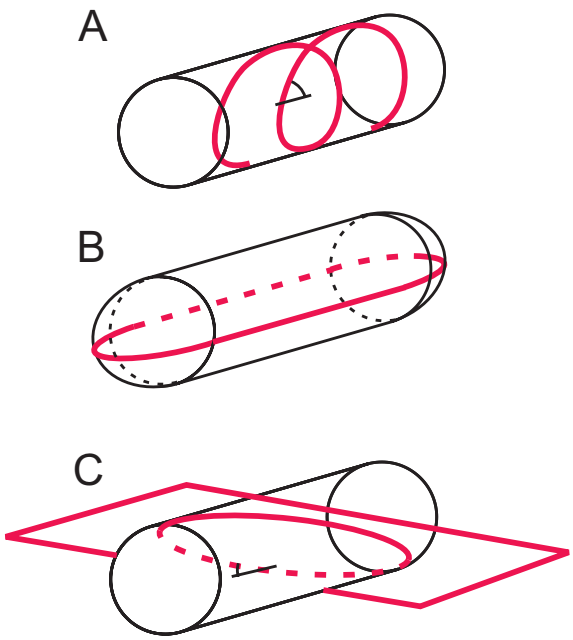

Figure 3.4: Three configurations of an elastic filament inside a cylindrical cell. A) Helix. The angle indicated by the arc is the pitch angle, θ. B) If the filament is allowed to enter the hemispherical end caps, it can make a paperclip-like configuration. C) The maximal ellipse obtained by slicing the cylinder along its diagonal. The angle indicated by the arc is $\cos^{-1}\sqrt{\beta}$.

Energy of a paperclip

If the filament is allowed to extend into the hemispherical cell poles, it can adopt the periodic paperclip-like configuration shown in Fig. 3.4B. One repeat of this configuration has length $L_{fil1} = 2L_c + 2\pi R_c$ and total square curvature

$$\mathcal{C}_{p1} = \frac{2\pi}{R_c}. \tag{3.33}$$

For $L_c = 3\,\mu$m, $R_c = 400\,$nm, we get $L_{fil1} = 9.14\,\mu$m, the curvature in the poles is $\kappa = 2\,\mu\text{m}^{-1}$, and $\mathcal{C}_{p1} = 12.5\,\mu\text{m}^{-1}$. A filament of length $L_{fil} = 10\,\mu$m whose starting point is randomly placed along this configuration will have total square curvature

$$\mathcal{C}_p = \frac{L_{fil}}{L_{fil1}}\mathcal{C}_{p1} = \frac{L_{fil}}{2L_c + 2\pi R_c}\frac{2\pi}{R_c}. \tag{3.34}$$

For $L_{fil} = 10\,\mu\text{m}$, $\mathcal{C}_p = 13.7\,\mu\text{m}^{-1}$. For $Bn^2 = 10^4\,\text{pN}\,\text{nm}^2 \cdot 5^2$, the energy is $E_p = 2925\,\text{pN}\,\text{nm}$.

Energy of an ellipse

The maximal ellipse obtained by slicing the cylindrical part of the cell, as shown in Fig. 3.4C, has semimajor axis $a = \sqrt{R_c^2 + (L_c/2)^2}$, semiminor axis $b = R_c$ and eccentricity

$$e = \sqrt{1 - b^2/a^2} = \frac{L_c}{\sqrt{4R_c^2 + L_c^2}}. \tag{3.35}$$

Expressing the curvature in polar coordinates is undesirably messy, so we instead parametrize the curve by

$$x(t) = a\cos t, \tag{3.36}$$

$$y(t) = b\sin t, \tag{3.37}$$

where $t \in [0, 2\pi]$. Note that t is not the polar angle θ, but rather is related to it by $\tan\theta = (b/a)\tan t$. The distance from the origin is

$$r(t) = \sqrt{a^2\cos^2 t + b^2\sin^2 t} \tag{3.38}$$

and the curvature is (using the Frenet-Seret theorem, Eq. 3.21)

$$\kappa(t) = \frac{ab}{b^2\cos^2 t + a^2\sin^2 t}, \tag{3.39}$$

which has a maximum of $\kappa_{max} = a/b^2$ and minimum of $\kappa_{min} = b/a^2$ at the two vertices, respectively. The perimeter of the ellipse is $L_{fil1} = 4aE(e)$ where $E(x)$ is the complete elliptic integral of the second kind.

The total square curvature of one wavelength is

$$\mathcal{C}_{e1} = 4\int_0^{\pi/2} \kappa(\theta)^2 r(\theta) d\theta = 4\int_0^{\pi/2} \kappa(t)^2 r(t) \left(\frac{d\theta}{dt}\right) dt. \tag{3.40}$$

Now define $\beta = b/a = \sqrt{1 - e^2}$. The above expression becomes

$$\mathcal{C}_{e1} = 4\frac{\beta^3}{a}\int_0^{\pi/2} \frac{(\cos^2 t + \beta^2\sin^2 t)^{1/2}}{(\beta^2\cos^2 t + \sin^2 t)^3} \frac{1 + \tan^2 t}{1 + \beta\tan^2 t} dt. \tag{3.41}$$

This integral has no closed form solution. For $L_c = 3\,\mu$m, $R_c = 400\,$nm, we get $L_{fil1} = 7.0\,\mu$m and $\mathcal{C}_{e1} = 16.4\,\mu\text{m}^{-1}$. For $L_{fil} = 10\,\mu$m, $\mathcal{C}_e = 23.4\,\mu\text{m}^{-1}$, and for $Bn^2 = 10^4\,\text{pN}\,\text{nm}^2 \cdot 5^2$, the energy is $E_e = 5000\,\text{pN}\,\text{nm}$.

Both the paperclip configuration and the elliptic configuration have less energy than the helical configuration by at least 40%. The conclusion of this section and the previous is that an elastic filament inside a cylindrical cell will not buckle into a helix in the absence of external torques. This conclusion will be verified numerically using finite element analysis in Chapter 5. There must be some external forces acting on the MreB cables other than forces normal to the cell wall (which contribute no axial torque) in order for otherwise straight cables to buckle into a helix.

3.2.3 Variational estimate of effective force

By imposing the observed helical configuration we can use variational techniques to estimate the effective forces working against monomer addition at the filament tips. Although we do not know the nature of the external forces acting to maintain a helical configuration, this derivation is independent of their details.

Using the linearly elastic Hamiltonian from Eq. 3.14, plugging in Eq. 3.17 and $L_c = L_{fil}\cos\theta$, we find the variations of the Hamiltonian with respect to cell length L_c, cell radius R_c and filament length L_{fil},

$$\frac{\partial \mathcal{H}}{\partial L_c} = -\frac{2B}{R_c^2}\sin^2\theta\cos\theta\langle n^2\rangle, \tag{3.42}$$

$$\frac{\partial \mathcal{H}}{\partial R_c} = -\frac{BL_{fil}}{R_c^3}\sin^4\theta\langle n^2\rangle, \tag{3.43}$$

$$\frac{\partial \mathcal{H}}{\partial L_{fil}} = -\frac{B}{2R_c^2}\sin^2\theta\,(1+3\cos^2\theta)\langle n^2\rangle. \tag{3.44}$$

Regardless of any mechanisms holding the MreB bundle in a helical configuration, one additional monomer must provide an energy of $(-a_0\partial\mathcal{H}/\partial L_{fil})$ to polymerize itself to the tip of the longest protofilament(s). This provides an estimate for the force acting upon the tip of the filament bundle,

$$F_B = \begin{cases} f_B\sin^2\theta\,(1+3\cos^2\theta)\langle n^2\rangle & L_{fil} > L_c \\ 0 & L_{fil} < L_c, \end{cases} \tag{3.45}$$

where we define $f_B \equiv B/2R_c^2 \approx 0.031pN$ to be the elastic force scale. Many of our results reflect the fact that we work in an interesting regime where elastic forces, F_B, and the polymerization force scale, $f_0 \equiv k_BT/a_0 = 0.80\,\mathrm{pN}$, are similar in magnitude.

The pitch p and pitch angle θ of the helix are related by

$$p = \frac{2\pi R_c}{\tan\theta}, \quad \cos\theta = \frac{L_c}{L_{fil}}. \tag{3.46}$$

The bundle thickness $n(s)$ need not be spatially homogeneous. If it exhibits significant inhomogeneity along the bundle, by analogy with actin cables in yeast [43], then the appropriate average thickness n is the root-mean-square average thickness along the bundle length. Other than the buckling point at $L_{fil} = L_c$, F_B is independent of L_{fil} for a given θ. As the pitch p vanishes, with $\theta \to \pi/2$, then $F_B \to f_B n^2$. The force F_B has a maximum of $F_B^{\max} \equiv \frac{4}{3} f_B n^2$ at $\theta^* = \arctan\sqrt{2} \approx 0.96 \approx 55^\circ$.

The other variations

Insight into the MreB helix can be extracted from the other variations as well. We describe them here as an aside.

Eq. 3.42 provides an estimate for the force generated by the MreB cytoskeleton against the cell's end caps. An estimate for the difference in longitudinal spring constant of the cell with and without a properly formed MreB helix is,

$$\Delta k_{cell} \approx \frac{\partial^2 \mathcal{H}}{\partial L_c^2} = \frac{2B}{L_c R_c^2} \cos\theta(3\cos\theta - 1)n^2. \tag{3.47}$$

For $p = 1\,\mu$m and $n = 15$, this yields $4 \times 10^{-4}\,\mathrm{pN/\,nm}$. For *E. coli*, the spring constant of the entire cell is $\approx 10^3\,\mathrm{pN/\,nm}$ [93] and is much larger for *B. subtilis*, thus the spring constant differential provided by the MreB helix is insignificant. Similarly, Eq. 3.43 provides an estimate for the radial line pressure the helix exerts on the lateral walls:

$$\frac{F_{\hat{r}}}{L_{fil}} \approx \frac{B}{R_c^3} \sin^4\theta n^2. \tag{3.48}$$

For $p = 1\,\mu$m and $n = 15$, this yields $0.03\,\mathrm{pN/\,nm}$. Eq. 3.48 represents a force contrast between pushing the cell wall directly above the helix and elsewhere. A bundle with $n = 15$ has approximate thickness $a_0\sqrt{n} \approx 20\,\mathrm{nm}$ and the local excess pressure over the cables is $\approx 5 \times 10^{-3}\,\mathrm{pN/\,nm^2}$. In comparison, turgor pressure inside *E. coli* has

been measured at $\approx 0.1\,\mathrm{pN}/\,\mathrm{nm}^2$ [93], indicating that the rigidity of the MreB bundles does not directly provide significant structural support for the cell well.

3.2.4 Energy scales and approximations

The stretching modulus of a filament bundle of actin is $nEA \approx 40n\,\mathrm{pN}$ where n is the number of protofilaments in a typical cross-section of the bundle. For a typical filament with $n = 15$, the energy scale to stretch the filament by monomer addition is $\Delta U_{stretch} = EA\,na_0 \approx 2 \times 10^3\,\mathrm{pN\,nm}$, whereas a comparable energy scale for bending the helix is $\Delta U_{bend} = Ba_0/4R_c^2n^2 \approx 70\,\mathrm{pN\,nm}$. Therefore the no-stretch assumption is appropriate in this case.

At physiological temperatures, all cellular components undergo thermal fluctuations of the order k_BT. However, a typical helical bundle with $n = 5$ and $p = 1\,\mu\mathrm{m}$ has an elastic energy of $U = 3.5 \times 10^5\,\mathrm{pN\,nm} \gg k_BT = 4.1\,\mathrm{pN\,nm}$. We therefore assume that the helical pitch does not significantly fluctuate due to thermal effects. This is a consequence of the fact, stated earlier, that the structures MreB forms have length scales much smaller than the persistence length of the cables.

3.2.5 Euler buckling

It is intersting to consider the behavior of the filament as it approaches the length of the cell and first encounters a compressive force upon its tips, as hypothesised in Eq. 3.45. The filament's equilibrium configuration, that is, straight, is only stable below a certain force. Above this limit, the filament will buckle under the compressive force and adopt a non-straight configuration. This phenomenon is known as Euler buckling [3, 52].

The critical force can be found using the so-called beam equation, which is a consequence of the Hamiltonian in Eq. 3.14, along with the assumption that the deformations are small enough that $r_z(s) \approx s$. The beam equation is used extensively in mechanical engineering. It is a fourth-order differential equation that states

$$B\frac{\partial^4 r_x}{\partial z^4} + F\frac{\partial^2 r_x}{\partial z^2} = 0, \tag{3.49}$$

$$B\frac{\partial^4 r_y}{\partial z^4} + F\frac{\partial^2 r_y}{\partial z^2} = 0. \tag{3.50}$$

The trivial solution, $r_x(s) = r_y(s) = 0$, always exists. To find non-trivial solutions, we note that both $r_x z = \sin(knz)$ and $r_x z = \cos(knz)$ satisfy Eq. 3.49 with $k = \sqrt{F/B}$ and $n \in \{0, 1, 2, ...\}$. The condition that the ends are fixed is $r_x(0) = r_x(L_{fil}) = 0$. Further constraining the ends imposes further boundary conditions, for instance clamping them such that $\partial^3 r_x(0)/\partial z^3 = \partial^3 r_x(L_{fil})/\partial z^3 = 0$. However, the basic condition leads to

$$\sin(kL_{fil}) = 0 \implies F_E = \pi^2 \frac{B}{L_{fil}^2}. \tag{3.51}$$

where F_E is the critical force for Euler buckling. Thus, there is a regime in which the filament can be exposed to a non-zero force $F < F_E$ and may still remain straight. This tip force is comparable to our proposed tip force in Eq. 3.45 when

$$\pi^2 \frac{B}{L_{fil}^2} \geq \frac{B}{2R_c^2} \sin^2\theta \, (1 + 3\cos^2\theta). \tag{3.52}$$

For the standard cell geometry $L_c = 3\,\mu$m, $R_c = 400\,$nm, this occurs at $\theta = 18^\circ \implies p = 8\,\mu$m, a pitch much larger than is biologically relevant. For larger θ we are far above F_E and do not expect any metastable unbuckled configurations.

3.3 Other possible sources of pitch

The shooting helix

One of the simplest explanations of the abundance of helices in bacteria is that if a polymer is membrane-bound and simply starts growing in some direction, without any bending resistance, then it will form a helix, a ring or an axial line (which are degenerate helices). We explore the consequences of this model here.

Suppose a polymer nucleus were oriented randomly at one end of the cell so that its polymerization axis made an angle θ with the cell's axis. For now, suppose θ is uniformly distributed in the first quadrant. That is,

$$\theta \sim f_\theta(\theta) = \begin{cases} 2/\pi & 0 \leq \theta \leq \pi/2 \\ 0 & \text{otherwise} \end{cases} \tag{3.53}$$

If this nucleus grows into a polymer without rotating, extending into a helix that runs the length of the cell, the pitch of this helix will be given by Eq. 3.46,

$$p = \frac{2\pi R_c}{\tan\theta}. \tag{3.54}$$

That is, $p = h(\theta)$ where for clarity we define

$$h(x) = \frac{2\pi R_c}{\tan x} \tag{3.55}$$

The tan function is monotonic increasing in $[0, \pi/2]$ thus h is monotonic decreasing. To find the distribution of $p \sim g_p(p)$, we use the transformation equation [72],

$$g_p(p) = f_\theta(h^{-1}(p)) \left| \frac{dh^{-1}}{dp}(p) \right|. \tag{3.56}$$

and obtain

$$p \sim g_p(p) = \begin{cases} 4R_c / \left(p^2 + (2\pi R_c)^2\right) & 0 \leq p \leq \infty \\ 0 & \text{otherwise} \end{cases} \tag{3.57}$$

This function is illustrated by the red curve in Figure 3.5. Note that

$$\int_0^\infty g_p(p)dp = \int_0^\infty \frac{4R_c}{p^2 + (2\pi R_c)^2} dp = 1 \tag{3.58}$$

and

$$\langle p \rangle = \int_0^\infty p g_p(p)dp = \int_0^\infty \frac{4R_c p}{p^2 + (2\pi R)^2} dp \to \infty,$$

$$\langle p^2 \rangle = \int_0^\infty p^2 g_p(p)dp = \int_0^\infty \frac{4R_c p^2}{p^2 + (2\pi R_c)^2} dp \to \infty.$$

The distribution is well-defined but has no mean or variance. The mode (maximum) is at $p = 0$. The cumulative distribution function of p is

$$G_p(p) = \int_0^p g_p(q)dq = \frac{2}{\pi} \arctan\left(\frac{p}{2\pi R_c}\right). \tag{3.59}$$

Solving for $G_p(p) = 0.50$ gives the median, at $p = 2\pi R_c$ (*i.e.* when $\theta = \pi/4$). Note that if the range of θ is increased to $[-\pi/2, \pi/2]$ and the pitch is taken to be strictly positive, the function h becomes even and the results are identical. It is probably not relevant that the distribution of pitches has no mean, however it does demonstrate that the distribution is extremely wide and has an extremely long tail — that is, many helices established in this way have large pitches. A bacteria using such a mechanism to establish helices would have a very difficult time controlling their pitches, and in particular, avoiding nearly-straight configurations.

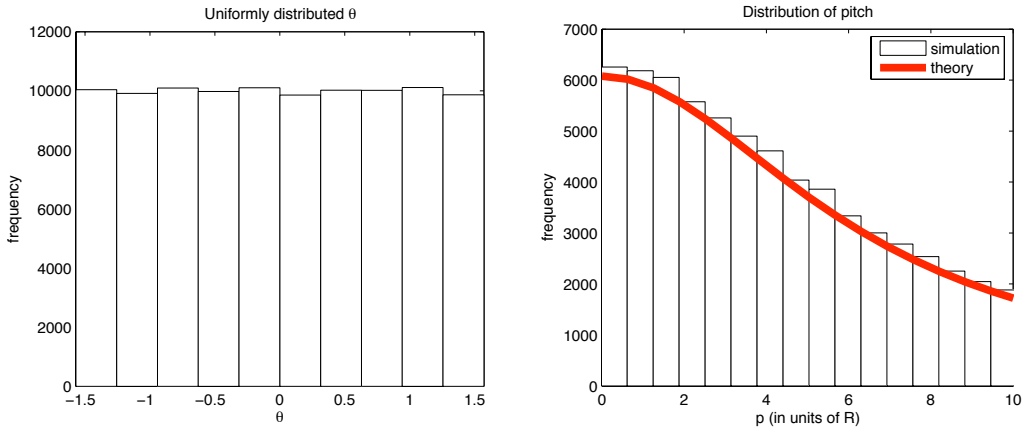

Figure 3.5: The shooting model for the establishment of a helical pattern in a cell. (Left) Uniformly distributed pitch angle $\theta \in [-\pi/2, \pi/2]$. ($N = 10^5$). (Right) The resulting distribution of pitches. The histogram represents data from simulation, $N = 10^5$, while the curve shows analytic prediction from Eq. 3.57. The function is non-zero for all positive p and the plot was cut at $p = 10R$ for clarity.

3.4 Conclusions

In this chapter we presented a model of the MreB helix inside a cylindrical cell. First, individual protofilaments were considered on a molecular scale using a simple polymerization model, where changes occur in nanometers (the size of an MreB monomer). Then, the ultrastructure of the cables was considered, where the cross section may be tens of monomers wide. Finally, the cable's elastic properties within the cell was considered, in which it forms structures several microns long. Three significant differences between MreB and actin were highlighted: the lack of a double-helix polymer, which leads to a slight change in polymerization dynamic equations; the distinct and unknown kinetic rates; and the lateral bundling interactions of the protofilaments.

In the following chapters, we will explore the consequences of this model. However we have already stated several novel conclusions. First, the bundle's ultrastructure cannot be such that all protofilaments are laterally attached so as not to slip, and also such that their orientations are random, since this would lead to tapering and breaking. Second, the helix is not the default configuration for an elastic filament inside a cylindrical cell. Third, the mechanical properties of the MreB structure are

negligible compared to the cell's other mechanical elements, such as the peptidoglycan stiffness and the turgor pressure. And fourth, filaments generated by randomly oriented nuclei indeed form helices, but often with very large pitches.

Chapter 4

Results: Polymerization consequences

The model described in the previous chapter leads to the following interpretation of the establishment of the MreB helix. A cell contains an abundance of $N = N_0$ molecules of MreB. A bundle of protofilaments, n thick, is formed somewhere inside the cell, and it begins to grow, reducing the number of cytoplasmic monomers, N, and consequently the concentration, c. As the bundle length, L_{fil}, grows longer than the cell length, L_c, it is forced to buckle into a helical configuration, at which point forces on its ends reduce the polymerization rate. These forces increase as the bundle gets longer and longer, meanwhile the concentration of free monomers decreases. The bundle continues to grow until the elastic forces are balanced by the polymerization forces, and the helix reaches a steady state.

In this steady state, the helical configuration of the bundle is static, however the individual monomers are not. Subunits incorporated into the bundle continue to treadmill from the barbed end pole towards the pointed end pole, and then depolymerize into the cytoplasm where they await reincorporation.

The helical configuration and the effective tip force in Eq. 3.45 assume the helix is in mechanical equilibrium, which may not be true if the dynamics of polymerization are fast enough to continually hold the helix in (mechanical) non-equilibrium. However, this is not the case: an estimate for the timescale for elastic reorganization of the MreB helix can also be obtained from the relaxation time of the lowest hydrodynamic mode in the filament [39],

$$t_{elastic} \sim \frac{2^6}{(3\pi)^4 \ln(2)} \frac{\eta L_{fil}^4}{B} \approx 0.02\,\mathrm{s}, \tag{4.1}$$

where η is the cytoplasmic viscosity. In comparison, the characteristic time for polymer elongation is given by the steady-state treadmilling rate,

$$t_{poly} \sim \frac{1}{\lambda_{tread}} = \frac{k_{\mathrm{on}}^p + k_{\mathrm{on}}^b}{k_{\mathrm{off}}^p k_{\mathrm{on}}^b - k_{\mathrm{off}}^b k_{\mathrm{on}}^p} \approx 1.7\,\mathrm{s}. \tag{4.2}$$

Since $t_{elastic} \ll t_{poly}$ we can assume that elastic relaxation is fast compared to the polymerization dynamics of interest.

The main result of this chapter is a solution for this steady state, and in particular, a relationship between the four system variables that describe it: total molecular abundance, N_0, the bundle thickness n, the cytoplasmic concentration of monomers, c and the helical pitch, p. We establish this relationship under several assumptions, along with other details of the steady state.

4.1 Mean-field results

By neglecting stochastic fluctuations, we can solve analytically for the relationship between pitch, total monomer number and cytoplasmic concentration. By equating the average velocities of barbed polymerization and pointed depolymerization in Eqs. 3.1 and 3.2, we find the force at which an the filament will cease to grow and begin treadmilling,

$$F = f_0 \ln\left(\frac{c}{c_c}\right). \tag{4.3}$$

In mechanical equilibrium, this force must be balanced with the effective force in Eq. 3.45. If $n_{tip} \in [1, n]$ protofilaments reach each tip, then the force is shared between them, and

$$F_B = f_0 \ln\left(\frac{c}{c_c}\right) n_{tip} = f_B \sin^2\theta \,(1 + 3\cos^2\theta)\langle n^2\rangle. \tag{4.4}$$

We also have conservation of total number of monomers. The length of the filament is $L_{fil} = Lc/\cos(\theta)$, and is thus composed of $\langle n\rangle Lc/(a_0\cos(\theta))$ monomers. The total number of monomers is this plus the number in the cytoplasm, so

$$N_0 = N_C c + \langle n\rangle \frac{L_c}{a_0}\frac{1}{cos\theta}, \tag{4.5}$$

where N_0 is the total number of monomers, N_C is the number of molecules per μM for a given cell volume, defined in Eq. 3.6, and $\langle n\rangle$ is averaged along the length of the helix. Together these equations give a relationship between concentration and pitch angle,

$$\ln\left(\frac{c}{c_c}\right) n_{tip} = \frac{f_B}{f_0}\sin^2\theta \,(1 + 3\cos^2\theta) \times \left((N_0 - N_C c)^2 \,\frac{{a_0}^2}{L_c}\,\cos^2\theta\right), \tag{4.6}$$

and an equivalent relationship between bulk thickness and pitch angle,

$$\ln\left(\frac{N_0}{N_C c_c} - \langle n\rangle \frac{L_c}{a_0 N_C c_c}\frac{1}{\cos\theta}\right) n_{tip} = \frac{f_B}{f_0}\sin^2\theta\,(1+3\cos^2\theta)\langle n^2\rangle. \tag{4.7}$$

These equations are independent of the kinetic rates except through the critical concentration.

4.1.1 Eukaryotic actin kinetics

Eqs. 4.6 and 4.7 have no closed-form solution. However, they can be solved numerically provided $N_0 - nL_{fil}/a_0 > N_C c_c$, that there are enough monomers left in the cytoplasm to achieve the critical concentration, and $N_0/n > L_c/a_0$, that there are enough subunits to span the cell length n times. We do this for the two cases $n_{tip} = 1$ and $n_{tip} = n$, shown in Figs. 4.1-4.2. As expected, the assumption $n_{tip} = 1$ produces much larger pitches and higher cytoplasmic concentrations. For bundle thicknesses $n > 5$, the pitches are too long to be physiologically relevant. Both these results can be compared with results from stochastic simulation we will find in Sec. 4.2.

4.1.2 *Thermotoga*-scaled kinetics: Explicit results for low-c_c

For the *Thermotoga*-scaled kinetics from Tables 3.1.1, the only relevant change is in the critical concentration. However, we are now in a regime where

$$c_c \ll \frac{N_0}{N_C} e^{-f_B/f_0} \tag{4.8}$$

and we can obtain approximate explicit solutions for Eq. 4.6. The concentration scale is low, so $c \ll N_0/N_A$. Thus, the c term in Eq. 4.5 can be neglected and Eq. 4.7 can be solved for θ, and in turn for the pitch (Eq. 3.46) and then c. The pitch and concentration are then given by

$$p(N_0, n) = \frac{2\pi R_c}{\sqrt{\left(\frac{L_c n}{N_0 a_0}\right)^2 - 1}}, \tag{4.9}$$

and

$$c(N_0, n) = c_c \exp\left[\frac{f_B}{f_0}\left(1 - \left(\frac{L_c n}{N_0 a_0}\right)^2\right)\left(1 + 3\left(\frac{L_c n}{N_0 a_0}\right)^2\right)\frac{n^2}{n_{tip}}\right]. \tag{4.10}$$

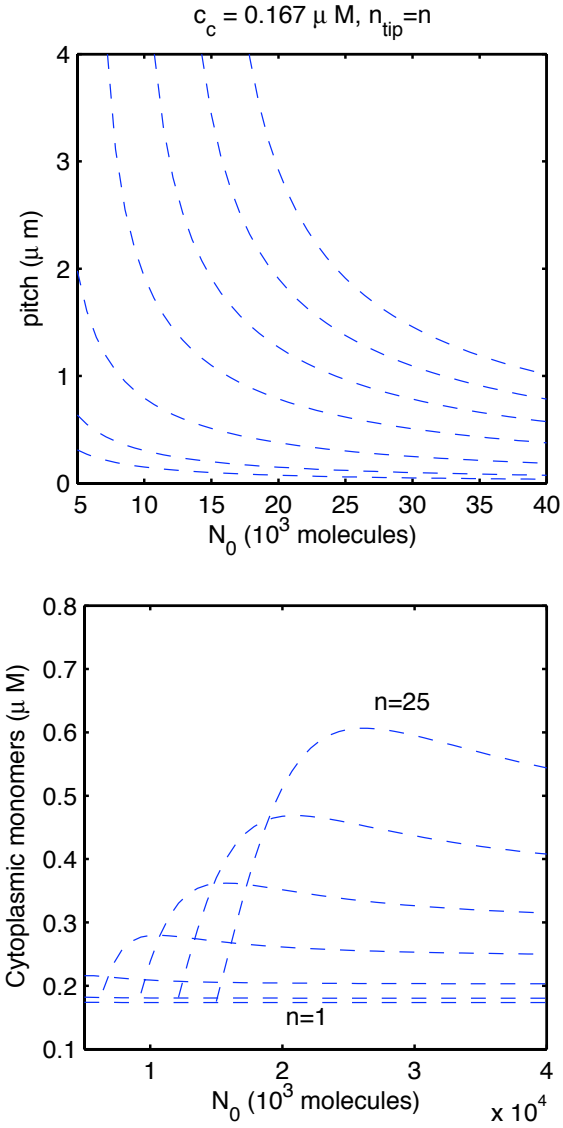

Figure 4.1: Steady-state configuration parameters in the mean-field approximation with actin kinetics, assuming that all protofilaments contributes to the polymerization force, $n_{tip} = n$. These curves were found by numerically solving Eq. 4.6.

The interpretation of these solutions is straightforward. Eq. 4.9 states that effectively all monomers join the bundle. Its length is simply $L_{fil} = a_0 N_0/n$, and its pitch follows from the geometry. Eq. 4.10 states that the concentration will adjust to whatever is needed to provide the force required by Eq. 4.9. Its non-monotonic character is inherited from the non-monotonic character of the force equation, Eq. 3.45.

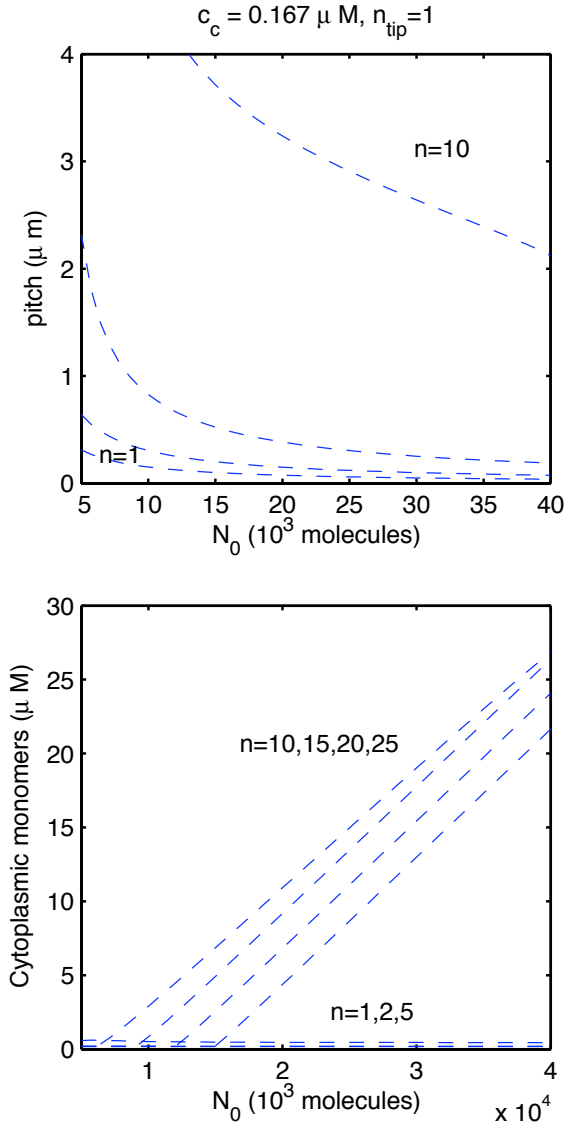

Figure 4.2: Steady-state configuration parameters in the mean-field approximation with actin kinetics, assuming that one protofilament contributes to the polymerization force, $n_{tip} = 1$. These curves were found by numerically solving Eq. 4.6. The resulting pitches and concentrations are much higher than in Fig. 4.1, where $n_{tip} = n$.

These functions are shown in Fig. 4.3. The explicit results from Eqs. 4.9 and 4.10 are identical to curves obtained from finding numerical solutions to Eq. 4.6. These results will further be compared with full stochastic simulations in the next section.

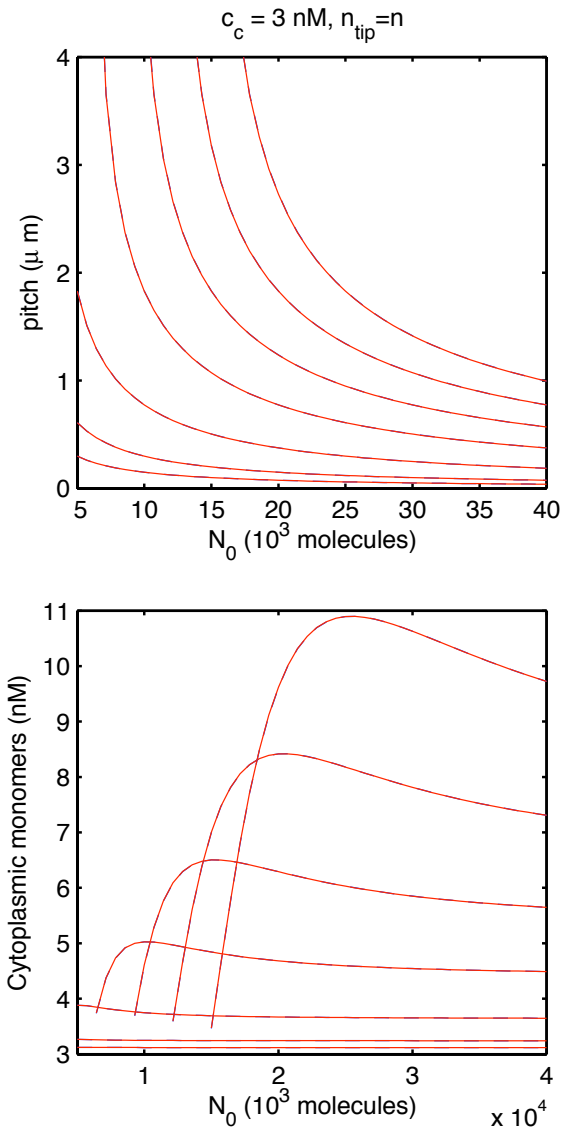

Figure 4.3: Steady-state configuration parameters in the mean-field approximation with *Thermotoga*-scaled kinetics, assuming that all protofilaments contributes to the polymerization force, $n_{tip} = n$. The explicit results from Eqs. 4.9 and 4.10 are indistinguishable from curves obtained from finding numerical solutions to Eq. 4.6. Note the scale is now in nM= $10^{-3}\,\mu$M.

4.2 Stochastic simulation

In a typical *B. subtilis* cell of volume $1.9\,\mu\text{m}^3$, only 4 unpolymerized monomers are necessary to achieve the critical concentration of *Thermotoga* MreB, $c_c = 0.003\,\mu$M,

suggesting that stochastic effects, due to the discrete molecular nature of the polymerizing monomers, may be significant. Similarly, the number of protofilaments in a typical cross-section of the MreB helix is small (less than 20), and the number of protofilaments in contact with the cell wall at the helix tips, n_{tip}, is even smaller. For these reasons, a fully stochastic simulations may be needed to explore the impact of stochastic effects in this system, especially in the low-c_c regime.

We simulated n protofilaments that grew and shrank stochastically within a common pool of N_0 monomers according to the force-dependent polymerization rates and force-independent depolymerization rates described in Sec. 3.1. The times between polymerization or depolymerization events were chosen from appropriate exponential distributions. This is sometimes called the Gillespie algorithm [34]. The forces on each protofilament tip were determined by the constraint force on the bundle, Eq. 3.45, divided among the leading filaments at that tip ($1 \leq n_{tip} \leq n$). The filament bundle was studied once it reached a steady-state. The length of each of the n filaments and the monomer concentration continued to fluctuate within the steady-state, as did the number of protofilament tips, n_{tip}, at a given end of the filament bundle.

For a given cell geometry (L_c and R_c) and total number of monomers (N_0), each bulk thickness n yields a unique helical steady-state configuration with a particular pitch p and average cytoplasmic monomer concentration c_{ss}. As seen in Fig. 4.4, as the abundance N_0 increases for a given number of protofilaments n, the pitch decreases due to longer bundles. Conversely, at a given N_0, thicker bundles (larger n) leads to larger pitches.

The gray rectangles in Fig. 4.4 represent independent experimental measurements of MreB abundance and cable pitch in *B. subtilis* [10,41] and *E. coli* [50]. In *B. subtilis*, if the three MreB isoforms (MreB, Mbl, and MreBH) bundle together into a triplex structure, the total number of monomers should be the sum from each homologue, which we estimate is $23000 - 40000$. We see that with current experimental estimates, *E. coli* has $n \in [3, 16]$ protofilaments in each polarized MreB helical bundle. Expressed independently in *B. subtilis* we estimate that Mbl has $n \in [9, 21]$, while MreB has $n \in [3, 7]$. However, if all of the isoforms are expressed together, the triplex structure

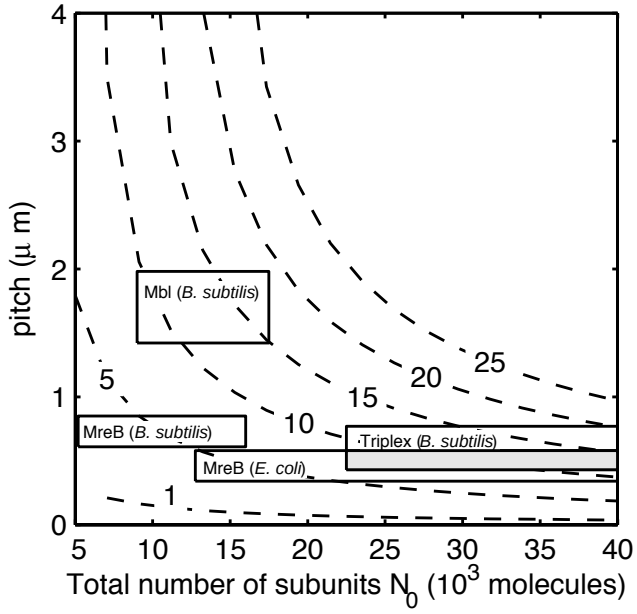

Figure 4.4: Steady-state pitch p vs. total molecule number N_0 for various filament bulk thicknesses n as predicted by stochastic simulation. The mean-field plot is indistinguishable from this due to the low cytoplasmic concentration, and between actin kinetics and *Thermotoga*-scaled kinetics. The rectangles represent approximate regions of experimental relevance from [10, 41, 50]. In *B. subtilis*, if the three isoforms bundle together into a triplex structure, the number of monomers will be the sum of each homologue.

has a distinct pitch. Under the assumption that the isoforms are mutually non-slipping, we estimate $n \in [8, 21]$ in the triplex.

The concentration of MreB in monomeric form shown in Fig. 4.5 is low, representing less than 0.1% of the total cellular MreB. This is in contrast to the same model using eukaryotic actin kinetics, for which $1 - 5\%$ is monomeric (Fig. 4.6), and in dramatic contrast with observations of FtsZ polymerization, for which 30% is associated with the Z-ring and 70% is diffuse in the cytoplasm in vivo [81]. Notwithstanding, the average monomeric concentration of MreB is significantly above the critical concentration due to a reduced polymerization rate which arises from the constraining force at the bundle tips.

The shape of the curves in Fig. 4.5 can be understood by examining the explicit

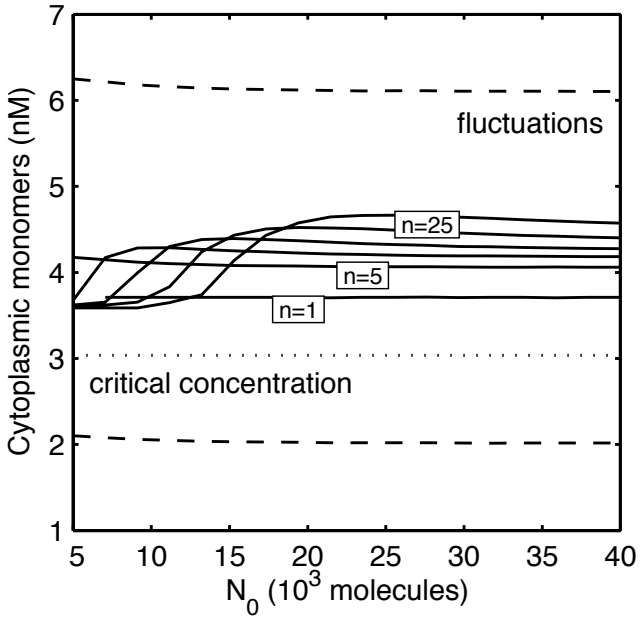

Figure 4.5: Steady-state cytoplasmic concentration c_{ss} of MreB monomers vs. total monomer number N_0 from stochastic simulation for n protofilaments, showing $n = 1$, 5, 10, 15, 20, and 25. The dotted line represents the critical concentration. The dashed line illustrates the large standard deviation of stochastic fluctuations in steady-state, for $n = 5$. For all n, relative fluctuations were $50\%\pm5\%$ and absolute fluctuations were within $0.2nM$ of those shown for $n = 5$. These simulations used *Thermotoga*-scaled kinetics.

results from the mean-field approximation in Eq. 4.10. As stated previously, the non-monotonicity follows from the force vs. pitch relationship in Eq. 3.45, which grows quickly, reaches a maximum then decreases again as the pitch angle approaches $\pi/2$. As a result for each n the cytoplasmic concentration exhibits a similar maximum vs. N_0 as force does vs. pitch. This maximum is at larger N_0 for larger n, corresponding to a constant θ^*. We also see in Fig. 4.5 that the fluctuations in the monomeric concentration are very large and approximately independent of n and N_0 — the system is often below the critical concentration despite the upward bias due to the constraint forces. This has implications for force generation, which we discuss in Sec. 4.3.

If the force experienced by the bundle tip does not vary strongly, *i.e.* if, $dF/dx \ll k_BT/a_0^2$, then constraining a filament at both ends does not alter the treadmilling

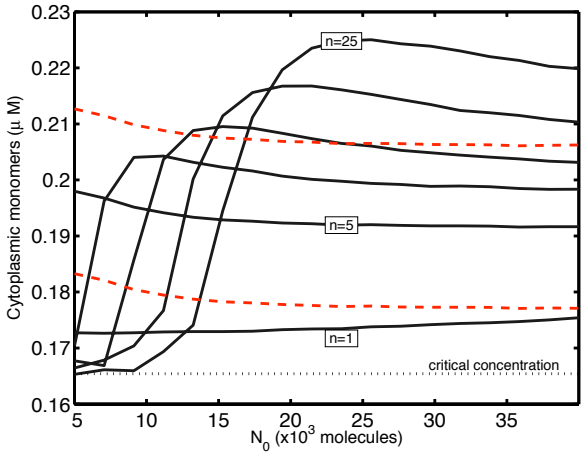

Figure 4.6: Steady-state cytoplasmic concentration c_{ss} of MreB monomers vs. total monomer number N_0 from stochastic simulation for n protofilaments, showing $n = 1$, 5, 10, 15, 20, and 25, using eukaryotic actin kinetics. The dotted line represents the critical concentration. The red dashed line illustrates the large standard deviation of stochastic fluctuations in steady-state, for $n = 5$. These fluctuations are $\approx 0.02\,\mu$M, or roughly 12%, much lower than for *Thermotoga*-scaled kinetics (Fig. 4.5).

rate given in Eq. 2.4, since all on-rates are scaled proportionally, leaving their ratio unchanged. In the other limit, in which a filament is stuck in an infinite square well and forces are zero if the filament is blow a certain length and infinite above it, the treadmilling rate is also unchanged. We derive this surprising results in Appendix A. It is thus not surprising that in the much more complicated situation of a treadmilling bundle, λ_{tread} remains identical.

4.3 Force generation by a stochastic polymer bundle

There is a large disagreement between the steady-state configuration predicted by mean-field approximations and what is found through stochastic simulation, evident in the cytoplasmic concentration in Fig. 4.5 contrasted with Fig. 4.3. In the mean-field approximation, the force obeyed the simple form of Eq. 4.3,

$$F = f_0 \ln\left(\frac{c}{c_c}\right) n_{tip}. \tag{4.11}$$

In our simulation, the emergent force generation is complicated by stochastic effects. We explain this in terms of two competing phenomena; the fluctuations in the structure of the tip, which augments force generation at a given cytoplasmic concentration, and the fluctuations in the concentration of cytoplasmic monomers themselves, which reduces the force generation.

4.3.1 Tip fluctuation effects

In the absence of forces, every protofilament of a bundle treadmills with equivalent rates and critical concentrations. However, force generation by a bundle in which the load is applied only on the most advanced n_{tip} protofilaments behaves differently. In the mean-field approximation we were forced to assume a particular value for n_{tip}, while in the full simulation, the number fluctuated significantly. For instance, for $n = 20$, $N_0 = 20000$, the full distribution of n_{tip} is shown in Fig. 4.7. Nearly 70% of the time, only one protofilament reaches the end of the bundle, and thus only one protofilament is pushing against the cell wall. However, the force generation is very different from the mean-field result in which we assumed $n_{tip} \equiv 1$.

In fact, when n_{tip} is allowed to fluctuate, lagging filament tips grow without force retardation and with a reduced c_c, thereby catching up to the tip more often than otherwise — increasing n_{tip} and reducing the load per loaded filament. This leads to a larger total load for the bundle for the same monomer concentration c_{ss}. A similar effective increase in force generation due to stochastic fluctuations has been noted in passing [62], although not analyzed in detail.

In this section we explicitly work out the details for $n = 2$. For $n > 2$, the effects of force generation by a stochastic n_{tip} are expected to be more significant, as is seen in Fig. 4.9.

Stochastic tip: $n = 2$ case

We parametrize the system of two filaments by $i \in \{0, 1, ...\}$, the number of monomer spacings between the two tips. For any i, two competing Poisson events could increase the spacing: addition at the leading tip and dissociation at the lagging tip. Reduction of i occurs by the complementary two events. The fact that there are two physical

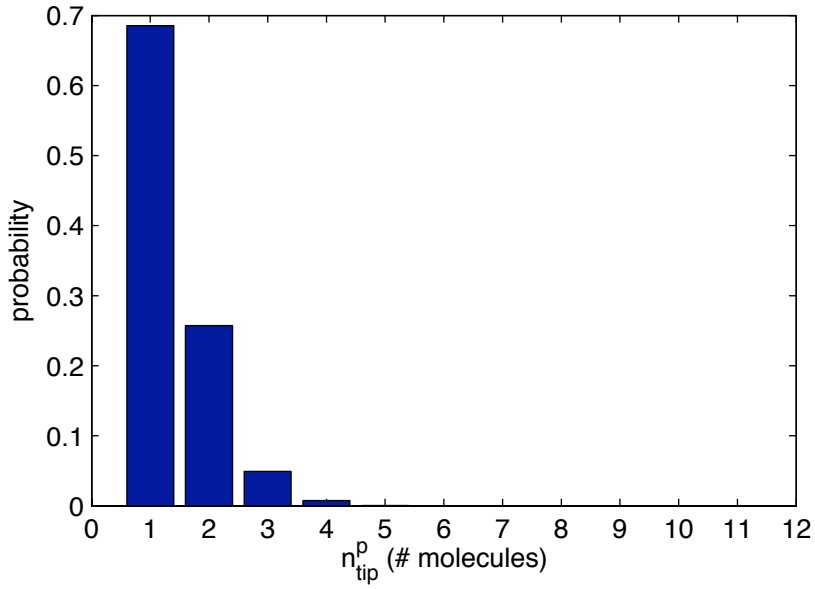

Figure 4.7: Probability distribution of number of protofilaments that reach the end of the bundle, n_{tip}. The data was taken from the final 10^6 s of a stochastic simulation with $n = 20$ and $N_0 = 20000$. As shown in the graph, nearly 70% of the time there is only one protofilament reaching the tip. The distribution has mean $\langle n_{tip} \rangle = 1.38$ and standard deviation 0.62.

configurations corresponding to any particular value of i, except for $i = 0$, is irrelevant. This is a Markov process whose transition diagram is depicted in Fig. 4.8.

The master equations lead to the following equations for stationary probabilities p_i:

$$\begin{aligned}
i \geq 2 \quad &: \quad p_{i-1}(k_{\text{off}} + k_{\text{on}} c\epsilon) + p_{i+1}(k_{\text{on}} c + k_{\text{off}}) = p_i(k_{\text{off}} + k_{\text{on}} c\epsilon + k_{\text{on}} c + k_{\text{off}}), \\
i = 1 \quad &: \quad 2p_0(k_{\text{off}} + k_{\text{on}} c\sqrt{\epsilon}) + p_2(k_{\text{on}} c + k_{\text{off}}) = p_1(2k_{\text{off}} + k_{\text{on}} c(1 + \epsilon)), \\
i = 0 \quad &: \quad 2p_0(k_{\text{off}} + k_{\text{on}} c\sqrt{\epsilon}) = p_1(k_{\text{on}} c + k_{\text{off}}).
\end{aligned}$$

The factors of $\sqrt{\epsilon}$ arise when $i = 0$ and there are two leading tips sharing the load, halving the force per filament. These equations lead to recurrence relations for p_i. Although i cannot exceed the length of the filament, the p_i vanish exponentially as i increases so we approximate $i_{max} = \infty$. Imposing normalization, $\sum p_i = 1$, we find

$$p_0^b = \frac{c(1 - \epsilon)}{c(1 + 2\sqrt{\epsilon} - \epsilon) + 2c^b}, \tag{4.12}$$

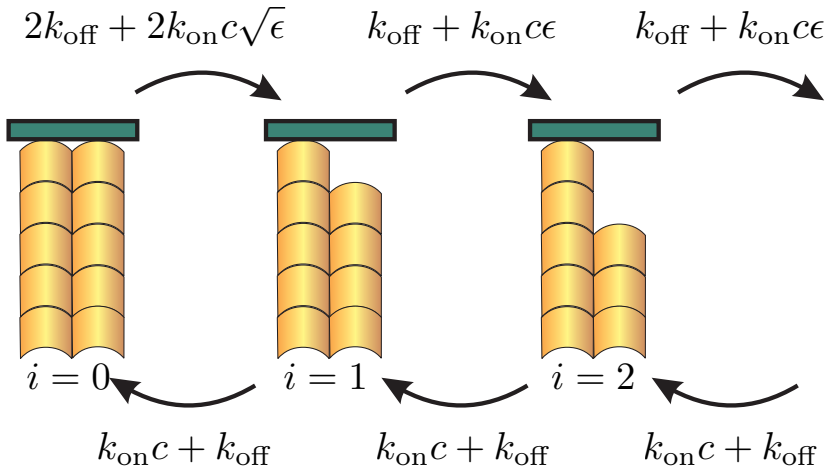

Figure 4.8: Transition diagram for a stochastic polymer tip with $n = 2$ protofilaments as it interacts with a load force, F, represented by the rectangle. The parameter i represents the number of subunit spacings between the leading filament tip (which is always in contact with the load) and the other tip. The force is mediated through a Boltzmann factor, $\epsilon \equiv \exp(-F/f_0)$.

where $c^b \equiv k^b_{\rm off}/k^b_{\rm on}$, and we have specified the barbed end. An equivalent expression for p^p_0 applies for the pointed end. The average polymerization velocity for these stationary probabilities is

$$\begin{aligned} \lambda^b &= (2k^b_{\rm on}c\sqrt{\epsilon})\,p_0 + (k^b_{\rm on}c\epsilon - k^b_{\rm off})(1-p_0) \\ &= (k^b_{\rm on}c\epsilon - k^b_{\rm off}) + (k^b_{\rm on}c(2\sqrt{\epsilon}-\epsilon) + k^b_{\rm off})\,p_0, \end{aligned} \tag{4.13}$$

and is a nontrivial function of both c and F (through ϵ). To solve for the treadmilling concentration at a given force, we insert the barbed and pointed equivalent versions of Eq. 4.13 into $\lambda^p = -\lambda^b$, which is a cubic polynomial in c, and we extract the one real, stable root.

The relation between the total applied force, F_B, and the cytoplasmic monomer concentration c_{ss} is shown by the solid line in Fig. 4.9. Note that this derivation (and the simulations in Fig. 4.9) imposes a static c, though n_{tip} fluctuates. The disagreement with the mean-field result (dashed line), indicates that the n_{tip} fluctuations are

important for the total force.

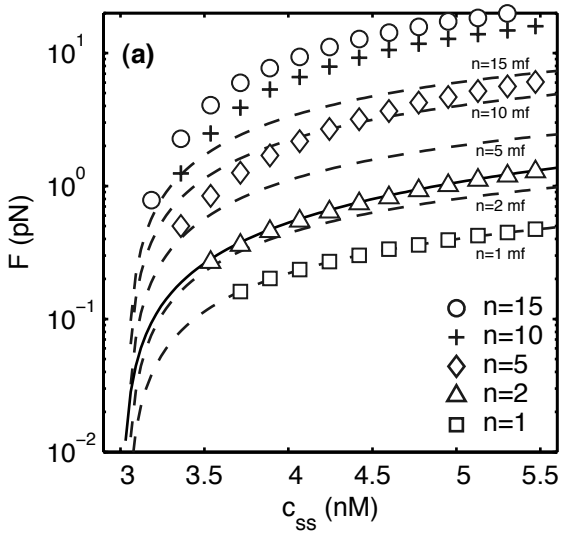

Figure 4.9: The effect of tip fluctuations on force generation by a polymer bundle. Maximal steady-state force generation F by a filament bundle with a stochastic n_{tip} is shown as a function of average concentration c_{ss}. We hold c_{ss} fixed and allow an arbitrary bundle stiffness. The solid line represents the analytic prediction for $n = 2$ with a stochastic n_{tip}. The points indicate stochastic simulations, only allowing n_{tip} to vary. Fluctuations in n_{tip} allow a significantly increased force compared to the mean-field results. Various average bundle thicknesses n are shown. The dashed lines represent the mean-field predicted force-concentration relation (Eqs. 4.3, 4.11) if $n_{tip} = n$ independent tips were all sharing the load.

4.3.2 Cytoplasmic fluctuation effects

The second phenomenon responsible for the disagreement between the mean-field prediction and stochastic simulation is the nature of the cytoplasmic monomers. First, they are discrete; in a typical cell with $R_c = 400\,\text{nm}$ and $L_c = 3\,\mu\text{m}$, one monomer gives a concentration of $1/N_C = 0.87$ nM, so only integer multiples of this concentration are ever achieved, $c \in \{0.87, 1.74, 2.61, ...\}$ nM. The second is their large fluctuations, as mentioned previously and shown in Fig. 4.5. The distribution of the number of cytoplasmic monomers in steady state is shown in Fig. 4.10, for the

particular case $n = 20$ and $N_0 = 20000$. In this case, the average was $N = 4.07$, corresponding to $c = N/N_C = 3.54$ nM, slightly above the critical concentration.

The reason the fluctuations affect the force generating properties is as follows. A linear function of a random variable will have an average value equal to the function evaluated at the average of the random variable. However, if the function is nonlinear and the tails of the random variable's distribution are long enough, this is not expected to hold. In our case, the function is the force-concentration relation shown in Fig. 4.9, which is concave-down. The random variable is the concentration, shown in Fig. 4.10, and is highly asymmetric towards the left (*i.e.* it has positive skewness). In such a situation, the average force is less than the force predicted by the average concentration. The fluctuations of the cytoplasmic monomers thus *decrease* the force-generation at a given average concentration. These effects, in combination with the effects of tip fluctuations described in the previous section, are shown in Fig. 4.11.

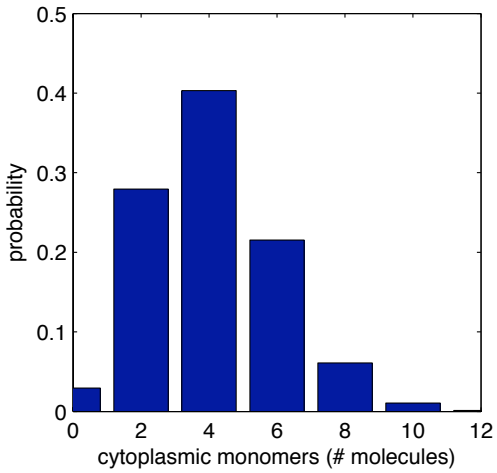

Figure 4.10: Probability distribution of number of cytoplasmic monomers in steady-state, N. The data was taken from the final 10^6 s of a stochastic simulation with $n = 20$ and $N_0 = 20000$. The distribution has mean $\langle N \rangle = 4.07$ and standard deviation 1.97. The long tail is cut off for clarity, although the number of monomers did occasionally reach $N = 16$.

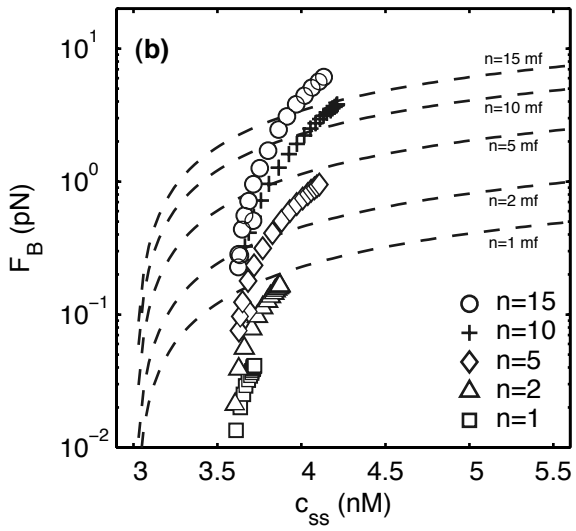

Figure 4.11: The effect of cytoplasmic fluctuations in force generation by a polymer bundle. Maximal steady-state force generation F by a filament bundle with a stochastic n_{tip} is shown as a function of steady-state concentration c_{ss}. Various average bundle thicknesses n are shown. The dashed lines represent the mean-field predicted force-concentration relation (Eqs. 4.3, 4.11) if $n_{tip} = n$ independent tips were all sharing the load. The points indicate fully stochastic simulations. A specific bundle elasticity is imposed by forcing $F = F_B$. Fluctuations in c_{ss} systematically decrease the bundle force compared to Fig. 4.9, and this effect is stronger for smaller c_{ss}.

4.4 Cell growth

As the cell grows, doubling its lateral length before dividing, so must the MreB helix. There are two modes in which this growth may occur: the MreB helix may unstretch, increasing its pitch, or its pitch may remain constant while the filament length increases. It may also be a combination of these two modes. Experimental results are mixed. Some reports observed the helix growing with constant pitch [41], while Mbl has been observed to have longer pitches in longer cells [9, 80]. We address this question here.

We assume that the total number of monomers N_0 is proportional to the cell length and that the number of protofilaments n is length-independent. We simulated

cell growth in a regime towards the low-N_0 end of Fig. 4.4, with $N_0 = 3 \times 10^3 L_c$ so that an average $3\,\mu$m cell contains 9000 MreB monomers, and towards the high-N_0 end, with $N_0 = 10^4 L_c$. Fig. 4.12 shows how the steady-state helical pitch angle varies as the cell length, L_c, ranges between $2 - 4\,\mu$m.

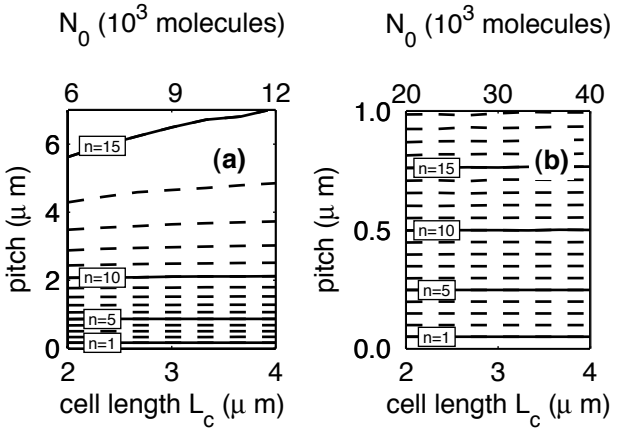

Figure 4.12: Pitch p as the cell length L_c grows for various filament bulk thicknesses n_{bulk} as predicted by stochastic simulation, for (a) $N_0 = 3 \times 10^3 L_c$ so that an average $3\,\mu$m cell contains 9000 MreB monomers, corresponding to regimes towards the low-N_0 end of Fig. 4.4, and (b) $N_0 = 10^4 L_c$, corresponding to the high-N_0 end. For most bundle thicknesses, the pitch is effectively constant as the cell elongates. However, for thicker bundles in the low-N_0 regime, the helical pitch exhibits a significant dependence on cell length, expanding as the cell doubles in size.

For most bundle thicknesses, n, the pitch is nearly constant as the cell elongates. However, for thicker bundles in the low-N_0 regime, the helical pitch increases significantly as the cell doubles in size. This increase is due to fluctuations at small cell lengths, L_c. While it appears strange that at *large* n, the stochastic effects are larger, the pitch is determined by the filament length L_{fil}, which only depends on the maximum protofilament length. While the mean protofilament length fluctuates less with increasing n, the maximum protofilament length is an extremal property of the bundle — and increases with increasing n. At small L_c, the relative fluctuations in the cytoplasmic fraction also increases. For the larger N_0 regime of Fig. 4.12B, the pitches are much smaller, L_{fil} larger, and length fluctuations correspondingly smaller.

In the physiological regimes shown by boxes in Fig. 4.4, pitch should not change

significantly during cell growth if the overall concentration of MreB monomers remains constant. Experimental observations of considerable variability of the number of helical turns per cell within cells of the same strain, size and growth conditions [80] may imply considerable variability of MreB expression or of the cross-sectional number of protofilaments n.

4.5 Dynamics of the subunits

In experiments on *B. subtilis* involving fluorescence recovery after photobleaching (FRAP) of fluorescence-tagged Mbl, four helical turns on one side of the cell's longitudinal axis were bleached while the other half continued to fluoresce. It took approximately 8 minutes for the bleached halves to recover fluorescence at the same level as the unbleached halves [9]. We obtain an upper bound for this time by calculating the average time unbleached parts of the MreB protofilaments take to treadmill into the bleached regions; one half-turn in the polarized model and one quarter-turn in the non-polarized models. Thus, in silico,

$$t_{FRAP} \approx \frac{\pi R_c}{a_0 \sin\theta \lambda_{tread}} = \frac{\pi\sqrt{p^2 + R_c^2}}{a_0 \lambda_{tread}} \tag{4.14}$$

for polarized array structures and half of that for non-polarized array structures. For $p \approx 0.5\,\mu$m this yields between 3 and 6 minutes. The agreement of this timescale with experiment suggest that monomer renewal by exchange with the cytoplasm may not dominate the FRAP recovery time.

Several experiments have applied the MreB-specific small molecule A22 to quickly and reversibly break down the MreB cytoskeleton by blocking polymerization [36, 48]. Cells remain viable after recovery from A22-induced disruption of MreB and reform their helical patterns in less than 1 minute for *C. crescentus* [36]. In *E. coli* MreB-dependent *oriC* localization was recovered in less than one measurement interval (25 minutes) [48]. In the context of our model, recovery from A22-treatment corresponds to re-establishment of the steady-state MreB helix from a pool of cytoplasmic monomers. We simulated our stochastic model from a nucleus of n protofilaments, each of length 3 (as suggested for actin [19]), under the assumption that the nucleation time is short [25]. Thicker bundles (larger n) reach their final steady-state

length much faster than thin bundles, due to the presence of more free filament ends. The equilibration times vary between $1-5$ seconds. Fewer bundled protofilaments took longer to reach a steady state, the longest being $n = 1$, with $N_0 = 10000$, in which the final length is reached in 5 seconds. These are consistent with A22 recovery timescales.

We can also address the timescale of breakdown. Assuming that A22 simply blocks polymerization, but does not change depolymerization dynamics, then it will take $t_1 = L_{fil}/(k^p_{off}+k^b_{off}) \approx 25$ minutes for each protofilament to disassemble with no internal free ends. If each protofilament has length L_{proto} with L_{fil}/L_{proto} free pointed (or barbed) ends, then we would expect the disassembly to be correspondingly faster by $t_m = t_1/m$. Experiments constrain the actual disassembly time in *C. crescentus* [36] to be ≤ 1 min, implying $m \geq 25$ and $L_{proto} \approx 300\,\text{nm}$. Analysis of single-molecule experiments in *C. crescentus* estimates $L_{proto} \approx 392 \pm 23\,\text{nm}$ [44] by assuming that protofilaments treadmill in place. If protofilaments also advect along the bulk MreB cable, as we assume in our model, this estimate would be lower.

These estimates of assembly and disassembly timescales of the MreB helix can also be applied to the reported midcell condensation of MreB in *E. coli* [76] and *C. crescentus* [29], and of MreBH in *B. subtilis* [81]. Two possible mechanisms are an elastic compression of the intact MreB helix to midcell driven by some (posited) motor protein, or disassociation of the MreB helix and (transient) association with some midcell binding partners. These mechanisms may occur in tandem. The timescales of condensation and recovery are ≈ 30 minutes in *C. crescentus* which is considerably longer than A22-induced breakdown. The maximum filament-end force needed to compress a typical MreB helix in our model from L_c to a midcell spiral is $F_B^{\max} \approx 10pN$, and is comparable to the force generated by the RNA polymerase [48] and the anchoring forces of integral membrane proteins [26]. Thus, both motor driven compression and depolymerization are possible mechanisms for the observed midcell condensation.

4.6 Macromolecule trafficking

A vital role of MreB is the polar localization of proteins such as Tar in *E. coli* [75], the cell polarity markers DivJ and PleC in *C. crescentus* [35], and the origin-proximal region of the newly-replicated chromosome in *E. coli*, *B. subtilis* and *C. crescentus* [48]. One possibility is that these passengers associate with yet-to-be-discovered motor proteins that use MreB as a track to the poles [75]. A second possibility is that these proteins simply bind to the helix and advect with the continuous treadmilling, eventually ending up at one of the polar tips. A third possibility is that they associate with leading tips of MreB protofilaments [28], perhaps via intermediary proteins analogous to formin for actin filaments. Here we quantitatively analyze these possibilities, which are depicted in Fig. 4.13, together with associated translocation speeds with respect to the fixed bacterial axis.

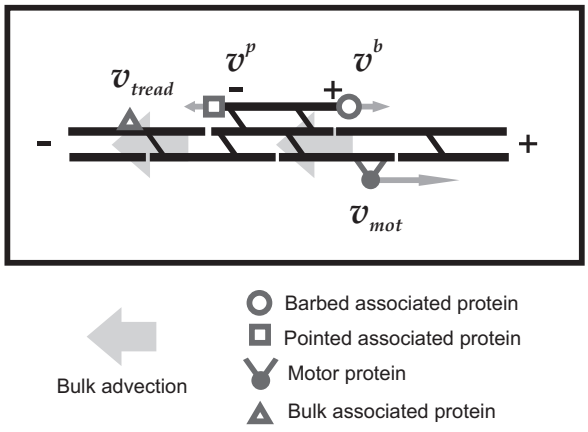

Figure 4.13: Schematic of the different possible modes of transport along MreB bundles. Velocities are absolute with respect to the cell in the indicated directions. Bulk treadmilling advects bundles that span the cell length at a speed v_{tread} towards the slow-growing pointed ("−") end. Side associated protofilaments, without constraint forces at their tips, have different polymerization rates and so are not simply advected with the bundle. Their tip velocities are v_p and v_b for pointed and barbed ends, respectively. As discussed in the text, v_b is always opposite the treadmilling direction. Putative motor proteins would probably be polarized and would have a characteristic speed v_{mot}. The figure illustrates one polarized protofilament bundle, however it is possible that two oppositely polarized bundles would exist within a cell — in which case the polarity and velocities of the second bundle should be opposite the first.

For any transport mechanism, a characteristic speed along the filament bundle, v_{trans}, translates into a speed $v_z = \cos\theta v_{trans}$ relative to the cell's axis. Assuming the protein initially binds at a uniformly random location along the bundle, the average time to reach a pole is then

$$\langle t_{trans} \rangle \approx \frac{L_c}{2v_z} = \frac{L_c}{2\cos\theta v_{trans}}. \tag{4.15}$$

This time can be compared to the cell division time to see whether it provides a plausible mechanism for polar localization over many generations.

The myosins that transport organelles along actin tracks in eukaryotes travel at speed $v_{mot} \approx 200-400\,\mathrm{nm/\,s}$ [71] (though speeds of up to $10^4\,\mathrm{nm/\,s}$ have been reported [64]). Attached to putative homologues of such myosins, macromolecules could be translocated to the poles in $\sim$ 20 seconds. This is well within cell division times, so this would be a viable polarization mechanism. However, no cytoplasmic motor homologue has been identified in prokaryotic cells. Furthermore, almost all myosins travel towards the pointed ("+") tip along actin filaments [90], so a single polarized MreB bundle would probably only support motor-driven localization to one pole while unpolarized bundles would not support selective targeting to one pole and not the other.

Static association of proteins to the side of MreB bundles would, through treadmilling, lead to a translocation speed equal to the rate of advection times the monomer spacing, $\lambda_{tread} a_0$, in the direction of the pointed end of the bundle. In steady state, the advection rate $\lambda_{tread} = 1.2\,\mathrm{s}^{-1}$ is independent of the buckling force, the bundle thickness, or the cytoplasmic concentration and leads to $v_{tread} = a_0\lambda_{tread} = 5.92nm/s$, shown by the dashed line in Fig. 4.14C. Applying Eq. 4.15 to a typical configuration with $p = 1\,\mu\mathrm{m}$ and $L_c = 3\,\mu\mathrm{m}$, this yields $\langle t_{trans} \rangle \approx 12$ minutes, which is plausible compared to cell-division timescales.

Proteins that could bind either directly, or via putative tip-binding proteins (analogous to formin in eukaryotes [28, 46]) to the barbed end of free protofilaments could be translocated in the *opposite* direction to the treadmilling advection. In an unbuckled ($F_B = 0$) filament, lateral protofilaments treadmill at the same rate of the net backwards advection of the bundle, accomplishing no net movement relative to the cell's axis. In a buckled filament, however, the monomer concentration is considerably

above the critical concentration of a free protofilament, as illustrated in Fig. 4.5. As a result, unconstrained laterally associated barbed ends grow faster than the bulk of the bundle, with

$$\begin{aligned} v_b &= a_0 \left[(k^b_{\rm on} c_{ss} - k^b_{\rm off}) - \lambda_{tread} \right] \\ &= a_0 k^b_{\rm on} (c_{ss} - c_c). \end{aligned} \tag{4.16}$$

For each bundle thickness and pitch simulated, the translocation times are shown in Fig. 4.14A and speeds in Fig. 4.14C. Typical bundles with $20000 - 40000$ molecules of MreB and $8-15$ protofilaments thick would transport passengers in $4-6$ minutes, considerably faster than laterally-associated proteins and in the opposite direction.

Similarly, proteins associated with the slow-growing pointed end have a net velocity given by

$$\begin{aligned} v_p &= a_0 \left[(k^p_{\rm on} c_{ss} - k^p_{\rm off}) + \lambda_{tread} \right] \\ &= a_0 k^p_{\rm on} (c_{ss} - c_c). \end{aligned} \tag{4.17}$$

Note that free pointed ends are *disassembling* on average, though not as rapidly as the treadmilling, so that $v_p < v_{tread}$. These translocation times are shown in Fig. 4.14B and speeds in Fig. 4.14D. According to Eqs. 4.16 and 4.17, they are slower by a factor of $k^b_{\rm on}/k^p_{\rm on} \approx 10$ compared to free barbed ends, taking several hours. These times are probably too slow to be biologically relevant.

These protofilament-associated translocation modes offer a non-motor based mechanism for specific targeting of proteins to *either* pole in cells with a single polarized bundle of MreB. The cell could specify the specific pole destination of a particular protein by specifying which part of an MreB protofilament it binds to: barbed-associated proteins would end up at the pole at the barbed-tip of the MreB bundle with a speed of v_b, while laterally-associated proteins would end up at the pointed-tip pole with speed $v_{tread} = a_0 \lambda_{tread}$. Of course, these translocation mechanisms may also supplement a (hitherto undiscovered) motor-based mechanism to provide targeting to either pole with polarized MreB bundles. We do not see any way of specific targeting of proteins to a given pole if the MreB bundle is not polarized or if there are anti-parallel bundles, either with or without motor proteins.

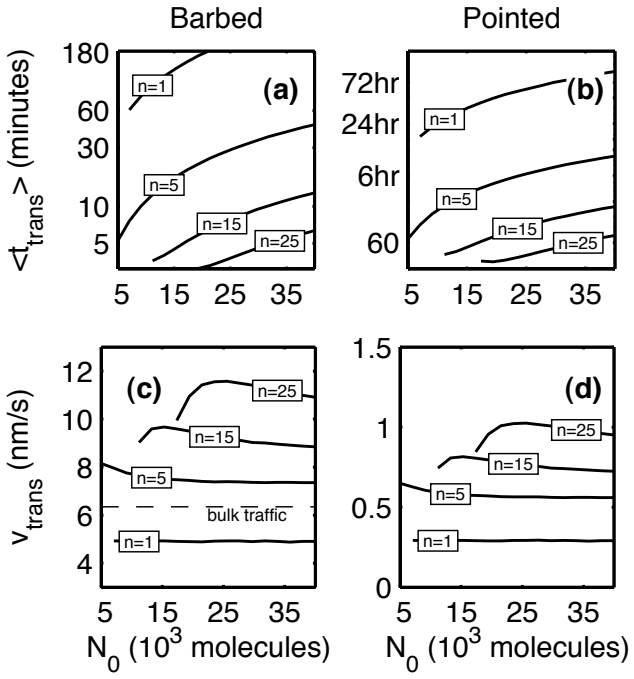

Figure 4.14: Mean translocation times $\langle t_{trans} \rangle$ for macromolecule passengers being transported by MreB side protofilaments treadmilling on the side of the main cables. Constraint forces at the ends of the helix keep c_{ss} above c_c, so that significant axial movement can be seen with respect to bulk treadmilling. Different modes of transport along the cables are depicted schematically in Fig. 4.13. Barbed ends move antiparallel with respect to bulk advection (a,c). Pointed ends move in the same direction as bulk advection, however the slower polymerization rates lead to much longer translocation times (b,d). Lateral traffic associated with parts of the bulk cables move towards the pointed end at $a_0\lambda_{tread}$, indicated in c) by the dashed line. Any passenger dissociation and re-association from protofilament tips will increase translocation times and decrease effective speeds.

If protofilaments dissociate at a significant rate from the main bundles then these translocation times represent lower bounds. Additionally, any putative MreB-binding proteins could strongly affect the polymerization kinetics. For example, ADF/cofilin in eukaryotes increase k^p_{off} for actin by ~ 20 times. A bacterial homologue of such a protein would decrease the delivery time of pointed-associated proteins by ~ 20. Similarly, in the presence of profilin, formin increases the barbed growth rate of actin by 10- to 15-fold [31], and would decrease the delivery time of barbed-associated proteins to within a minute, which is comparable to times for motor proteins.

Proteins associated with pointed or barbed ends of protofilaments could be translocated towards those poles at v_p and v_b, respectively. However the proteins could also be directly recruited to distinct poles of the cell, due to the free ends of the MreB bundles. The relative magnitude of translocation vs. direct recruitment is dependent on the number of barbed or pointed protofilament ends. Tip-associated translocation requires a significant number of laterally associated protofilaments tips to maximize the translocation flux, while tip-directed polar recruitment requires unbroken protofilaments to minimize non-polar binding sites. Observations in *C. crescentus* [44] indicate that protofilaments are short, supporting tip-associated translocation as a viable mechanism in vivo.

4.7 Implications and conclusions

The model introduced in Chapter 3 leads naturally to steady-state helical configurations described by four quantities: the helical pitch, the concentration of free monomers, the total abundance of MreB and the bundle thickness. The main result of this chapter is a relationship between these, both approximate analytic expressions (Eqs. 4.10, 4.9.) and through stochastic simulation (Figs. 4.4, 4.5). Given any two of these quantities, our model predicts the other two.

This is relevant for two reasons. The first is practical. Two of the parameters can be measured experimentally, pitch through fluorescence tagging and microscopy [9,17,49] and total abundance through quantitative immunobloting [41,50]. The other two have been considerably more difficult to measure: the cytoskeletal protein FtsZ has been studied for many more years (Sec. 2.3.2) yet its bundle thickness remains entirely unmeasured. Measuring the in vivo amount of MreB not associated with the bundle has also never been achieved. Our model thus allows two measurable properties to predict two properties that would be hard to measure directly.

The second reason is theoretical. The steady-state predicted by our model provides an immediate foundation upon which to address other properties of the bacterial cytoskeleton. One example in the previous chapter is that of macromolecular trafficking. The steady-state configuration gave rise to several obvious methods for transporting

packages to the poles. The timescales estimated from our *Thermotoga*-scaled parameters allowed us to reject one of these modes (association with free pointed ends), and propose a method for pole discrimination that could lead to the assymmetry of *C. crescentus* (association with free barbed ends, along with association with the stable bulk of the bundle). In the event that our model is modified, either in the parameters or in fundamental details, it is likely that similar relationships between the configuration parameters can be derived.

A significant part of this chapter was concerned with the effects of stochasticity in the small, noisy environment of a bacterial cell. This lead to the surprising result that a bundle of polymerizing protofilaments can generate more force than if all n tips were constantly pushing the load. The role of stochastic fluctuations in biological systems has been recently stressed [55,69]. The behavior of the tip of a growing, force-generating bundle of polymers that we analyzed here provides another example of the importance of such stochasticity in biology.

Chapter 5

Results: Elastic consequences

The previous two chapters beg the following question: What mechanical forces cause the MreB filament to take on a helical configuration? The separation of timescales described in Eq 4.1 and 4.2 allowed us to address the polymerization dynamics separately from this question. Now we explore how the filament responds to its internal elastic forces and external constraints.

We have developed a finite element method to simulate the behavior of MreB inside a small bacterial cell. We first numerically verify the conclusions of Sec. 3.2.2, that a filament with length larger than the cell length will not simply buckle into a helix. We also verify the timescale calculation of Eq. 4.1. Then, three models are proposed for possible external forces, each increasing in complexity and physiological relevance.

5.1 Elastic dynamics simulator

In order to explore the elastic behavior of an MreB filament inside a cell in any non-trivial situation, numerical simulation is required. Moreover, the simulation must operate in a particular regime:

- The low Reynolds number environment of the cytoplasm. The Reynolds number is a dimensionless quantity describing the viscous nature of a fluid, defined as $Re \equiv vl/\eta$ where v is the characteristic velocity, l is the characteristic length scale, and η is the viscosity. If $Re \ll 1$, we are in the viscous limit, and instead of Newtonian dynamics ($\Sigma F = ma$), we have $\Sigma F \propto v/(l\eta)$. Inertia (mass) plays no role [51]. In the cytoplasm, $Re \approx 10^{-7}$ and we are certainly in the viscous limit.

- The filament is semiflexible, meaning it is much shorter than its persistence

length (*i.e.* $L_{fil} \ll \xi_p$), but longer than its radius of curvature (which is maximally the radius of the cell, R_c). It is also nearly inextensible: the energy density for stretching is of order $EA = 20\,\mathrm{pN}$, while for bending it is $B/R_c^2 = 6 \times 10^{-2}\,\mathrm{pN}$.

- The simulation must preserve the symmetry inherent in the situation. This symmetry cannot be imposed, since we wish to explore asymmetric situations and situations in which symmetry is spontaneously broken.

- The filament is subject to external boundary conditions, both mechanical, where the external forces are specified, and kinematic, where a constraint is placed on the configuration, such as confining it within or on a cell wall. It is also subject to large displacements, where parts of the filament may be rotated by 90° and displaced by several microns, precluding perturbative methods.

Several methods are available for simulating elastic rods. Simple ball-and-spring models have been used [92], however they require very small discretization for accuracy, especially since the curvature driving bending dynamics is proportional to a second spatial derivative (Eq. 3.21). Finite element methods have been developed for elastic rods [7], although not for large deflections or in the viscous limit. For the particular case of filaments in bacteria, statistical mechanical methods such as the Metropolis algorithm have been used to find energy minima [2], however this leaves the dynamics unaddressed. The intrinsic difficulty in the problem has even prompted the construction of "physical models" made of polyurethane and metal [91] to simulate the behavior of biofilaments in bacteria.

We chose to develop a simulator based on finite element methods, in which the filament is discretized into n_{el} elements of length l^e, and each of their dynamics evolves according to

$$\partial_t x_i = -\rho_i \frac{\partial \mathcal{H}}{\partial x_i} \tag{5.1}$$

where x_i is a coordinate, ρ_i is an associated mobility (roughly an inverse viscosity), and $\mathcal{H}$ is the elastic Hamiltonian given in Eq. 3.14. The details of the algorithm and its implementation are described in Appendix B. To our knowledge, this is the first finite element analysis of the dynamics of a filament in the viscous limit that

includes flexure, torsion and stretching. The numerical timestep is restricted by the microscopic elastic timescale (distinct from the macroscopic timescale in Eq. 4.1), which is set by an eigenvalue of a matrix involved in the finite element analysis, Eq. B.15, and is $\Delta t \approx 10^{-6}\,\mathrm{s}$.

5.2 A filament inside a cell

We are now in a position to simulate the behavior of a $10\,\mu\mathrm{m}$ filament inside a bacterial cell. For these simulations, we assumed the filament was $n = 5$ protofilament thick, the lower bound suggested by our results in Chapter 4 (Fig. 4.4). This gives bending and stretching modulii $B = B_0 n^2 = 2.5 \times 10^5\,\mathrm{pN\,nm^2}$, $EA = EA_0 n = 10^2\,\mathrm{pN}$ and a bundle diameter of $\sqrt{5}a_0 \approx 11\,\mathrm{nm}$, where the subscripts indicate the modulii of an individual polymer.

We do this with four boundary conditions. For each we simulated from five initial conditions: straight and compressed on the lateral wall, a perfect helix with $\theta = \arctan(L_c/L_{fil}) = 1.26$ rads, a ring at midcell, a ring at one pole, and the main diagonal of the cylinder.

- Hemispherical endcaps, free inside cell

  Starting from a compressed, straight filament along the main diagonal — the longest straight line in the cylindrical portion — the filament quickly buckles into an asymmetric configuration and, by $t = 0.5\,\mathrm{s}$, has relaxed into an equilibrium configuration resembling a figure-of-eight. Two snapshots are shown in Fig. 5.3. In Fig. 5.2, we show the elastic energy of the filament. The initial energy is $1.5 \times 10^4\,\mathrm{pN\,nm}$ (all due to compression), while the final equilibrium energy is $4035\,\mathrm{pN\,nm}$, which is lower than the maximal ellipse ($5000\,\mathrm{pN\,nm}$ from Eq. 3.41), and still lower than for a helix ($7100\,\mathrm{pN\,nm}$ from Eq. 3.32). It equilibrates within $0.2\,\mathrm{s}$, in agreement with the timescale estimated from Eq. 4.1, of $t_{elsatic} \approx 0.47\,\mathrm{s}$. The energy is monotonically decreasing, however not smoothly so: sudden drops in energy occur when kinks snap themselves out, in between slower relaxation dynamics.

- Flat endcaps, free inside cell

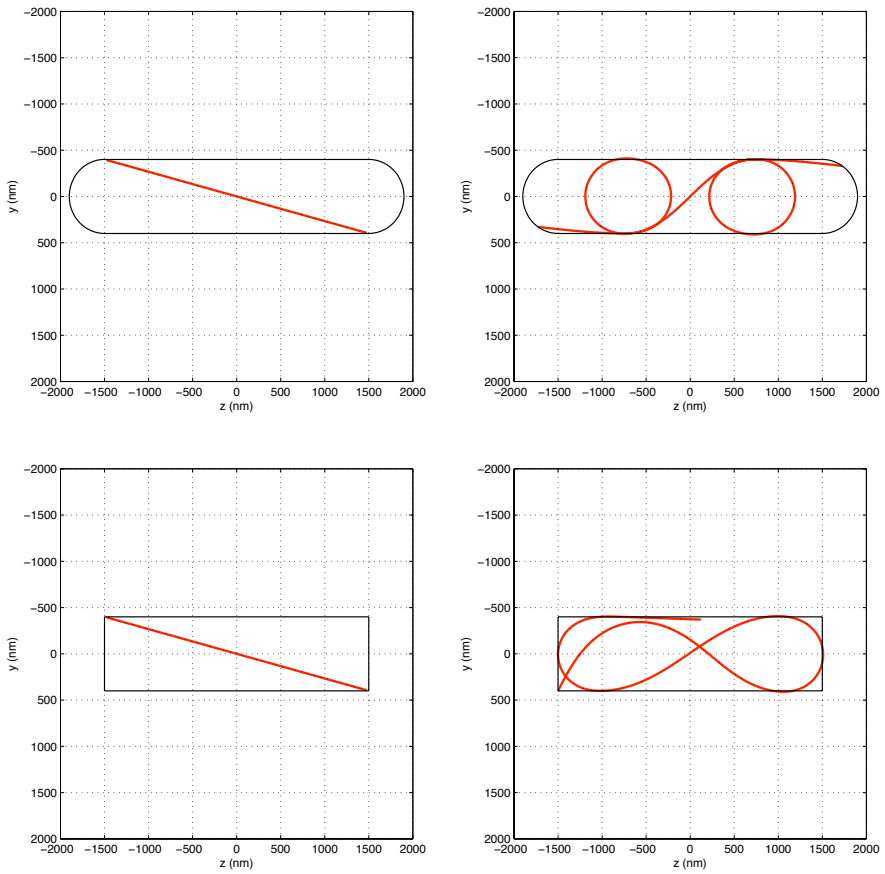

Figure 5.1: The elastic dynamics of a filament free inside a cell. (Top) the initial and equilibrium configurations of a filament inside a cylindrical cell with hemispherical endcaps. The final configuration at $t = 0.5\,\mathrm{s}$ is shown. From Fig. 5.2, the configuration has equilibrated. (Bottom) A filament constrained to stay within a right cylinder with flat endcaps. As for the previous simulation, the final configuration at $t = 0.5\,\mathrm{s}$ is in equilibrium.

Fig. 5.3 shows the same simulation as above, except that the filament is allowed forbidden from entering the hemispherical poles. Again, the filament buckles and assumes an extended configuration that is non-helical.

- Hemispherical endcaps, membrane affinity

  While MreB itself is not an inner-membrane protein, it is always found just below the membrane [15,86]. This may be for geometric reasons (the most relaxed configurations all involve the filament pushing outward against the membrane),

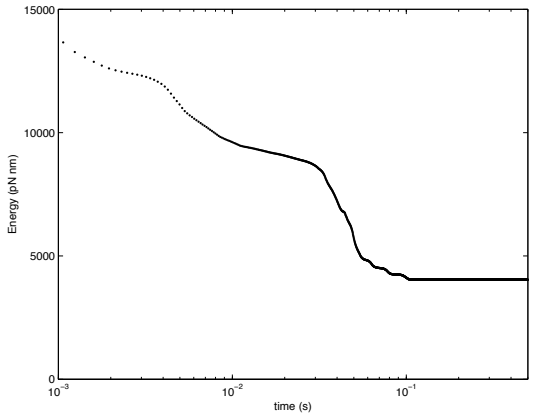

Figure 5.2: The elastic energy of a 10 μm filament inside a cylindrical cell with hemispherical endcaps, allowed to move freely within the cell.

or it may be due to an affinity for the membrane, for instance through the peptidoglycan synthesizing machinery (Sec. 2.2.1). Such an affinity could constrain the filament to the cell wall. For the remainder of the chapter, we explore the consequences of this assumption.

If the filament is constrained to the membrane but allowed in the membrane, it will assume the paperclip configuration depicted in Fig. 3.4B. As predicted, the equilibrium energy is 3000 pN nm, and the configuration is very much non-helical. It is shown in Fig. 5.3.

- Flat endcaps, membrane affinity

  Surprisingly, if the filament is initially configured as a (perfect) helix, it equilibrates into a nearly-helical configuration. Fig. 5.3 shows three snapshots as the filament equilibrates. The filament tips are located initially in the cusp between the flat caps and the cylindrical cell, and would have to overcome an energy barrier to escape. For this reason, the near-helical configuration is in equilibrium.

Only one of these boundary conditions and initial conditions produced a helix-like configuration similar to what is observed experimentally. For this boundary condition, there must be a strong affinity for the membrane and a mechanism to exclude the

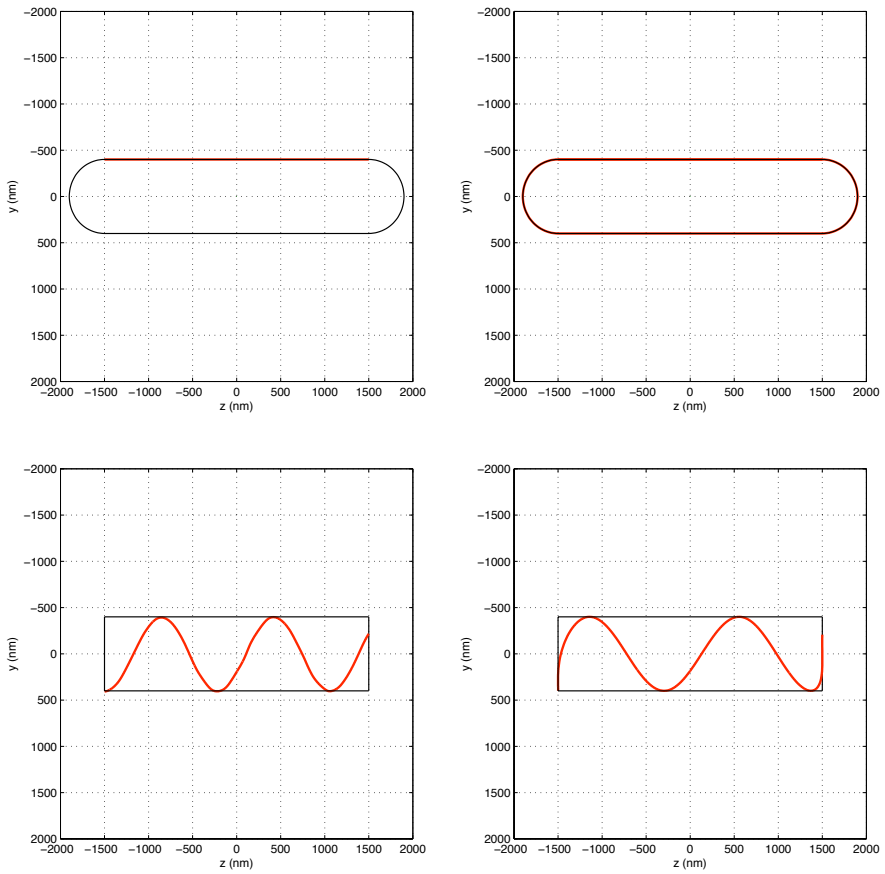

Figure 5.3: The elastic dynamics of a filament constrained to the membrane of a cell. (Top) the initial and equilibrium configurations of a filament inside a cylindrical cell with hemispherical endcaps. (Bottom) A filament constrained to stay within a right cylinder with flat endcaps. As for the previous simulation, the final configuration at $t = 0.5\,\mathrm{s}$ is in equilibrium.

filament from the poles. For most boundary conditions, the filament buckles into different shapes: as stated in Chapter 3, there must be some external forces that cause a torque in the axial direction to create the helical configuration.

5.3 Static external forces

The simplest possible forces giving rise to an axial torque are forces acting in the azimuthal direction, parallel to the surface of the cylindrical portion of the cell wall,

$$\hat{\phi} \equiv \frac{-y\hat{x} + x\hat{y}}{x^2 + y^2}. \tag{5.2}$$

as shown in Fig. 3.3. There is an abundance of examples of molecular motors in both eukaryotes and prokaryotes. Kinesin on microtubules can generate a force between $4 - 8\,\mathrm{pN}$, and myosin on actin can produce $1 - 10\,\mathrm{pN}$ [39]. The RNA polymerase is stronger than both of these, generating a force up to $\sim 25\,\mathrm{pN}$ [48]. Moreover, the RNA polymerase interacts with MreB (Sec. 2.2.4). Another possibility is a force is due to the cell wall synthesis machinery that putatively associates with the MreB helix (Sec. 2.2.1). This molecular complex may rotate around the circumference of the lateral walls as it inserts new peptidoglycan, pulling azimuthally on the MreB helix.

We exposed a $L_{fil} = 3\,\mu\mathrm{m}$ filament, constrained to lie on the membrane of a $L_c = 3\,\mu\mathrm{m}$ cell, to forces at its endpoints, $\vec{F}^{\mathrm{ext}} = \pm 3\,\mathrm{pN}\hat{\phi}$. The result, shown in Fig. 5.4A, appears nearly helical. For closer inspection we define the instantaneous pitch, analogous to the helical pitch (Eq. 3.46)

$$p(s) \equiv \frac{2\pi R_c}{\tan\theta(s)}, \tag{5.3}$$

shown in Fig. 5.5, we see that the configuration is not precisely helical, since the pitch varies significantly over the filament. It is, however, always of the same sign. We refer to configurations of a filament as *helix-like* if it is everywhere on the membrane and if the instantaneous pitch is always the same sign. A configuration with nearly-constant instantaneous pitch is nearly helical.

For the cell to arrange forces to oppose one another, as in the above model, long-range coordination would be required. A more likely biological boundary condition is that the *active* azimuthal force is at one end of the filament, while the other end is anchored in place. The anchor point would be expected to produce a constraining force equal and opposite to the force at the other end, and by intuition, the configuration should be the same as in Fig. 5.4A. We simulated this situation, and indeed, found this result, shown in Fig. 5.4B.

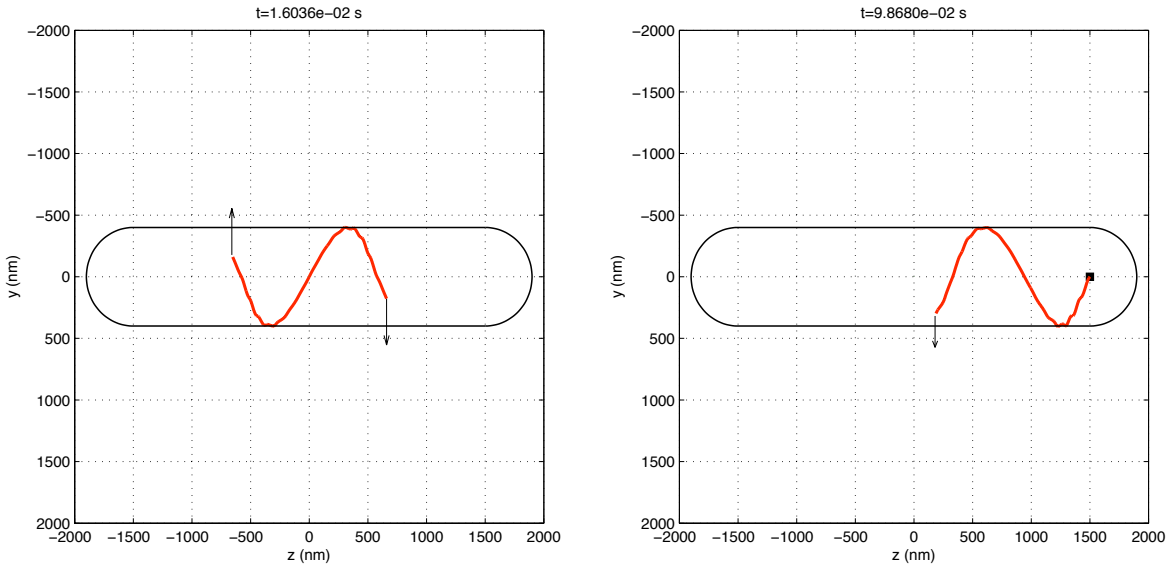

Figure 5.4: Equilibrium configuration of a 3 μm filament on the membrane of a bacterial cell subject to azimuthal forces $\vec{F}^{\text{ext}} = \pm 3\,\text{pN}\hat{\phi}$ (A) at each end, and (B) at one end only, with the other end anchored to remain stationary.

5.3.1 Numerical test: varying element size

To test the accuracy of the code, we repeated the azimuthal force simulation while varying the element length l^e, effectively changing the spatial and temporal discretization. The results are compared for 3 different values of l^e in Fig. 5.5B. The steady-state configurations are convergent, and are qualitatively similar. The maximum discrepancy between $n_{el} = 16$ elements and $n_{el} = 64$ elements is 8%. We use 16 elements (so that one element has length $l^e = 187.5\,\text{nm}$) for our simulations. Although we are clearly not yet in the "continuum limit", this gives an acceptable compromise between accuracy and computational efficiency.

5.3.2 Azimuthal force and steady-state pitch

We obtain a relationship between the magnitude of the azimuthal force, F^{ext}, and the pitch in the resulting steady state. This pitch is not homogeneous along the filament, and we plot the mean, minimum, and maximum for several values of F^{ext}, in Fig. 5.6. As expected, the helix tightens as the force is increased. Pitches within

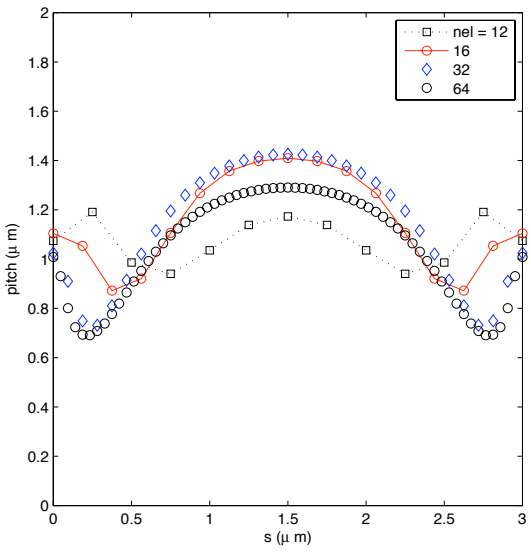

Figure 5.5: Instantaneous pitch in equilibrium configuration of a $3\,\mu$m filament on the membrane of a bacterial cell subject to azimuthal forces $\vec{F}^{\text{ext}} = \pm 3\,\text{pN}\hat{\phi}$ at each end. This is shown for varying numbers of elements. The maximum discrepancy between $n_{el} = 16$ elements and $n_{el} = 64$ elements is 8%.

the reported experimental ranges, $0.4 - 2.0\,\mu$m [41, 44], can be achieved by forces of $5 - 20\,$pN, a range that can be generated by motor proteins.

To explore the dependence on filament length, we simulated the same external force of $F^{\text{ext}} = 6\,\text{pN}$, acting on filaments of lengths $L_{fil} \in [3, 6, 8, 12]\,\mu$m. This is shown in Fig. 5.6. The instantaneous pitch did not qualitatively change, although its magnitude is slightly dependent on filament length.

5.4 Dynamic external forces

The second model of physiological torques we explored has only one end of the filament experiencing an azimuthal force, while the other end is free. In the absence of viscosity, this would lead to a ring-like configuration in steady-state, since nothing is opposing the force. However, in the viscous environment of the cell, the filament will experience a drag force. This drag is a complex function of the configuration of the cylinder — a filament parallel to the z-axis being dragged around the cylinder clearly experience

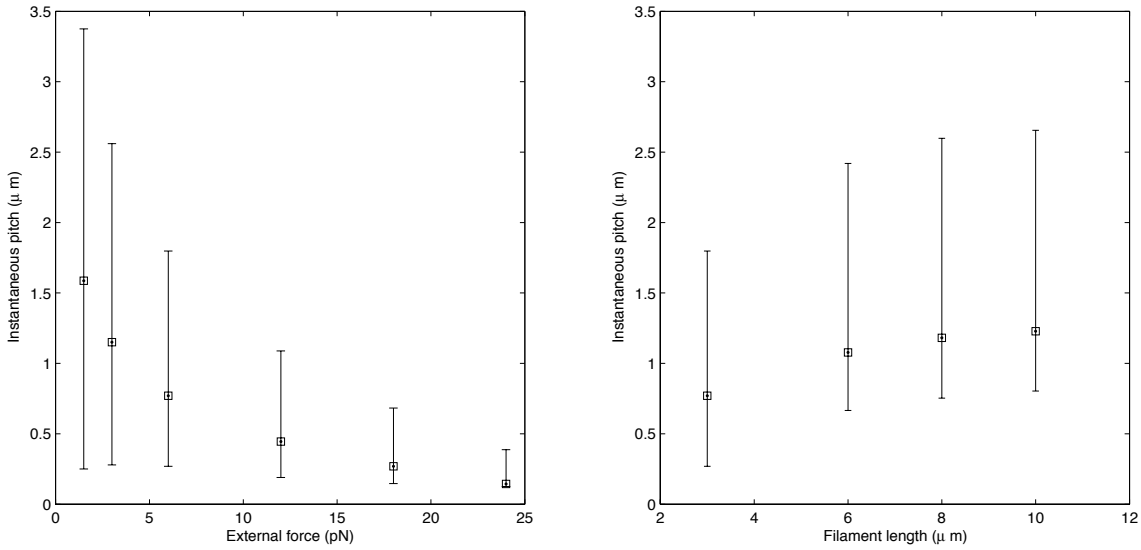

Figure 5.6: (Left) Instantaneous pitch in equilibrium configuration of a $3\,\mu$m filament on the membrane of a bacterial cell subject to azimuthal forces $\vec{F}^{\text{ext}}$ at each end. The instantaneous pitch varies along the filament: the square indicates the averages, and the vertical bars indicate the minima and maxima. (Right) Same, for fixed $F^{\text{ext}} = 6\,\text{pN}$, and varying L_{fil}. There is a weak dependence on filament length.

more drag than one that is in a ring around the z-axis.

The results for $F^{\text{ext}} = 3\,\text{pN}$ are shown in Fig. 5.7. Unlike in the static case, the configuration is not symmetric, however it is still helix-like. The pitch is tightest near the point of application of the force, and increases further out as the energy from the motor dissipates. Corresponding results for varying F^{ext} are shown in Fig. 5.8. The pitches are much longer than in the previous model due to the longer tail of higher pitches away from the force.

The filament continually rotates around the membrane. This occurs because the torque has no opposing force with which to cancel. In Fig. 5.8B we show the angular velocity in steady-state. The relationship appears slightly concave down, but nearly linear in this regime. The inverse slope corresponds to an angular viscosity, defined by μ in

$$\hat{F}^{\text{ext}} \cdot \hat{\phi} = \mu\omega. \tag{5.4}$$

where $\omega = \partial_t \phi$ is the angular velocity. For the dynamic force model, $\mu = 3.55 \times$

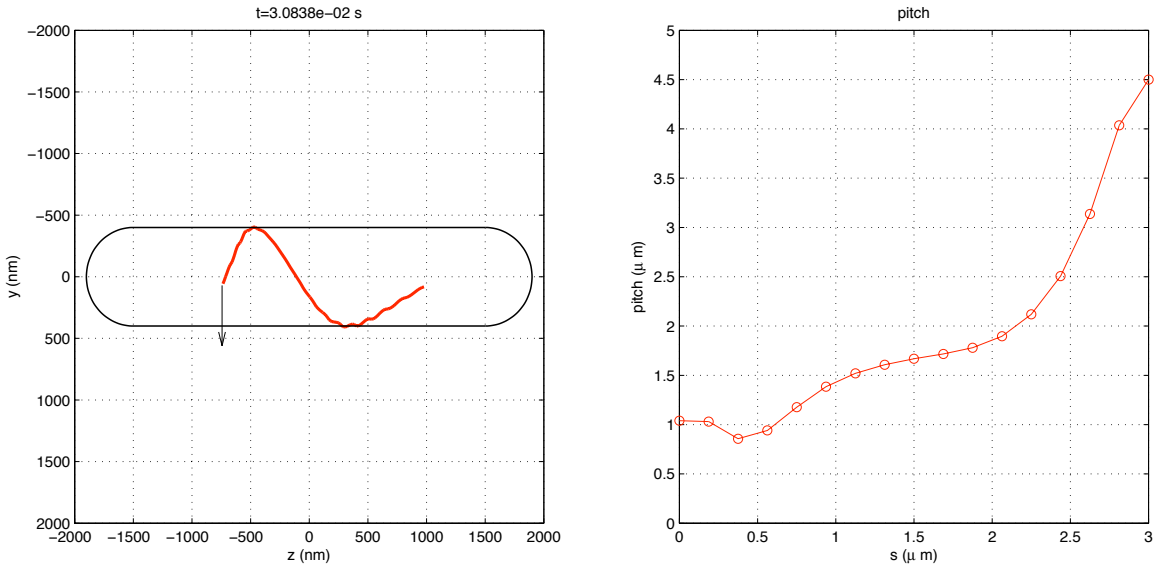

Figure 5.7: Equilibrium configuration (left) and instantaneous pitch (right) of a $3\,\mu$m filament on the membrane of a bacterial cell subject to azimuthal forces $\vec{F}^{\text{ext}} = 3\,\text{pN}\hat{\phi}$ at the left end.

$10^{-3}\,\text{pN}\,\text{s/rad}$.

5.5 Distributed dynamic external forces

The next level of detail we considered was the distribution of forces. It is more likely that the molecular motors are not localized at one part of the filament, but rather appear in some distribution along its length. If they are homogeneously distributed, the filament will not twist into a helix-like configuration. The polymerization dynamics we explored in Chapter 4 lead naturally to an inhomogeneous distribution: Consider a polarized bundle in which most of the subunits being exchanged with the cytoplasm are at the tips. If the molecular motors bind to the filament at a constant rate, they will appear in greater density on subunits that have been incorporated in the filament longest. Since treadmilling means the subunits are constantly advecting towards one pole, the motors will appear with high density at the old (pointed) end, with zero density at the new (barbed) end, and the density will vary linearly in between.

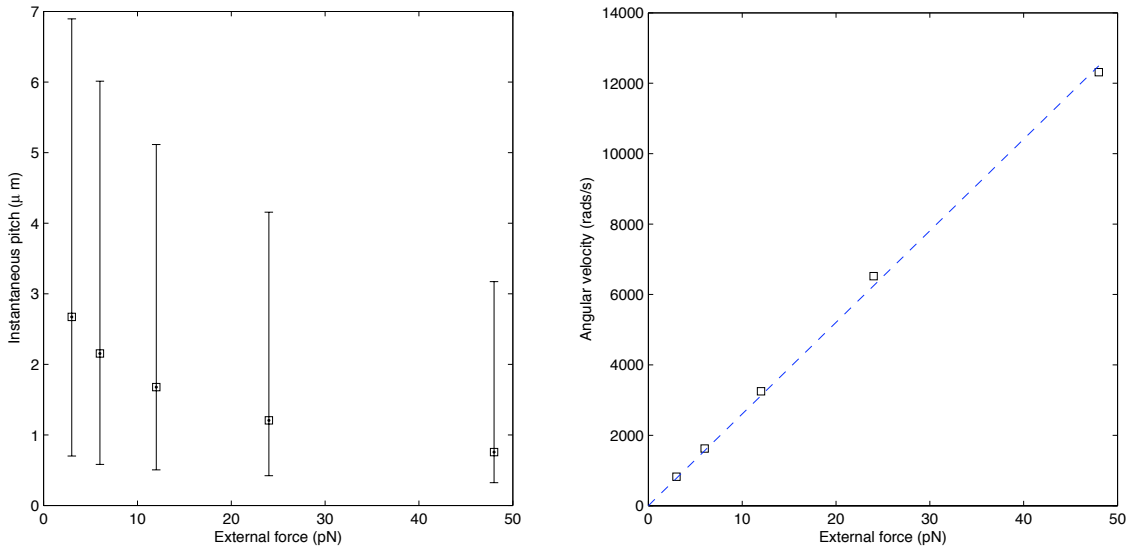

Figure 5.8: (Left) Instantaneous pitch of the steady-state configuration of a $3\,\mu$m filament on the membrane of a bacterial cell subject to one azimuthal forces $\vec{F}^{\text{ext}}$ at its left end. The square indicated the averages, and the vertical bars indicate the minima and maxima. (Right) Angular velocity of in the resulting steady-state. The relationship appears nearly linear — the dotted line shows a linear regression with inverse slope $\mu = 3.55 \times 10^{-3}\,\text{pN}\,\text{s/rad}$.

In this model, the force line density, in pN/ nm, is

$$\nu(s) = \frac{2F_{\text{ext}}}{L_{fil}^2} s \tag{5.5}$$

so that the total force on the filament is

$$F_{\text{tot}} = \int_0^{L_{fil}} \nu(s) ds = F_{\text{ext}} \tag{5.6}$$

We discretize this force density and apply it to the nodes between each element.

The results for $F^{\text{ext}} = 3\,\text{pN}$ are shown in Fig. 5.9. The instantaneous pitches are lower than for point forces, as expected, since the force at the right is effectively acting against the force at the left in addition to the drag. There is also a qualitative difference in the inhomogeneity of the pitch. While in the point-force model, the instantaneous pitch is high in the middle and lower near the edges, the opposite is true for the distributed force model. The pitches are not symmetric, however the asymmetry is slight.

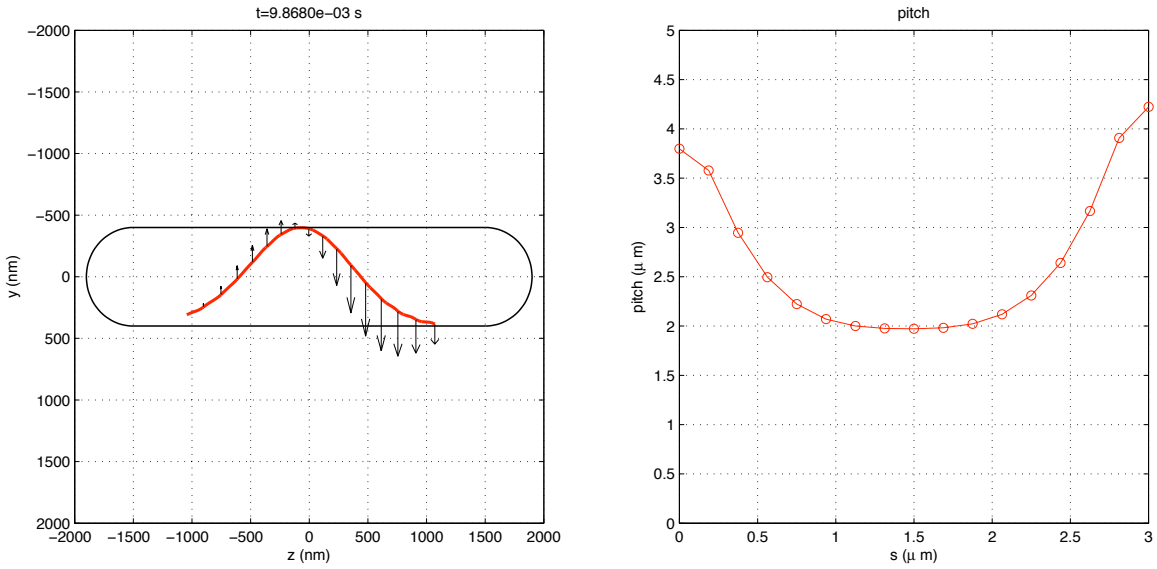

Figure 5.9: Equilibrium configuration (left) and instantaneous pitch (right) of a $3\,\mu$m filament on the membrane of a bacterial cell subject to azimuthal forces totaling $F^{\text{ext}} = 3\,\text{pN}$ distributed along its length according to Eq. 5.5.

As for the previous two models, we repeated the simulation for various F^{ext}. The pitches and angular velocities are shown in Fig. 5.10. As in the dynamic point-force model, the relationship appears linear, with viscosity $\mu = 3.85 \times 10^{-3}\,\text{pN}\,\text{s/rad}$, slightly higher than for the dynamic point-force model.

5.6 Implications and conclusions

The finite element analysis in this chapter offers a preliminary exploration of the elastic dynamics of MreB in vivo. The main conclusion is that forces in physiological range of motor proteins, between $1 - 25\,\text{pN}$, can easily generate pitches in the physiological range, between $0.4 - 2.0\,\mu$m. The simulator will also allow much more complex models to be analyzed.

A coherent explanation for cell wall synthesis in rod-shaped bacteria emerges from the previous two chapters. A putative complex of cell wall synthesis machinery is associated with the MreB helix, and is moving around the circumference of the lateral walls, inserting new peptidoglycan moieties as it goes. This generates an azimuthal

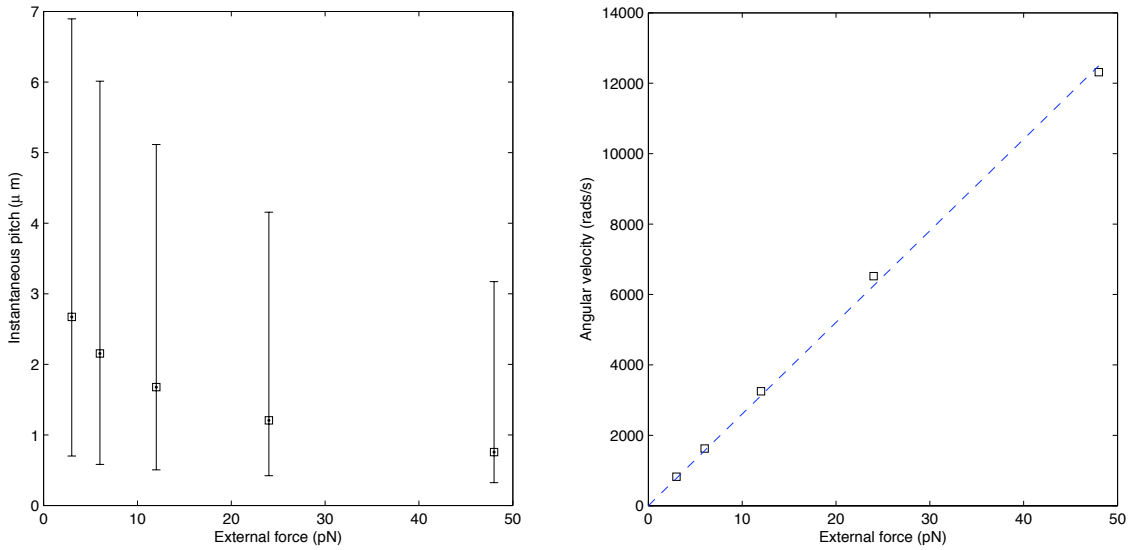

Figure 5.10: (Left) Instantaneous pitch of the steady-state configuration of a $3\,\mu$m filament on the membrane of a bacterial cell subject to distributed azimuthal forces $\vec{F}^{\text{ext}}$. The square indicated the averages, and the vertical bars indicate the minima and maxima. (Right) Angular velocity of in the resulting steady-state. The dotted line shows a linear regression with inverse slope $\mu = 3.85 \times 10^{-3}\,\text{pN}\,\text{s/rad}$.

force back on the helix. Meanwhile, the complex is pushed in the axial direction by MreB. This can occur with bulk advection or any of the possibilities discussed in Sec. 4.6. Thus, there may be a functional interdependence between MreB and the cell wall synthesis machinery. The machinery could require the MreB track to move it axially, necessary for the insertion to happen evenly along the lateral wall [12, 14, 58]. Conversely, MreB requires the machinery to pull it into a helix.

A substantial distinction between the dynamic external force models and the static external force model is the presence of continual rotation in the steady-state, which occurs in the dynamic models since the torque(s) do not balance. Experimentally, Mbl in *B. subtilis* changed curvature and orientation, and it has been suggested that it does indeed rotate inside the cell [9]. However, the speeds at which our models predict they rotate, $10^3 - 10^4$ rad/s, are very high compared with the intervals between fluorescence imaging, which occurs over the course of minutes [9]. This speed is highly dependent on the viscosity, which may be complicated by interaction with the inner

membrane [53]. The viscosity of the membrane itself is $\eta_m \approx 10^{-7}\,\mathrm{pN\,s/\,nm^2}$ [73], which is 100 times larger than the viscosity of the cytoplasm. The viscosity is the only place where time enters our dynamics, and thus if we were to switch η with η_m, all our dynamic times would simply decrease by a factor of 100; the configuration, both in static and dynamic external forces, would be unchanged. Interaction of an extended body in, on, or near a fluid membrane is more subtle [53,54,73]. The no-slip boundary condition requires the fluid membrane to move with the bulk fluid and introduces a length scale $\eta_m d/\eta \approx 500\,\mathrm{nm}$ [54] where $d = 5\,\mathrm{nm}$ is the membrane thickness [5]. Rods longer than this length exhibit more complicated dynamics. Including such effects will require more details about the way in which MreB interacts with the membrane.

A rotating, advecting MreB bundle raises a curious possibility for the relationship between MreB and other helices in bacteria. As discussed in Sec. 2.4, helices such as MreC and SetB appear related to MreB, but do not have the same pitch. If the MreB helix rotates with angular velocity ω, and a second protein decorates it, riding with velocity v, then the space curve traced out by the decorating protein will be another helix with a distinct pitch given by

$$\frac{1}{p_D} = \frac{1}{p} - \frac{\omega R_c}{v}\sqrt{\frac{1}{p^2} + \frac{1}{(2\pi R_c)^2}}. \tag{5.7}$$

For a particular MreB pitch p and angular velocity ω, any decorating pitch, with either handedness, can be achieved by appropriate choice of v. While there are no known biochemical analogies to argue for such a mechanism (J. Theriot, private communication), the connection between distinct helices through rotation remains a formal possibility.

Chapter 6

Conclusions

We have presented a model of MreB based on the polymerization dynamics and elastic properties of a bundle of actin-like polymers. It is self-consistent and addresses the establishment and steady-state of the helix on the elastic timescale of microseconds (Chapter 5) and the polymerization timescale of seconds (Chapter 4).

The model also addresses the many functions of the helix, such as macromolecular transport and cell wall synthesis. Most of the hypotheses are based on speculation articulated qualitatively in reviews [8, 59, 77]. This thesis adds two new major concepts. The first is that polymerization at the tips of the MreB bundle generates a force that varies with helical pitch (via the cytoplasmic concentration), as does the elastic force acting against these tips. This leads to a steady-state in which these forces balance. A result of this thesis is the relationship of this steady-state to system variables, namely the total number of subunits of MreB and the bundle thickness.

The second concept is the idea that molecular motors pulling along the circumference of the lateral cell wall are responsible for winding the MreB bundle into a helix. Our exploration of this hypothesis in Chapter 5 is preliminary, however we have shown that forces in the physiological range can produce pitches in the physiological range.

The conclusions of this thesis also suggest refuting two widespread notions about MreB. The first is that "linear polymers composed of identical subunits, constrained to the inner surface of a cylinder... would always lead to a helical or coiled configuration... unless the initial axis of polymerization was parallel or perpendicular to the long axis of the cylinder" [77]. These linear polymers have a bending stiffness and wish to minimize their elastic energies, thus will often organize into non-helical configurations. With that said, a polymer with an intrinsic curvature (such as FtsZ and tubulin [81]) or whose membrane affinity has an anisotropy (such as MinD [2]) will have different elastic energetics. If MreB turns out to have either of these biochemical properties,

our conclusion will certainly change.

The second notion is the requirement of molecular motors analogous to myosin to move cargo along MreB [8, 77]. We have shown that in steady-state, it is possible to obtain bidirectional transport in the MreB subunits themselves. This provides a myosin-free way to localize cargo to the cell poles, in biological timescales, together with a method for pole discrimination (Sec. 4.6).

6.1 Further work

Several questions have been raised by this work:

- This thesis highlights the need for the polymerization rate constants of MreB in order to make precise quantitative predictions. The mean-field calculation of steady-state suggests only the critical concentration is important, however stochastic simulation demonstrates a need for all four on- and off-rates. How much will they differ from those of actin, and what effect will this have on our results?

- What is the nature of the subunits in the cytoplasm? We have assumed that they are mostly monomers. This appears false for FtsZ [81] and true for actin only in the presence of sequestering agents [34]. If a fraction of the subunits in the cytoplasm are polymeric, they would not participate in the force-generation mechanism, and their isodesmic exchange with the bundle would not affect the steady-state. This would have the effect of reducing the effective total number of subunits N_0, dilating the x-axis of Fig. 4.4.

- In our models of macromolecule translocation, the package being transported was assumed to exert a negligible force on the helix. This is probably true for proteins, but may not be true for larger macromolecules such as the chromosome. What are these response forces, probably acting in the axial direction? What is their effect on the elastic arrangement of the helix, and can it be observed through microscopy? The finite element simulator gives us the opportunity to address this question

- How much can we extrapolate from the conclusions of Chapter 5? Computational cost constrained the simulations mostly to short filaments of $3\,\mu$m, much shorter than their in vivo length. Although the quantitative details will certainly differ for longer filaments, how will their qualities change? Increasing the length to physiological sizes had a small but significant effect on pitch in Fig. 5.6, suggesting our overall conclusions will be preserved.

- What are the differences between the homologues of MreB that are present in Gram-positive species, such as Mbl and MreBH in *B. subtilis*? Some insight is gained into their interactions via the boxed regimes of Fig. 4.4: the pitch and concentration we predict differ whether they bundle together or separately. However, functionally they appear to fulfill different roles that are all performed by the unique MreB in Gram-negative species [10]. What implications does this have for our model?

- Are there prokaryotic analogues to any of the $\sim$ 100 actin-binding proteins that regulate MreB? As actin's interactions with these regulating proteins were mapped out, the quantitative modeling of actin became a rich field [68]. Our present model has shown that polymerization dynamics alone can account for many of MreB's functions. If there are few or no MreB-regulating proteins, further modeling will contribute to understanding how prokaryotes achieve this comparative simplicity. If there are regulating proteins, a wealth of modeling analogous to actin will ensue.

This is one of the first attempts to build a quantitative model of MreB, along with Andrews and Arkin (2007) [2] and Wolgemuth et al. (2005) [91]. Andrews and Arkin (2007) state an alternative model for elasticity based on intrinsic curvature, intrinsic twist and anisotropic membrane affinity, ignoring polymerization dynamics. Wolgemuth et al. (2005) impose the filament's helical configuration and explore its effect on a growing cell envelope. Clearly there is much work to be done, both theoretically and experimentally. For the bacterial cytoskeleton, the interplay between modeling and experiment begins.

Appendix A

Treadmilling in an infinite square well

Suppose a filament is stuck between two rigid barriers (with, eg, Young's modulus $\gg F_{stall}$). When the filament tips reach the edge, new monomers cannot associate with the tips, thus $k^b_{\rm on} = k^p_{\rm on} = 0$. The filament will remain stationary, however individual monomers will advect towards the pointed end. We calculate the rate of advection as follows.

Let T be the (random) time to advect by one monomer. In the following we use the standard notation that $E[X]$ is the expected value of random variable X, and $E[X|A]$ is the expected value of X, given that A is true. There are four possible sequences of events before the filament is returned to its constrained length: $\binom{b}{\rm off}\binom{p}{\rm on}$, $\binom{b}{\rm off}\binom{b}{\rm on}$, $\binom{p}{\rm off}\binom{p}{\rm on}$ or $\binom{p}{\rm off}\binom{b}{\rm on}$. By total expectation,

$$\begin{aligned} E[T] &= E[T|\tbinom{b}{\rm off}\tbinom{p}{\rm on}]P(\tbinom{b}{\rm off}\tbinom{p}{\rm on}) \\ &+ E[T|\tbinom{b}{\rm off}\tbinom{b}{\rm on}]P(\tbinom{b}{\rm off}\tbinom{b}{\rm on}) \\ &+ E[T|\tbinom{p}{\rm off}\tbinom{p}{\rm on}]P(\tbinom{p}{\rm off}\tbinom{p}{\rm on}) \\ &+ E[T|\tbinom{p}{\rm off}\tbinom{b}{\rm on}]P(\tbinom{p}{\rm off}\tbinom{b}{\rm on}) \end{aligned}$$

$$\begin{aligned} E[T](k^b_{\rm off}+k^p_{\rm off})(\lambda^b_{\rm on}+\lambda^p_{\rm on}) &= \left(E[T^b_{\rm off}|T^b_{\rm off}<T^p_{\rm off}]+E[T^p_{+1}|T^p_{+1}<T^b_{+1}]\right)k^b_{\rm off}\lambda^p_{\rm on} \\ &+ \left(E[T]+E[T^b_{\rm off}|T^b_{\rm off}<T^p_{\rm off}]+E[T^b_{+1}|T^b_{+1}<T^p_{+1}]\right)k^b_{\rm off}\lambda^b_{\rm on} \\ &+ \left(E[T]+E[T^p_{\rm off}|T^p_{\rm off}<T^b_{\rm off}]+E[T^p_{+1}|T^p_{+1}<T^b_{+1}]\right)k^p_{\rm off}\lambda^p_{\rm on} \\ &+ \left(2E[T]+E[T^p_{\rm off}|T^p_{\rm off}<T^b_{\rm off}]+E[T^p_{+1}|T^p_{+1}<T^b_{+1}]\right)k^p_{\rm off}\lambda^b_{\rm on} \end{aligned} \tag{A.1}$$

where $\lambda^b_{\rm on} \equiv k^b_{\rm on}c - k^b_{\rm off}$ and equivalently for $\lambda^p_{\rm on}$.

Note that although polymerization events at the two tips are independent, it is not true that the expected time for barbed depolymerization, given that it occurred

before a pointed depolymerization, is the same as the expected time for barbed depolymerization alone. That is,

$$E[T^b_{\text{off}}|T^b_{\text{off}} < T^p_{\text{off}}] \neq E[T^b_{\text{off}}] = 1/k^b_{\text{off}}. \tag{A.2}$$

Instead of solving for $E[T^b_{\text{off}}|T^b_{\text{off}} < T^p_{\text{off}}]$ (which is non-analytic), observe that

$$E[min\{T^b_{\text{off}}, T^p_{\text{off}}\}] = \frac{1}{k^b_{\text{off}} + k^p_{\text{off}}} \tag{A.3}$$

and, again by the law of total expectation,

$$E[min\{T^b_{\text{off}}, T^p_{\text{off}}\}\}] = E[T^b_{\text{off}}|T^b_{\text{off}} < T^p_{\text{off}}]P(^b_{\text{off}}) + E[T^p_{\text{off}}|T^p_{\text{off}} < T^b_{\text{off}}]P(^p_{\text{off}}) \tag{A.4}$$

thus

$$1 = E[T^b_{\text{off}}|T^b_{\text{off}} < T^p_{\text{off}}]k^b_{\text{off}} + E[T^p_{\text{off}}|T^p_{\text{off}} < T^b_{\text{off}}]k^p_{\text{off}}. \tag{A.5}$$

Now rearranging Eq. A.1

$$\begin{aligned} E[T] \quad & ((k^b_{\text{off}} + k^p_{\text{off}})(\lambda^b_{\text{on}} + \lambda^p_{\text{on}}) + k^b_{\text{off}}\lambda^b + k^p_{\text{off}}\lambda^p + 2k^p_{\text{off}}\lambda^b) \\ = \quad & E[T^b_{\text{off}}|T^b_{\text{off}} < T^p_{\text{off}}]k^b_{\text{off}}\lambda^p + E[T^p_{\text{off}}|T^p_{\text{off}} < T^b_{\text{off}}]k^p_{\text{off}}\lambda^b \\ + \quad & E[T^b_{\text{off}}|T^b_{\text{off}} < T^p_{\text{off}}]k^b_{\text{off}}\lambda^b + E[T^p_{\text{off}}|T^p_{\text{off}} < T^b_{\text{off}}]k^p_{\text{off}}\lambda^b \\ + \quad & E[T^b_{+1}|T^p_{+1} < T^b_{+1}]k^b_{\text{off}}\lambda^p + E[T^p_{+1}|T^b_{+1} < T^p_{+1}]k^p_{\text{off}}\lambda^b \end{aligned} \tag{A.6}$$

Making use of Eq. A.5, this simplifies to

$$E[T] = \frac{\lambda^p + \lambda^b + k^b_{\text{off}} + k^p_{\text{off}}}{k^b_{\text{off}}\lambda^p - k^p_{\text{off}}\lambda^n} = \frac{k^p_{\text{on}} + k^b_{\text{on}}}{k^p_{\text{off}}k^b_{\text{on}} - k^b_{\text{off}}k^p_{\text{on}}}.$$

Since this is still exponentially distributed [72], we reciprocate it to obtain the rate of constrained treadmilling,

$$\lambda_{advect} = \frac{k^p_{\text{off}}k^b_{\text{on}} - k^b_{\text{off}}k^p_{\text{on}}}{k^p_{\text{on}} + k^b_{\text{on}}} = \lambda_{tread} \tag{A.7}$$

independent of concentration and identical to the rate of free treadmilling.

Appendix B

Finite element analysis of a biofilament inside a cell

B.1 The finite element method

For an elastic body with Hamiltonian (Eq. 3.14)

$$\mathcal{H} = \frac{1}{2}\int_0^{L_{fil}} \left[\left(B\kappa(s)^2 + C\tau(s)^2\right)\, n(s)^2 + EA(1-|\partial_s \vec{r}|)^2\, n(s)\right] ds \tag{B.1}$$

in a viscous fluid, the time-evolution is given by

$$\partial_t q(s) = -\rho(s)\frac{\delta \mathcal{H}}{\delta q(s)} \tag{B.2}$$

where the $q(s)$ are generalized coordinates, which include the position $\{x(s), y(s), z(s)\}$ and orientation of the rod. For a continuous body, there are an infinite number of coordinates corresponding to the position and (in the case of a Cosserat rod) angles of the body at every point. The $\rho(s)$ are mobilities, which include inverse viscosities and drag coefficients.

The finite element method seeks to solve Eq. B.2 for small perturbations of q_i by the approximation

$$\Delta_t q_i = -\rho_i \sum_j \frac{\partial^2 \mathcal{H}}{\partial q_i \partial q_j} q_j \tag{B.3}$$

which is the first-order Taylor expansion of Eq. B.2, valid for small q_j. Furthermore, instead of continuous $q(s)$, the body's configuration is discretized so that one element is described by a finite number of configuration variables. The Hamiltonian Eq. B.1 requires the coordinates $q(s)$ at every point. To accomplish this, the finite element method first divides the body into a finite number of elements, each of length l^e, so that there are $n_{el} = L_{fil}/l^e$ elements. Then *shape functions* are introduced, $q_{\text{shape}}(s) = q(q_1, q_2, ..., s)$, that describe the configuration between elements. The power of the finite element lies in this fact: space has not been discretized, but rather the set of possible configurations.

Considerable research has gone into finding the best shape functions for particular situations [40,94]. For any smooth shape function, for smaller l^e, Eq. B.3 will converge to Eq. B.2. We use a discretization of twelve *nodes* per element,

$$\{x^e, y^e, z^e, \phi_x^e, \phi_y^e, \phi_z^e, x^f, y^f, z^f, \phi_x^f, \phi_y^f, \phi_z^f\},$$

together with shape functions that have been used for the dynamics of Cosserat rods, based on series solutions of the equilibrium equations [7],

$$\begin{aligned} x_{\text{shape}}(s) &= x^e(s) + \phi_y^e s - \left(3x^e - 3x^f + 2l^e\phi_y^e + l^e\phi_y^f\right)(s/l^e)^2 && \text{(B.4)} \\ &+ \left(2x^e - 2x^f + l^e\phi_y^e + l^e\phi_y^f\right)(s/l^e)^3 && \text{(B.5)} \\ y_{\text{shape}}(s) &= -\phi_x^e s - \left(3y^e - 3y^f - 2l^e\phi_x^e - l^e\phi_x^f\right)(s/l^e)^2 && \text{(B.6)} \\ &+ \left(2y^e - 2y^f - l^e\phi_x^e - l^e\phi_x^f\right)(s/l^e)^3 && \text{(B.7)} \\ z_{\text{shape}}(s) &= z^e + \left(z^f - z^e\right)(s/l^e) && \text{(B.8)} \end{aligned}$$

The vectors $\{\vec{\phi}^e, \vec{\phi}^f\}$ represent the spin vector required to rotate the coordinate axes $\{\hat{x}, \hat{y}, \hat{z}\}$ into $\{\vec{d}_1, \vec{d}_2, \vec{d}_3\}$. We then plug the shape functions into the definitions of the directors $\{\vec{d}_1, \vec{d}_2, \vec{d}_3\}$ and Eq. 3.15 to get the curvature and twist, then into the Hamiltonian, and finally into Eq. B.3. Computer algebra system Maple (Maplesoft) was used for this. The result is, for each element, "stiffness matrix"

$$K_{ij} \equiv -\rho_i \sum_j \frac{\partial^2 \mathcal{H}}{\partial q_i \partial q_j} q_j \tag{B.9}$$

(the language is standard, although not accurate in the viscous case), that is 12×12 elements in size. The time evolution of one element is given by

$$\Delta_t \vec{q}^e = \mathbf{K}^e \vec{q}^e. \tag{B.10}$$

Recall that the filament is one connected structure, and all elements share their nodes with the previous and following element. The time evolution of the entire system is

$$\Delta_t \vec{q} = \sum_{e=1}^{n_{el}} \mathbf{K}^e \vec{q} \tag{B.11}$$

where $\vec{q}$ contains all nodal displacements: there are $d = 6(n_{el} + 1)$ of them. The matrix $\sum \mathbf{K}^e$ is called the global stiffness matrix.

B.2 The stiffness matrix of a Cosserat rod element

The drag coefficients for a right cylinder were solved numerically in the 1970s and 1980s [4, 84, 85]. For a cylinder of length l^e and diameter a, lying on the z-axis, the mobilities are approximately

$$\rho_{xyz} \approx \frac{2}{(6a^2)^{1/3}\eta\, l^e}\left(\frac{\log p_e + 0.312 + 0.565/p_e + 0.1/p_e^2}{6\pi(2p_e/3)^{1/3}}\right) \tag{B.12}$$

$$\rho_{\theta} \approx \frac{8}{6a^2\eta(l^e)^3}\left(\frac{9}{16}\frac{\log p_e - 0.662 + 0.917/p_e - 0.05/p_e^2}{\pi p_e^2}\right) \tag{B.13}$$

$$\rho_{\phi} \approx \frac{8}{6a^2\eta(l^e)^3}\left(8\pi 0.64\left(1 + 0.677/p_e - 0.183/p_e^2\right)\right)^{-1} \tag{B.14}$$

where $p_e = l^e/2a$. Translation mobility is given by ρ_{xyz}, while ρ_θ corresponds to rotation in the x-y plane and ρ_ϕ to rotation in the z-axis. For an element of a filament, whose ends are not exposed to the fluid, these are approximations. For instance, for an element in a much longer filament we would expect only linear terms in the translational mobility, $\rho_{xyz} \propto 1/l^e$. Conversely, giving each element a separate mobility ignores non-local effects mediated by the fluid. This approximation is justified since the local effects are the leading order, separated by the log of the aspect ratio from non-local interactions [74]. A further simplification is made by assuming an equal translational mobility in all directions, when in fact it may differ by a factor of two [54]. Similar mobility coefficients are obtained from the "shish-kebab" model for a rod-like polymer [16].

The stiffness matrix for one element was found using Maple and is shown in Fig. B.1. This matrix has eigenvalues

$$\left[-2\,\frac{\rho_X EA}{l}, -1/2\,\frac{\rho_\Psi\,(B+4\,C)}{l}, -1/2\,\frac{\rho_\Phi B}{l}, \right.$$
$$-3/2\,\frac{B\,(\rho_\Phi l^2 + 4\,\rho_X)}{l^3}, -1/2\,\frac{\rho_\Phi B}{l}, -3/2\,\frac{B\,(\rho_\Phi l^2 + 4\,\rho_X)}{l^3},$$
$$\left. 0, 0, 0, 0, 0, 0\right]. \tag{B.15}$$

The six zero eigenvalues correspond to the six rigid body motions, under which the element can move without changing its energy. The other six give the timestep under which simple Euler updating is stable. For the parameter regime of an actin-like filament, the first eigenvalue dominates with a value of $10^6\,\mathrm{s}^{-1}$.

$$
\begin{bmatrix}
-\frac{3\,\rho_X B}{l^3} & 0 & 0 & 0 & -\frac{3}{2}\frac{\rho_X B}{l^2} & 0 & \frac{3\,\rho_X B}{l^3} & 0 & 0 & 0 & -\frac{3}{2}\frac{\rho_X B}{l^2} & 0 \\
0 & -\frac{3\,\rho_X B}{l^3} & 0 & \frac{3}{2}\frac{\rho_X B}{l^2} & 0 & 0 & 0 & \frac{3\,\rho_X B}{l^3} & 0 & \frac{3}{2}\frac{\rho_X B}{l^2} & 0 & 0 \\
0 & 0 & -\frac{\rho_X EA}{l} & 0 & 0 & 0 & 0 & 0 & \frac{\rho_X EA}{l} & 0 & 0 & 0 \\
0 & \frac{3}{2}\frac{\rho_{\mathbf{\Phi}} B}{l^2} & 0 & -\frac{\rho_{\mathbf{\Phi}} B}{l} & 0 & 0 & 0 & -\frac{3}{2}\frac{\rho_{\mathbf{\Phi}} B}{l^2} & 0 & -\frac{1}{2}\frac{\rho_{\mathbf{\Phi}} B}{l} & 0 & 0 \\
-\frac{3}{2}\frac{\rho_{\mathbf{\Phi}} B}{l^2} & 0 & 0 & 0 & -\frac{\rho_{\mathbf{\Phi}} B}{l} & 0 & \frac{3}{2}\frac{\rho_{\mathbf{\Phi}} B}{l^2} & 0 & 0 & 0 & -\frac{1}{2}\frac{\rho_{\mathbf{\Phi}} B}{l} & 0 \\
0 & 0 & 0 & 0 & 0 & -\rho_{\mathbf{\Psi}}\left(\frac{1}{4}\frac{B}{l}+\frac{C}{l}\right) & 0 & 0 & 0 & 0 & 0 & \rho_{\mathbf{\Psi}}\left(\frac{1}{4}\frac{B}{l}+\frac{C}{l}\right) \\
\frac{3\,\rho_X B}{l^3} & 0 & 0 & 0 & \frac{3}{2}\frac{\rho_X B}{l^2} & 0 & -\frac{3\,\rho_X B}{l^3} & 0 & 0 & 0 & \frac{3}{2}\frac{\rho_X B}{l^2} & 0 \\
0 & \frac{3\,\rho_X B}{l^3} & 0 & -\frac{3}{2}\frac{\rho_X B}{l^2} & 0 & 0 & 0 & -\frac{3\,\rho_X B}{l^3} & 0 & -\frac{3}{2}\frac{\rho_X B}{l^2} & 0 & 0 \\
0 & 0 & \frac{\rho_X EA}{l} & 0 & 0 & 0 & 0 & 0 & -\frac{\rho_X EA}{l} & 0 & 0 & 0 \\
0 & \frac{3}{2}\frac{\rho_{\mathbf{\Phi}} B}{l^2} & 0 & -\frac{1}{2}\frac{\rho_{\mathbf{\Phi}} B}{l} & 0 & 0 & 0 & -\frac{3}{2}\frac{\rho_{\mathbf{\Phi}} B}{l^2} & 0 & -\frac{\rho_{\mathbf{\Phi}} B}{l} & 0 & 0 \\
-\frac{3}{2}\frac{\rho_{\mathbf{\Phi}} B}{l^2} & 0 & 0 & 0 & -\frac{1}{2}\frac{\rho_{\mathbf{\Phi}} B}{l} & 0 & \frac{3}{2}\frac{\rho_{\mathbf{\Phi}} B}{l^2} & 0 & 0 & 0 & -\frac{\rho_{\mathbf{\Phi}} B}{l} & 0 \\
0 & 0 & 0 & 0 & 0 & \rho_{\mathbf{\Psi}}\left(\frac{1}{4}\frac{B}{l}+\frac{C}{l}\right) & 0 & 0 & 0 & 0 & 0 & -\rho_{\mathbf{\Psi}}\left(\frac{1}{4}\frac{B}{l}+\frac{C}{l}\right)
\end{bmatrix}
$$

Figure B.1: The local stiffness matrix, Eq. B.9.

B.3 Large displacements

Using the stiffness matrix as it appears in Fig. B.1, and evolving through time via Eq. B.3 is appropriate for small displacements. However, when individual elements move a large distance away from their equilibrium configuration, or rotate through a large angle, as happens in the helical configurations we with to simulate, Eq. B.3 becomes invalid. To resolve this, we have modified the simple finite element scheme to translate each nodal displacement from *global* coordinates to *local* coordinates, by replacing $\tilde{q}_i = q_i - q_{i-1}$. This has the effect of translating the left endpoint of each element to the origin. As long as each element's right endpoint undergoes only a small displacement, the condition for the validity of Eq. B.3 is restored.

However, large rotations render the stiffness matrix invalid. To correct for this, the entire matrix is split into 16 matrices, each 3×3 matrix $\mathbf{K}_\alpha$ corresponding to a single cartesian coordinate or cartesian rotation. Each of these matrices is rotated by $\vec{\phi}^e$, to the orientation of the left endpoint, before being assembled into a global

stiffness matrix, via the rotation matrix $\mathbf{R}(\vec{\phi}^e) \cdot \mathbf{K}_\alpha \cdot \mathbf{R}(\vec{\phi}^e)^T$. A description of the rotation matrix can be found in [37]. This rotation is computationally taxing: the simulation spends 70% of its time evaluating $\mathbf{R}(\vec{\phi}^e)$.

B.4 Boundary conditions

We now wish to apply external forces to the elastic rod. These come in two types: mechanical forces, where the magnitude and direction of the force are specified, and kinematic constraints, where a constraint is imposed on the rod and the force required to maintain the constraint must be calculated *a posteriori*.

Applying mechanical forces is done simply by adding a term to Eq. B.3,

$$\Delta_t q_i = -\rho_i \sum_j \frac{\partial^2 \mathcal{H}}{\partial q_i \partial q_j} q_j + \rho_i f_i(t) \tag{B.16}$$

where $f_i(t)$ is a force for the q_i representing translational coordinates, or a torque for the q_i representing angular displacements.

Applying kinematic constraints is done as follows. Suppose we wish $\vec{r}_i < \vec{r}_0$ where $\vec{r_0}$ represents, for example, the surface of the cell wall. The correction vector normal to the surface is $\vec{n_i} = \vec{r}_0 - \vec{r}_i$. If the constraint is already satisfied, nothing is done. If it is not, we move $\vec{r'}_i \implies \vec{r}_i + \vec{n_i}$, where the prime indicates the constrained coordinate. We can calculate the constraining force $f_c(t)$ from

$$\Delta_t q_i' = -\rho_i \sum_j \frac{\partial^2 \mathcal{H}}{\partial q_i \partial q_j} q_j + \rho_i f_i(t) + \rho_i f_c(t). \tag{B.17}$$

Combining this with Eq. B.16, we get

$$f_c(t) = \frac{1}{\rho_i \Delta t} \left(q_i' - q_i \right). \tag{B.18}$$

B.5 Preservation of symmetry

The algorithm described so far is asymmetric. The coordinate transformation described in Sec. B.3 forces a choice of a preferred origin and axis. This asymmetry is unstable. In Fig. B.2, we show the result of the simulation for the situation described in Sec. 5.3, where a filament of length $L_{fil} = 3\,\mu$m is pulled azimuthally at

both ends, in opposite directions. The initial configuration and boundary conditions are symmetric, yet the configuration produced by the numerical simulation is highly asymmetric. Taking smaller and smaller elements shrinks the discrepancy, however

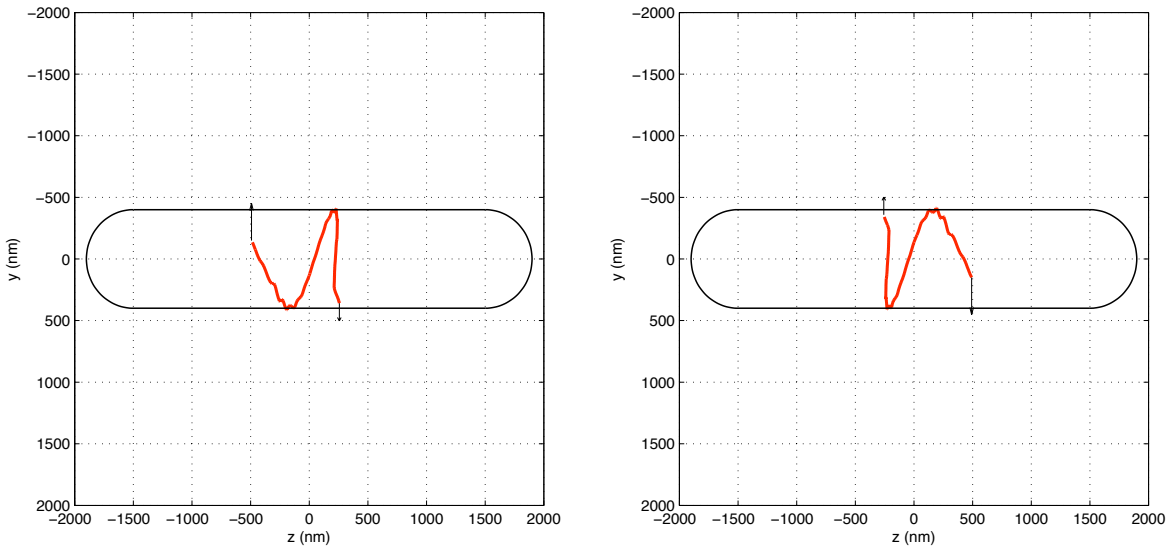

Figure B.2: Configuration of a $3\,\mu$m filament after symmetric azimuthal forces act on its endpoints, as in Fig. 5.5, except with coordinates transformed to the left endpoint of each element (left), and to the right endpoint of each element (right). The configurations are highly asymmetric, indicating a unphysical solution to Eq. B.2.

this has a high computational cost and the asymmetry is still present. To resolve this, at each timestep we localize each element to a set of coordinates centered at the left endpoint, and also to the right endpoint, and take their average. After this, there is no preferred origin and a simulation of a symmetric boundary condition results in a symmetric time evolution (Fig. 5.5).

B.6 Hookean spring test

To test the algorithm, an initially free filament lying in equilibrium on the z axis was exposed to external forces $\vec{F}^{\text{ext}} = \pm 20\,\text{pN}\hat{y}$ at its two ends. The filament responded to the force by rotating (through a transient S-shape) and stretching by $F^{\text{ext}}/EA = 10\%$, as expected. Three snapshots are shown in Fig. B.3. This test confirms the

linear stretching and qualitative bending behavior of the algorithm.

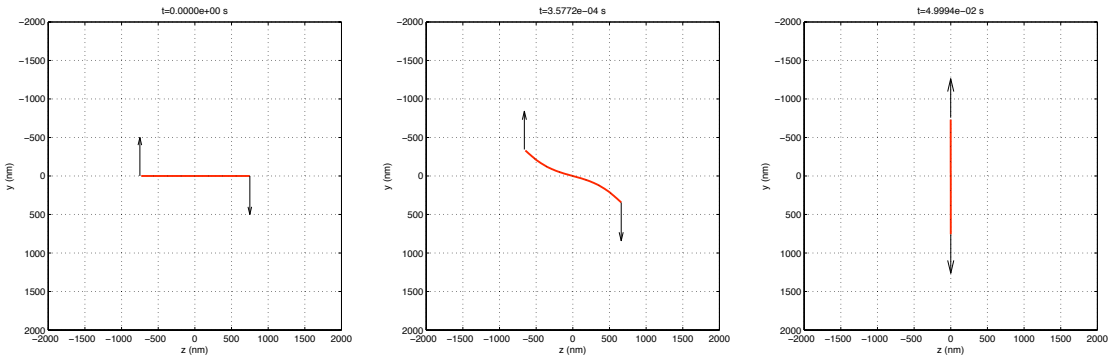

Figure B.3: The time evolution of a 1.5 μm filament initially lying in the z-axis subject to forces in the $\hat{y}$ direction, indicated by the arrows. The unstretched length is $L_{fil} = 1500\,\text{nm}$ and the final filament length is 1515 nm, recovering Hooke's law.

B.7 Euler buckling test

To subject the algorithm to a nonlinear test, we reproduced the Euler buckling phenomenon described in Sec. 3.2.5. For fixed ends, the buckling force, from Eq. 3.51, is

$$F_E = \pi^2 \frac{B}{L_{fil}^2}. \tag{B.19}$$

The Hookean force resulting from squeezing an L_{fil}-long filament in a cell of length L_c is

$$F = EA\left(1 - L_c/L_{fil}\right). \tag{B.20}$$

Equating these and solving for L_{fil}, we get the critical uncompressed filament length

$$L_{fil}^* = \frac{1}{2}\left(L_c + \sqrt{L_c^2 + 4\pi^2 B/EA}\right) \tag{B.21}$$

above which the filament will buckle, and below which the filament should remain straight.

In Fig. B.4 A and B we show the results for $L_{fil} < L_{fil}^*$ and $L_{fil} > L_{fil}^*$, respectively. All runs are given 0.1% uniformly random noise in their initial condition. As expected, the first one remains straight, while the second bows out after buckling.

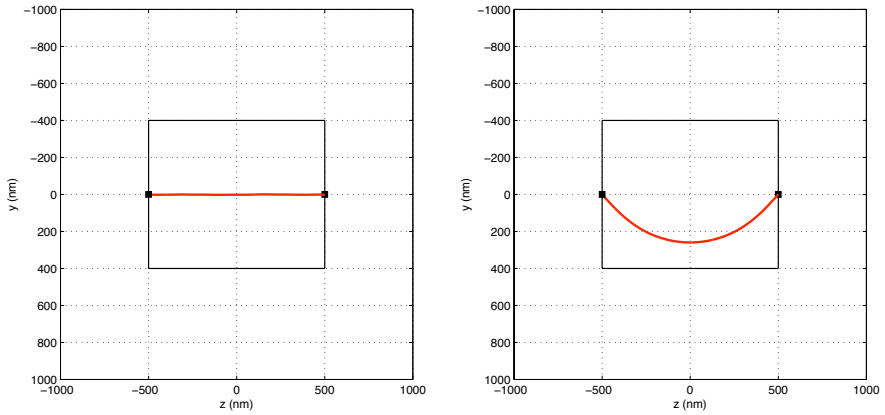

Figure B.4: A filament of length (left) $L_{fil} = 1100\,\text{nm}$ and (right) $L_{fil} = 1300\,\text{nm}$ constrained inside a cell of length $L_c = 1000\,\text{nm}$, with their ends anchored to the poles (indicated by the black squares). To highlight the buckling phenomenon, we decreased the stretching modulus by one order, to $EA = 2\,\text{pN}$. The critical length for Euler buckling is $L^*_{fil} = 1205\,\text{nm}$. In agreement with this, the longer filament buckles into a bowed configuration from the deciduous straight configuration, while the shorter filament remains straight.

Bibliography

[1] B. Alberts et al. *Molecular Biology of the Cell*. Garland Science, 4th edition, 2002. (mre52).

[2] S. S. Andrews and A. P. Arkin. A mechanical explanation for cytoskeletal rings and helices in bacteria. *Biophys. J.* 106.102343, 2007. (mre104).

[3] S. S. Antman. *Nonlinear Problems of Elasticity*. Springer, 2nd edition, 2004. (ela01).

[4] V. A. Bloomfield. Survey of biomolecular hydrodynamics. *http://www.biophysics.org/education/*, 2000. (ela12).

[5] D. Boal. *Mechanics of the Cell*. Cambridge University Press, 2002.

[6] P. Bork, C. Sander, and A. Valencia. An ATPase Domain Common to Prokaryotic Cell Cycle Proteins, Sugar Kinases, Actin, and hsp70 Heat Shock Proteins. *PNAS*, 89(16):7290–7294, 1992.

[7] D. Cao, D. Liu, and C. Wang. Nonlinear dynamic modelling for MEMS components via the Cosserat rod element approach. *Journal of Micromechanics and Microengineering*, 15(6):1334–1343, 2005.

[8] R. Carballido-Lopez. The Bacterial Actin-Like Cytoskeleton. *Microbiol. Mol. Biol. Rev.*, 70(4):888–909, 2006. (mre92).

[9] R. Carballido-Lopez and J. Errington. The Bacterial Cytoskeleton: In Vivo Dynamics of the Actin-like Protein Mbl of *Bacillus subtilis*. *Developmental Cell*, 4:19–28, Jan. 2003. (mre29).

[10] R. Carballido-López, A. Formstone, Y. Li, S. Ehrlich, P. Noirot, and J. Errington. Actin Homolog MreBH Governs Cell Morphogenesis by Localization of the Cell Wall Hydrolase LytE. *Developmental Cell*, 11(3):399–409, 2006. (mre88).

[11] N. Chouaieb, A. Goriely, and J. H. Maddocks. Helices. *PNAS*, 103(25):9398–9403, 2006. (ela14).

[12] R. A. Daniel and J. Errington. Control of Cell Morphogenesis in Bacteria: Two Distinct Ways to Make a Rod-Shaped Cell. *Cell*, 113:767, 2003. (mre30).

[13] P. de Boer, R. Crossley, and L. Rothfield. The essential bacterial cell-division protein FtsZ is a GTPase. *Nature*, 359(6392):254–256, 1992.

[14] M. A. De Pedro, H. Schwarz, and A. L. Koch. Patchiness of murein insertion into the sidewall of Escherichia coli. *Microbiology*, 149(7):1753–1761, 2003. (mre31).

[15] H. J. Defeu Soufo and P. L. Graumann. Dynamic localization and interaction with other bacillus subtilis actin-like proteins are important for the function of mreb. *Molecular Microbiology*, 62(5):1340–1356, 2006. (mre90).

[16] M. Doi and S. Edwards. The Theory of Polymer Dynamics. Oxford University Press 1986.

[17] N. A. Dye, Z. Pincus, J. A. Theriot, L. Shapiro, and Z. Gitai. Two independent spiral structures control cell shape in Caulobacter. *PNAS*, 102(51):18608–18613, 2005. (mre56).

[18] G. Ebersbach and K. Gerdes. Bacterial mitosis: partitioning protein para oscillates in spiral-shaped structures and positions plasmids at mid-cell. *Molecular Microbiology*, 52(2):385–398, 2004. (mre54).

[19] L. Edelstein-Keshet and G. Ermentrout. Models for the length distributions of actin filaments: I. Simple polymerization and fragmentation. *Bulletin of Mathematical Biology*, 60(3):449–475, 1998. (act21).

[20] L. Edelstein-Keshet and G. Ermentrout. Models for spatial polymerization dynamics of rod-like polymers. *Journal of Mathematical Biology*, 40(1):64–96, 2000. (act19).

[21] H. P. Erickson. Cytoskeleton: Evolution in bacteria. *Nature*, 413:30, Sept. 2001. (mre39).

[22] J. Errington. Dynamic proteins and a cytoskeleton in bacteria. *Nature Cell Biology*, 5:175, Mar. 2003. (mre36).

[23] O. Espeli, P. Nurse, C. Levine, C. Lee, and K. J. Marians. SetB: an integral membrane protein that affects chromosome segregation in *Escherichia coli*. *Molecular Microbiology*, 50(2):495–509, 2003. (mre53).

[24] O. Esue, M. Cordero, D. Wirtz, and Y. Tseng. The Assembly of MreB, a Prokaryotic Homolog of Actin. *J. Biol. Chem.*, 280:2628–2635, Jan. 2005. (mre10).

[25] O. Esue, D. Wirtz, and Y. Tseng. GTPase Activity, Structure, and Mechanical Properties of Filaments Assembled from Bacterial Cytoskeleton Protein MreB. *Journal of Bacteriology*, 188(3):968–976, Feb. 2006. (mre38).

[26] E. Evans, D. Berk, and A. Leung. Detachment of agglutinin-bonded red blood cells. I. Forces to rupture molecular-point attachments. *Biophys. J.*, 59(4):838–848, 1991.

[27] R. Feynman. *The Character of Physical Law*. MIT Press, 1967.

[28] A. Fiebig and J. A. Theriot. Bacteria make tracks to the pole. *PNAS*, 101(23):8510–8511, June 2004. (mre33).

[29] R. M. Figge, A. V. Divakaruni, and J. W. Gober. MreB, the cell shape-determining bacterial actin homologue, co-ordinates cell wall morphogenesis in *Caulobacter crescentus*. *Molecular Microbiology*, 51(5):1321–1332, 2004. (mre23).

[30] A. Formstone and J. Errington. A magnesium-dependent mreb null mutant: implications for the role of mreb in *Bacillus subtilis*. *Molecular Microbiology*, 55(6):1646–1657, 2005. (mre67).

[31] E. C. Garner, C. S. Campbell, and R. D. Mullins. Dynamic Instability in a DNA-Segregating Prokaryotic Actin Homolog. *Science*, 306(5698):1021–1025, Nov. 2004. (mre27).

[32] A. S. Ghosh and K. D. Young. Helical Disposition of Proteins and Lipopolysaccharide in the Outer Membrane of *Escherichia coli*. *J Bacteriol.*, 187(6):1913–1922, Mar. 2005. (mre08).

[33] K. A. Gibbs, D. D. Isaac, J. Xu, R. W. Hendrix, T. J. Silhavy, and J. A. Theriot. Complex spatial distribution and dynamics of an abundant Escherichia coli outer membrane protein, LamB. *Molecular Microbiology*, 53(6):1771–1783, 2004. (mre09).

[34] D. Gillespie. Exact stochastic simulation of coupled chemical reactions. *The Journal of Physical Chemistry*, 81(25):2340–2361, 1977.

[35] Z. Gitai, N. Dye, and L. Shapiro. An actin-like gene can determine cell polarity in bacteria. *PNAS*, 101(23):8643–8648, June 2004. (mre34).

[36] Z. Gitai, N. A. Dye, A. Weisenauer, M. Wachi, and L. Shapiro. MreB Actin-Mediated Segregation of a Specific Region of a Bacterial Chromosome. *Cell*, 120:329–341, Feb. 2005. (mre26).

[37] H. Goldstein, C. Poole, J. Safko, and S. Addison. Classical Mechanics. *American Journal of Physics*, 70:782, 2002.

[38] C. Heussinger, M. Bathe, and E. Frey. Statistical mechanics of wormlike bundles, arXiv.org:cond-mat/0702097 2007.

[39] J. Howard. Mechanics of Motor Proteins and the Cytoskeleton: Sinauer Assoc. *Inc., Sunderland, MA*, 367, 2001.

[40] T. Hughes. *The Finite Element Method: Linear static and dynamic finite element analysis*. Dover Publications, 2000.

[41] L. J. F. Jones, R. Carballido-Lopez, and J. Errington. Control of Cell Shape in Bacteria: Helical, Actin-like Filaments in *Bacillus subtilis*. *Cell*, 104:913–922, Mar. 2001. (mre13).

[42] W. Kan, and C. W. Wolgemuth The Shape And Dynamics of *Leptospiraceae*. *Biophysical Journal*, 93(3):54–61, 2007. (mre109).

[43] T. S. Karpova, J. G. McNally, S. L. Moltz, and J. A. Cooper. Assembly and Function of the Actin Cytoskeleton of Yeast: Relationships between Cables and Patches. *J. Cell Biol.*, 142(6):1501–1517, 1998. (act23).

[44] S. Y. Kim, Z. Gitai, A. Kinkhabwala, L. Shapiro, and W. E. Moerner. Single molecules of the bacterial actin MreB undergo directed treadmilling motion in Caulobacter crescentus. *PNAS*, page 0604503103, 2006. (mre71).

[45] G. Kirchhoff. Uber die bewegung eines rotationskorpers in einer Flüssigkeit. *JF Math.(Crelle)*, 71:237, 1869.

[46] D. Kovar and T. Pollard. Progressing actin: Formin as a processive elongation machine. *Nature Cell Biology*, 6(12):1158–1159, 2004.

[47] O. Kratky and G. Porod. Rontgenuntersuchung geloster fadenmolekule. *Rec. Trav. Chim*, 68:1105, 1949.

[48] T. Kruse, B. Blagoev, A. Lobner-Olesen, M. Wachi, K. Sasaki, N. Iwai, M. Mann, and K. Gerdes. Actin homolog MreB and RNA polymerase interact and are both required for chromosome segregation in *Escherichia coli*. *Genes Dev.*, 20(1):113–124, 2006. (mre50).

[49] T. Kruse, J. Bork-Jensen, and K. Gerdes. The morphogenetic MreBCD proteins of *Escherichia coli* form an essential membrane-bound complex. *Molecular Microbiology*, 1(55):78–89, 2005. (mre07).

[50] T. Kruse, J. Moeller-Jensen, A. Loebner-Olesen, and K. Gerdes. Dysfunctional MreB inhibits chromosome segregation in *Escherichia coli*. *The EMBO Journal*, 22(19):5283–5292, 2003. (mre73).

[51] P. Kundu and I. Cohen. *Fluid mechanics*. Academic Press San Diego, 1990.

[52] L. D. Landau and E. M. Lifshitz. *Theory of Elasticity*. J.W. Arrowsmith Ltd., 2nd edition, 1970. (ela04).

[53] A. Levine, T. Liverpool, and F. MacKintosh. Dynamics of Rigid and Flexible Extended Bodies in Viscous Films and Membranes. *Physical Review Letters*, 93(3):38102, 2004. (ela15).

[54] A. Levine, T. Liverpool, and F. MacKintosh. Mobility of extended bodies in viscous films and membranes. *Physical Review E*, 69(2):21503, 2004.

[55] J. Levine, H. Y. Kueh, and L. Mirny. Intrinsic Fluctuations, Robustness, and Tunability in Signaling Cycles. *Biophys. J.*, 92(12):4473–4481, 2007.

[56] A. Love. *Treatise on the Mathematical Theory of Elasticity*. Dover Pubns, 1944.

[57] A. Marée, A. Jilkine, A. Dawes, V. Grieneisen, and L. Edelstein-Keshet. Polarization and Movement of Keratocytes: A Multiscale Modelling Approach. *Bulletin of Mathematical Biology*, 68(5):1169–1211, 2006.

[58] N. H. Mendelson. Helical growth of *Bacillus subtilis*: A new model of cell growth. *Proc Natl Acad Sci USA*, 73(5):1740–1744, May 1976. (mre44).

[59] K. A. Michie and J. Lowe. Dynamic filaments of the bacterial cytoskeleton. *Annual Review of Biochemistry*, 75(1):467–492, 2006. (mre86).

[60] A. Mogilner and L. Edelstein-Keshet. Regulation of Actin Dynamics in Rapidly Moving Cells: A Quantitative Analysis. *Biophysical Journal*, 83(3):1237–1258, 2002. (act20).

[61] A. Mogilner and G. Oster. Cell motility driven by actin polymerization. *Biophys. J.*, 71(6):3030–3045, 1996. (act01).

[62] A. Mogilner and G. Oster. Force generation by actin polymerization II: The elastic ratchet and tethered filaments. *Biophys. J.*, 84:1591–1605, 2003. (act03).

[63] A. Mogilner and G. Oster. Polymer motors: Pushing out the front and pulling up the back. *Current Biology*, 13:721–733, Sept. 2003. (act04).

[64] M. Morimatsu, A. Nakamura, H. Sumiyoshi, N. Sakaba, H. Taniguchi, K. Kohama, and S. Higashi-Fujime. The molecular structure of the fastest myosin from green algae, Chara. *Biochem Biophys Res Commun*, 270(1):147–52, 2000. (act24).

[65] C. Peskin, G. Odell, and G. Oster. Cellular motions and thermal fluctuations: the Brownian ratchet. *Biophysical Journal*, 65(1):316–324, 1993.

[66] T. Pollard. Rate constants for the reactions of ATP- and ADP-actin with the ends of actin filaments. *J. Cell Biol.*, 103(6):2747–2754, 1986.

[67] T. D. Pollard. The cytoskeleton, cellular motility and the reductionist agenda. *Nature*, 422:741–745, Apr. 2003. (mre18).

[68] T. D. Pollard and G. G. Borisy. Cellular motility driven by assembly and disassembly of actin filaments. *Cell*, 112:453–465, Feb. 2003. (act05).

[69] J. M. Raser and E. K. O'Shea. Control of Stochasticity in Eukaryotic Gene Expression. *Science*, 304(5678):1811–1814, 2004.

[70] C. Revenu, R. Athman, S. Robine, and D. Louvard. The co-workers of actin filaments: from cell structures to signals. *Nature Reviews Molecular Cell Biology*, 5(8):635–646, 2004.

[71] M. Rief, R. S. Rock, A. D. Mehta, M. S. Mooseker, R. E. Cheney, and J. A. Spudich. Myosin-V stepping kinetics: A molecular model for processivity. *PNAS*, 97:9482–9486, Aug. 2000. (act25).

[72] S. Ross. *Introduction to Probability Models*. Academic Press, 2006.

[73] P. G. Saffman and M. Delbruck. Brownian Motion in Biological Membranes. *PNAS*, 72(8):3111–3113, 1975.

[74] M. J. Shelley and T. Ueda. The stokesian hydrodynamics of flexing, stretching filaments. *Physica D Nonlinear Phenomena*, 146:221–245, Nov. 2000. (ela03).

[75] Y.-L. Shih, I. Kawagishi, and L. Rothfield. The MreB and Min cytoskeletal-like systems play independent roles in prokaryotic polar differentiation. *Molecular Microbiology*, 58(4):917–928, 2005. (mre37).

[76] Y.-L. Shih, T. Le, and L. Rothfield. Division site selection in *Escherichia coli* involves dynamic redistribution of Min proteins within coiled structures that extend between the two cell poles. *Proc Natl Acad Sci USA*, 100(13):7865–7870, June 2003. (mre45).

[77] Y.-L. Shih and L. Rothfield. The Bacterial Cytoskeleton. *Microbiol. Mol. Biol. Rev.*, 70(3):729–754, 2006. (mre87).

[78] D. Shiomi, S. Banno, M. Homma, and I. Kawagishi. Stabilization of Polar Localization of a Chemoreceptor via Its Covalent Modifications and Its Communication with a Different Chemoreceptor. *J. Bacteriol.*, 187(22):7647–7654, 2005. (mre51).

[79] S. Smith. Neuronal cytomechanics: The actin-based motility of growth cones. *Science*, 242(4879):708, 1988.

[80] H. J. D. Soufo and P. L. Graumann. Dynamic movement of actin-like proteins within bacterial cells. *EMBO reports*, 5(8):789–794, 2004. (mre25).

[81] J. Stricker, P. Maddox, E. D. Salmon, and H. P. Erickson. Rapid assembly dynamics of the *Escherichia coli* FtsZ-ring demonstrated by fluorescence recovery after photobleaching. *PNAS*, 99(5):3171–3175, 2002. (mre89).

[82] S. Thanedar and W. Margolin. FtsZ Exhibits Rapid Movement and Oscillation Waves in Helix-like Patterns in *Escherichia coli* . *Current Biology*, 14:1167–1173, July 2004. (mre04).

[83] J. Theriot. The Polymerization Motor. *Traffic*, 1:19–28, 2000. (act12).

[84] M. M. Tirado and J. G. de la Torre. Translational friction coefficients of rigid, symmetric top macromolecules. application to circular cylinders. *The Journal of Chemical Physics*, 71(6):2581–2587, 1979.

[85] M. M. Tirado and J. G. de la Torre. Rotational dynamics of rigid, symmetric top macromolecules. application to circular cylinders. *The Journal of Chemical Physics*, 73(4):1986–1993, 1980.

[86] F. van den Ent, L. Amos, and J. Lőwe. Bacterial ancestry of actin and tubulin. *Current Opinion in Microbiology*, 4:634, 2001. (mre14).

[87] J. van der Gucht, E. Paluch, J. Plastino, and C. Sykes. Stress release drives symmetry breaking for actin-based movement. *PNAS*, 102(22):7847–7852, 2005.

[88] G. van der Heijden and J. Thompson. Helical and Localised Buckling in Twisted Rods: A Unified Analysis of the Symmetric Case. *Nonlinear Dynamics*, 21(1):71–99, 2000. (ela13).

[89] C. D. Webb, P. L. Graumann, J. A. Kahana, A. A. Teleman, P. A. Silver, and R. Losick. Use of time-lapse microscopy to visualize rapid movement of the replication origin region of the chromosome during the cell cycle in *Bacillus subtilis*. *Molecular Microbiology*, 28(5):883–892, 1998. (mre91).

[90] A. Wells, A. Lin, L. Chen, D. Safer, S. Cain, T. Hasson, B. Carragher, R. Milligan, and H. Sweeney. Myosin VI is an actin-based motor that moves backwards. *Nature*, 401(6752):505–508, 1999.

[91] C. W. Wolgemuth, Y. F. Inclan, J. Quan, S. Mukherjee, G. Oster, and M. A. R. Koehl. How to make a spiral bacterium. *Physical Biology*, 2:189–199, Sept. 2005. (mre65).

[92] S. Yamamoto and T. Matsuoka. A method for dynamic simulation of rigid and flexible fibers in a flow field. *J. Phys. Chem.*, 98:644–650, Jan. 1993. (ela02).

[93] X. Yao, M. Jericho, D. Pink, and T. Beveridge. Thickness and Elasticity of Gram-Negative Murein Sacculi Measured by Atomic Force Microscopy. *J. Bacteriol.*, 181(22):6865–6875, 1999. (mre49).

[94] O. Zienkiewicz and R. Taylor. *The Finite Element Method*. Butterworth-Heinemann, 2000.